



**THE  
DROP**



**DISASTER RESPONSE  
SEARCH AND  
IDENTIFICATION ATTRITABLE  
AIR VEHICLE**



**LIÈGE université  
Sciences Appliquées**





# THE DROP



MTOW = 6,934 lbs



Speed = Mach 0.7



Altitude = 30,000 ft



Price = 1,633,078 \$



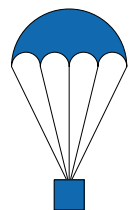
Take-off distance =  
3,037 ft



Landing distance =  
1,733 ft












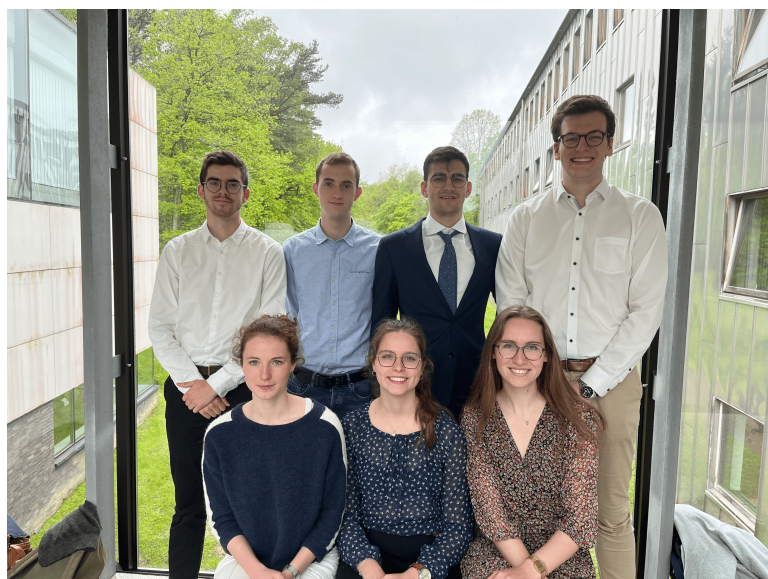
Range = 5,219 nm



Number of survival  
packages : 63

## TEAM MEMBERS

Name	AIAA N°	Mail	Signature
Eric Pavel AZANGUE DONGMO	1402878	paveleric.azangedongmo@student.uliege.be	
Mathias BRACH	1404176	mathias.brach@student.uliege.be	
Léonore COLSON	1404136	leonore.colson@student.uliege.be	
Charles JACQUET	1405468	charles.jacquet@student.uliege.be	
Benoît LAURENT	1402675	b.laurent@student.uliege.be	
Lucie LINOTTE	1403480	lucie.linotte@student.uliege.be	
Florian MULLER	1402876	florian.muller@student.uliege.be	
Colette REMACLE	1402807	colette.remacle@student.uliege.be	
Cédric SERET	1402877	cedric.seret@student.uliege.be	



Team members of The Drop.

## FACULTY ADVISORS

Professors	Assistants
	Arnaud BUDO
Grigorios DIMITRIADIS	Adrien CROVATO
Ludovic NOELS	Paul DECHAMPS
	Thomas LAMBERT

# Contents

<b>1</b>	<b>Introduction</b>	<b>1</b>	7.2 Drag analysis . . . . .	42
<b>2</b>	<b>Mission analysis and requirements</b>	<b>2</b>	<b>8 Structure</b>	<b>49</b>
<b>3</b>	<b>Methodology</b>	<b>4</b>	8.1 Materials selection . . . . .	49
<b>4</b>	<b>General design choices</b>	<b>4</b>	8.2 Characteristic diagrams . . . . .	51
4.1	Statistical study . . . . .	4	8.3 Loads computation . . . . .	54
4.2	General characteristics . . . . .	5	8.4 Structural design . . . . .	57
4.3	CAD model . . . . .	6	<b>9 Aircraft performances</b>	<b>70</b>
<b>5</b>	<b>Components design</b>	<b>8</b>	9.1 Take-off . . . . .	70
5.1	Lifting surfaces . . . . .	8	9.2 Climb . . . . .	72
5.2	Fuselage . . . . .	18	9.3 Turn . . . . .	74
5.3	Propulsion System . . . . .	20	9.4 Glide . . . . .	76
5.4	Landing gear . . . . .	23	9.5 Landing . . . . .	76
5.5	Avionics, subsystems and sensors . . . . .	27	9.6 Payload-range diagram . . . . .	79
5.6	Payload release . . . . .	27	<b>10 Cost Analysis</b>	<b>80</b>
5.7	Weights and centers of gravity . . . . .	30	10.1 Economy projection in 2028 . . . . .	81
<b>6</b>	<b>Stability</b>	<b>32</b>	10.2 Number of hours . . . . .	81
6.1	Static stability . . . . .	32	10.3 Cost Evaluation . . . . .	82
6.2	Dynamic stability . . . . .	36	10.4 Break-even analysis . . . . .	85
<b>7</b>	<b>Aerodynamics</b>	<b>39</b>	10.5 Operational costs . . . . .	86
7.1	Lift analysis . . . . .	39	<b>11 Trade-off study</b>	<b>88</b>
			<b>12 Conclusion</b>	<b>90</b>
			<b>A Derivatives</b>	<b>91</b>

# 1 Introduction

Due to global warming, it has been predicted that weather disasters, such as hurricanes, typhoons, and cyclones, will be more intense in the next years [1]. Their frequency might increase as well. However, the frequency of earthquakes should remain the same over time [2, 3]. Moreover, because of the demographic growth, a larger part of the population will be exposed to these increasing phenomena. Thus, one of the main challenges in the next decade is to be able to quickly provide assistance to these victims. During these episodes, the means of communication are frequently cut off. Consequently, the victims remain unable to contact the emergency services. In addition, the water distribution network is often cut. In that case, humans can only survive three days. Therefore, locating the victims and providing them with a communication device and water is the main objective during rescue missions. This should be achieved as fast as possible since hours or minutes spared can save numerous lives.

With this in mind, the American Institute of Aeronautics and Astronautics (AIAA) proposed to design an air device capable of covering a large land area, identify victims and provide them rescue resources. Its initial entry into service is expected to be in 2028. The Drop was designed to complete that mission. It is a victim assistance aircraft with two main missions: identify the victims and drop satellite phones and drinkable water during natural disasters. The Drop's name has been chosen to match its mission: drop first aid kits containing water, which can also be associated to drops. The potential users for a search and identification drone used in natural disaster situations would likely be any organization or individual involved in disaster relief and rescue efforts. These groups would benefit from its ability to quickly and efficiently search for survivors in the aftermath of a natural disaster.

First, the numerous issues that must be addressed during the design process are described. In parallel, the main characteristics of The Drop are listed and compared to the AIAA requirements. This aims to ensure that its mission is fulfilled.

Afterwards, the general design followed by a detailed analysis are presented. The wing, the tail, the fuselage, the engine, the landing gears, the avionics and the payload release are designed in order to meet the AIAA requirements. The precise dimensions of each component are described. Then, an accurate weight breakdown is made. The stability is then studied both statically and dynamically. A lift and drag analysis is presented for the wing as well. In addition, a full drag analysis of the aircraft is presented.

Subsequently, the structure is studied. The material selection of the components is first stated. The characteristic diagrams are then plotted. By computing the loads applied to The Drop in the worst cases, the structure of the fuselage and of the wing is highlighted. This section thus aims to verify that the aircraft resists to the loads applied during flight. Additionally, the aircraft performances at take-off and landing are examined. Through these sections, it is shown that the AIAA requirements are met.

The cost is then studied. Both the production and the operational costs are estimated. Eventually, a trade-off study is carried out. This section aims to prove that the design is the most optimal to complete the mission.

## 2 Mission analysis and requirements

In Table 2.1, The Drop's characteristics are listed. If the objectives provided by AIAA [4] are met, the value is in bold. Otherwise, only the threshold is reached.

The Drop must display the following features: a maximal loiter, a long ferry range, an ability to operate in rough weather, a small overall size, minimal operational logistics, a simple design, low acquisition costs, enhanced performances and a beneficial trade-off of cost and attritability.

These characteristics allow an easy and adjustable logistic. By maximizing the loiter, the time during which the packages are delivered is maximized. More victims can thus be helped. It corresponds to the second mission formulated by AIAA [4]. The third mission is to display a long ferry range. This allows to deploy the aircraft from anywhere within hours. Then, in order to start searching as fast as possible, the aircraft must be compatible with rough weather such as downdrafts which may persist right after the disaster. Additionally, a small and simple design facilitates the maintenance and limits the possible damages. Finally, decreasing the costs is always a major objective and even more for this mission since there is a high risk of loss.

The flight mission is represented in Figure 2.1. It resumes the main characteristics of The Drop's flight. The rescue kits are delivered during loiter. The ingress and the egress correspond respectively to the distance that has to be covered to flight to and to flight back from the impacted area.

Table 2.1: The Drop’s characteristics compared to the AIAA requirements.

Requirements	The Drop
Minimum cruise ingress range at 30,000 ft	<b>850 nm</b>
Minimum cruise ingress Mach at 30,000 ft	0.7
Minimum loiter time at 30,000 ft & Mach 0.7	<b>5 hrs</b>
Minimum cruise egress range at 30,000ft	<b>2,000 nm</b>
Minimum cruise egress Mach at 30,000ft	0.7
Maximum landing concrete runway length	1,936 ft
Minimum dash speed capability at 30,000 ft	0.8 Mach
Minimum loiter time at recovery/landing site	<b>45 min</b>
Minimum mission payload weight	<b>330 lbs</b>
Minimum free flight loads	4.5 g’s
Minimum number of sorties life with only search and ID ops	<b>50</b>
Maximum take-off concrete runway length	3,078 ft
Upward flight limit loads	<b>3 g’s</b>
Downward flight limit loads	<b>-1.5 g’s</b>
Factor of safety	<b>1.5</b>

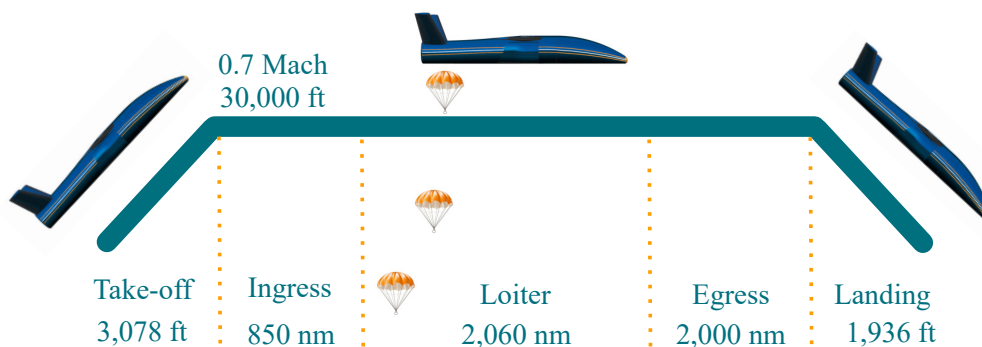


Figure 2.1: Flight mission diagram.

### 3 Methodology

After approximating the maximum take-off and zero-fuel weight, an iterative process is conducted in order to determine The Drop’s design. The methodology is represented in Figure 3.1. First, a conceptual design of the aircraft is attempted. If the static stability is verified and if the weight converges, then the preliminary design is started. If the requirements are not fulfilled, then the design is adapted. Otherwise, a final design is obtained.

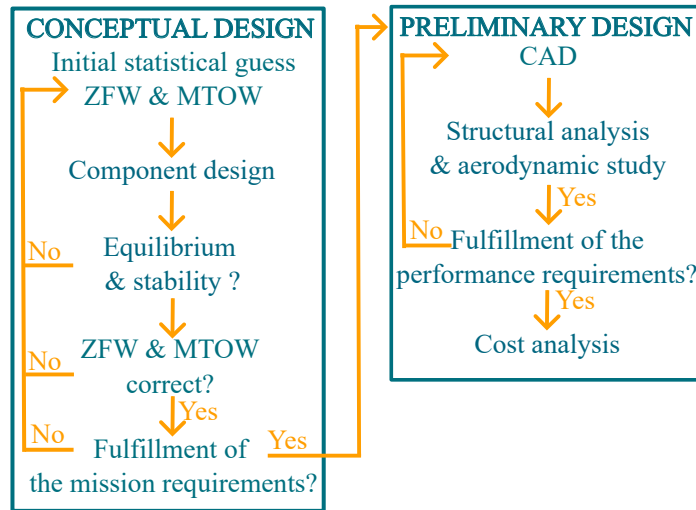


Figure 3.1: Design methodology.

## 4 General design choices

### 4.1 Statistical study

First of all, in order to make a first approximation of the maximum take-off weight and determine the main features of The Drop, a statistical study is conducted. Four aircraft with a similar required range, service ceiling or design Mach were selected. These are the Northrop Grumman X-47B, EADS Barracuda, Baykar Bayraktar Kızılelma and Scaled Composites 401 shown in Figure 4.1. Their main characteristics are summarized in Table 4.1.





(a) Northrop Grumman X-47B [5].



(b) EADS Barracuda [6].



(c) Baykar Bayraktar Kızılelma [7].



(d) Scaled Composites 401 [8].

Figure 4.1: Review of existing designs.

Table 4.1: Features of Northrop Grumman X-47B, EADS Barracuda, Baykar Bayraktar Kızılelma and Scaled Composites 401.

Aircraft	Range [nm]	Service ceiling [ft]	Design Mach	MTOW [lbs]
Northrop Grumman X-47B	2,100	42,000	0.9	44,567
EADS Barracuda	110	20,000	0.85	7,165
Baykar Bayraktar Kızılelma	500	45,000	0.6	13,228
Scaled Composites 401	1,082	30,000	0.6	8,000

## 4.2 General characteristics

It can be observed in Table 4.1 that the range of these aircraft is lower than requested while the service ceiling and the design Mach vary around the wanted cruise characteristics. The design must then be adjusted in order to meet the mission requirements. The general features of The Drop are based on these selected aircraft. The reasons behind each characteristic are presented in detail in their respective parts.

First of all, The Drop has a V-tail to reduce the interference drag generated by the aft part of the aircraft. This tail is however more complex to control. Then, the choice of a single engine is made to reduce the costs of the aircraft, as well as the generated drag. This choice was only possible because The Drop is autonomous. The restrictions are indeed more lax. For seek of stability, a high wing is considered. Since the aircraft flies at transonic speed, a supercritical airfoil is selected. Still in order to ensure stability, a tricycle landing gear is chosen. Moreover, the choice of an elliptical fuselage is made for structural and aerodynamics considerations. The body is also maximally streamlined in order to minimize the drag in cruise. In addition, The Drop is a lifting body. The ability of the fuselage to generate some lift is nevertheless not taken into account in the computations at this stage of the design. However, the eventual benefits and drawbacks of this configuration are

later considered in the trade-off study. The engine is placed inside the fuselage and the air intakes start below the wing to reduce the drag and interferences. Additionally, this configuration does not decrease the efficiency of the tail since the flow coming out of the engine does not interfere with the tail of the plane. Finally, regarding the payload release system, a bay door release system is preferred to a back door one. This configuration indeed displays the advantage to enable a release at high altitude. The dropped survival packages contain water packs, a satellite phone and a survival kit.

After selecting the main characteristics of The Drop, a first estimate of the maximum take-off weight is computed. Seeking for a trade-off between the requirements and the characteristics of the selected aircraft, a maximum take-off weight of **9,200 lbs** is calculated. This first estimate is used in the first design steps of The Drop.

### 4.3 CAD model

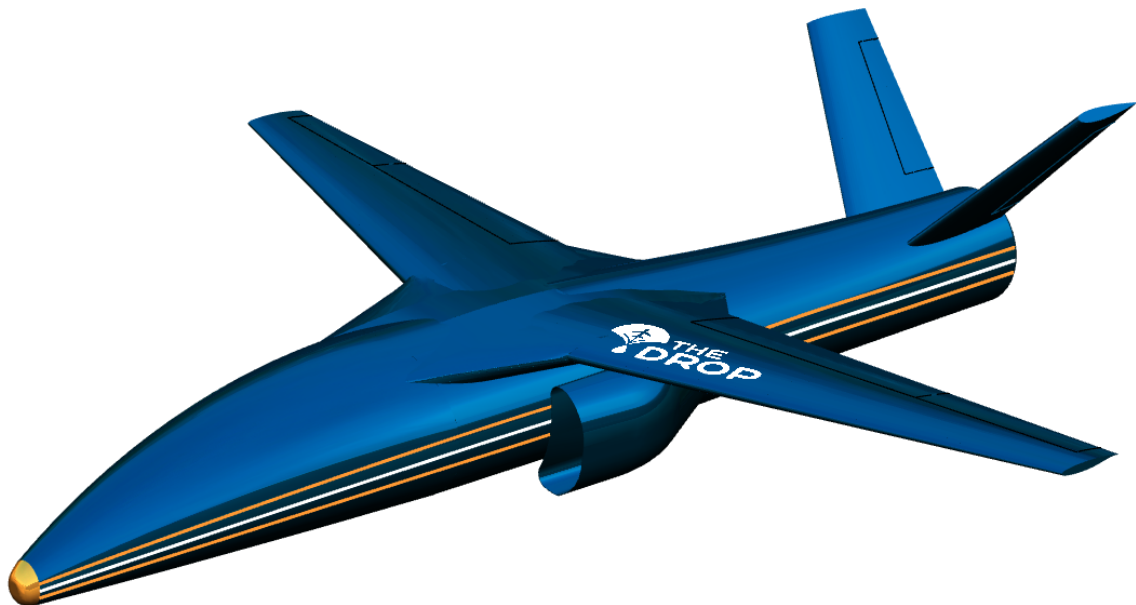


Figure 4.2: The Drop, CAD model.

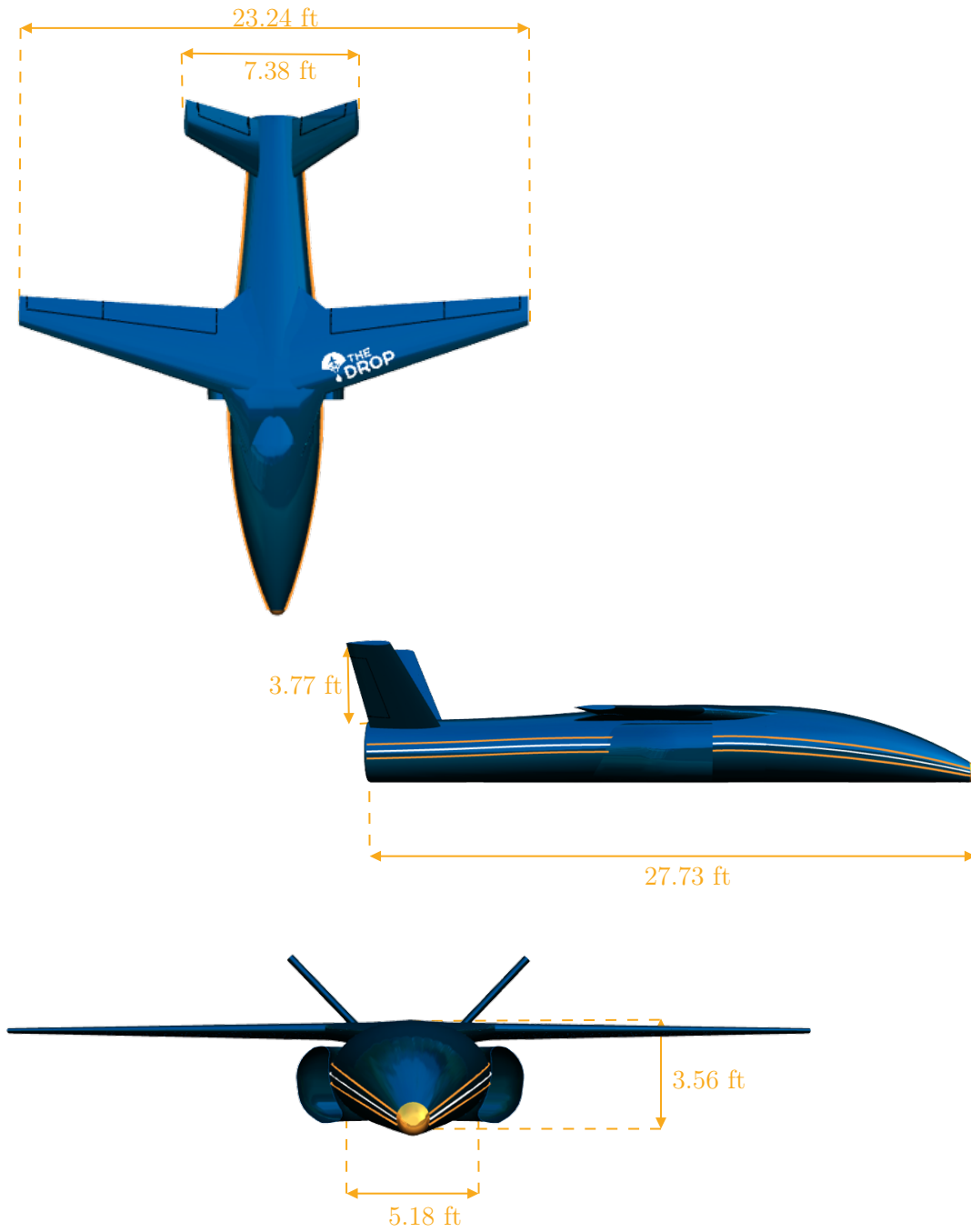


Figure 4.3: Main dimensions of The Drop: top, side and front views.

## 5 Components design

### 5.1 Lifting surfaces

#### 5.1.1 Wing

##### Wing planform

The wing planform is shown in Figure 5.1. Its geometry is determined by applying Raymer's methodology [9]. The flaps and ailerons are represented as well in the figure. Their design is presented at the end of this section.

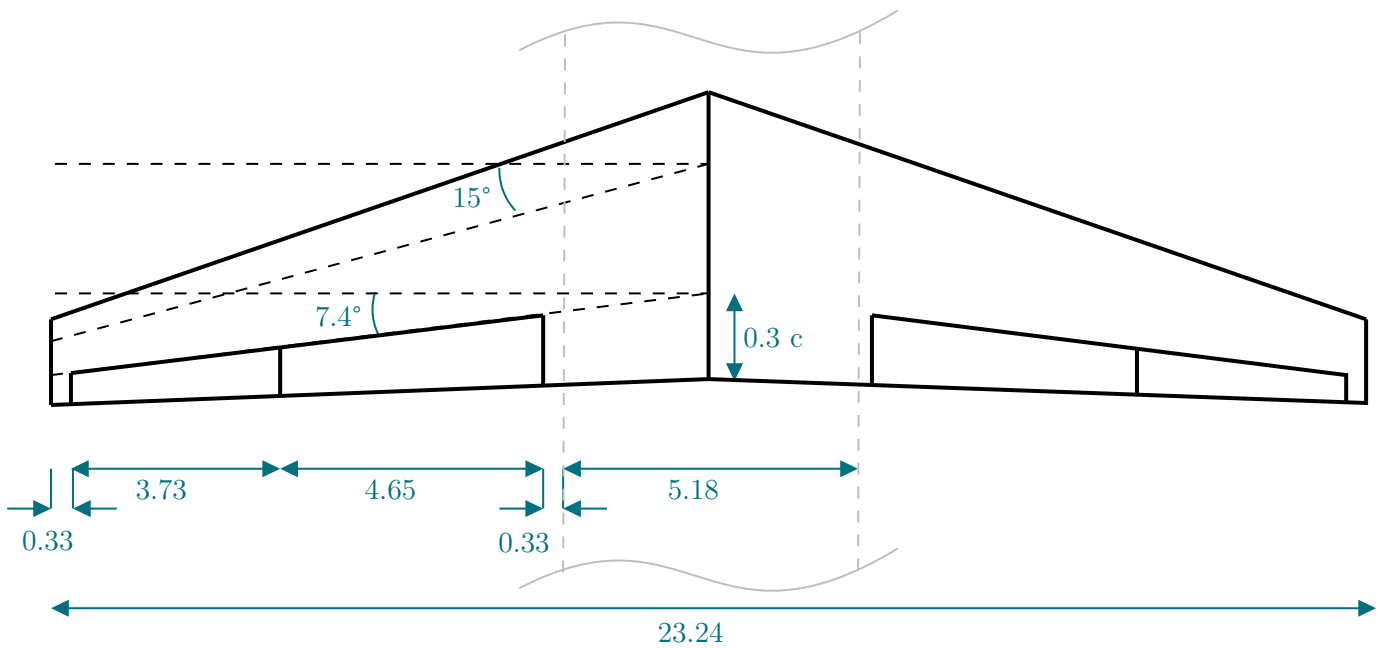


Figure 5.1: Wing planform, dimensions in feet.

The wing surface  $S_W$  is estimated considering a first guess of the lift coefficient at cruise. It ranges between 0.3 and 0.5 according to Raymer [9]. Since a higher lift coefficient results in higher structural loads,  $C_{LW} = 0.35$  is selected. This value is indeed close to 0.3 and enables to produce enough lift. By iterating over the tail and the wing, it is found that the wing surface  $S_W$  is equal to 77.14 ft<sup>2</sup>.

The aspect ratio  $AR_W$  is chosen considering a trade-off between the structural design and the aerodynamic performances. A high aspect ratio reduces the induced drag but increases the structural loads on the wing.

For light aircraft,  $AR_W$  is between 7 and 9 [9]. Since more importance is given to the reduction of the loads, the aspect ratio of The Drop is set to 7.

The **span**  $b$  is easily derived knowing the aspect ratio and the wing surface. It is equal to 23.24 ft.

The **tapper ratio**  $\lambda_W$  is set to 0.3 in order to reduce induced drag. Additionally, the lift distribution is then close to an elliptical one, which is the best possible configuration [9]. Moreover, introducing taper allows to reduce lift and thus the structural loads at the wing tip as well. Then, taking into account that the half wing is trapezoidal, the chord at the root,  $c_{\text{root}} = 5.11$  ft, and the chord at the tip,  $c_{\text{tip}} = 1.53$  ft, are computed.

The (**aerodynamic**) **twist angle**  $\varepsilon_a$  is used, still with the aim of reducing loads at the wing tip and to fit the lift distribution to the elliptical one. Moreover, a negative twist allows to avoid that the wing tip stalls before the wing root. A reasonable value of twist is  $-1^\circ$  [10].

### 5.1.2 Airfoil selection

Because of its high efficiency in transonic regime, a supercritical airfoil profile is chosen for The Drop's wing. Supercritical airfoils indeed present numerous advantages [11]. First of all, they are designed to delay the onset of wave drag, which is a form of drag that becomes significant at transonic speeds. By delaying the onset of wave drag, supercritical airfoils can improve the aircraft's efficiency, reduce drag and thus the needed thrust. Additionally, it is capable of supporting higher speeds than conventional airfoils (like NACA series), which can be beneficial in disaster response operations where speed is critical. Finally, the change in curvature is more gradual over the upper part of the airfoil. This feature can provide a more stable and predictable airflow over the wing, contributing to an improved stability and handling characteristics [11]. However, since this type of airfoils is less commonly used than NACA series, the manufacturing and maintenance costs can be higher. According to statistics [9], the thickness-to-chord ratio is about 12% for high subsonic jet. Moreover, the design lift coefficient has to be close to the lift coefficient of the wing, which is equal to 0.34. The chosen airfoil profile is then the NASA SC(2)-0412. Its design lift coefficient indeed corresponds to the desired characteristics [12]. The airfoil profile is represented in Figure 5.2 and its main features are listed in Table 5.1.

Table 5.1: Characteristics of the NASA SC(2)-0412.

Property	Symbol	Value
Design lift coefficient	$c_{l_{\text{design}}}$	0.4
Maximum thickness-to-chord ratio	$\frac{t}{c}$	12 %
Divergence Mach number	$M_D$	0.786
Lift coefficient derivative	$c_{l_\alpha}$	$9.55 \text{ rad}^{-1}$
Zero lift angle	$\alpha_{l_0}$	$-1.5^\circ$



Figure 5.2: Profile of the NASA SC(2)-0412.

The values for  $c_{l_\alpha}$  and  $\alpha_{l_0}$  are obtained at Mach 0.7 with the software XFOIL which gives reliable data in transonic regime according to its documentation [13].

### Other geometrical parameters

A [sweep angle](#)  $\Lambda_{1/4w}$  is not necessary since the divergence Mach is higher than the cruise Mach number  $M_{\text{cruise}} = 0.7$ . However, in order to reach the dash speed  $M_c = 0.8$ , a sweep angle is nonetheless introduced. It is computed as:

$$\Lambda_{1/4w} = \arccos \frac{M_D}{M_c} = 10.5^\circ.$$

Additionally, a security factor  $s = 1.5$  is considered. The sweep is thus set to  $15^\circ$ .

The [angle of attack at the root](#)  $\alpha_{\text{root}}$  can be determined if the 3D lift coefficient is known:

$$C_{LW} = C_{LW_\alpha} [\alpha_{\text{root}} - \alpha_{L_{0,\text{root}}}],$$

where  $\alpha_{L_{0_{\text{root}}}} = -1.27^\circ$  is the zero lift angle of attack of the wing considering a twist angle of  $-1^\circ$ , as previously discussed. The slope of the 3D lift coefficient  $C_{L_{W\alpha}}$  is computed as:

$$\left\{ \begin{array}{l} \beta = \sqrt{1 - M^2} = 0.714; \\ k = \frac{\beta c_{lw\alpha}}{2\pi} = 1.085; \\ \tan \Lambda_\beta = \frac{\tan \lambda_{1/4}}{\beta} = 0.375; \end{array} \right. \Rightarrow C_{L_{W\alpha}} = \frac{2\pi/\beta}{\frac{2}{\beta AR} + \sqrt{\left(\frac{1}{k \cos \Lambda_\beta}\right)^2 + \left(\frac{2}{\beta AR}\right)^2}} = 6.02 \text{ rad}^{-1}.$$

Knowing that the lift coefficient of the wing  $C_{L_W} = 0.34$ , the angle of attack at the root is thus computed. It is equal to  $2^\circ$ . The empirical relation of the lift curve is represented in Figure 5.3.

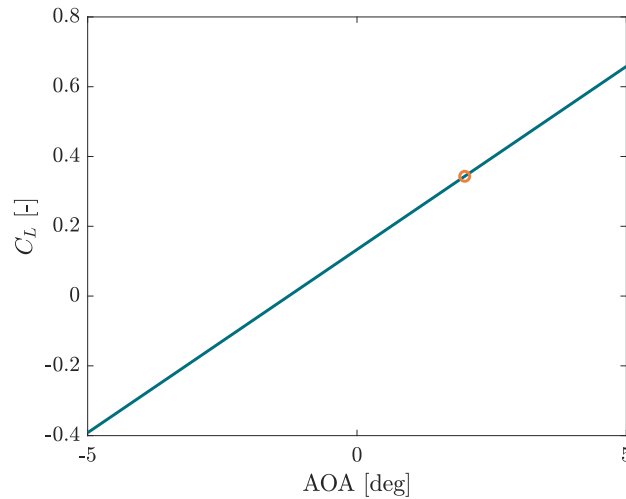


Figure 5.3: Wing lift coefficient as a function of the angle of attack at root. The orange ring is the design lift coefficient.

The mean aerodynamic chord MAC and the position of the aerodynamic center ( $x_{ac}; y_{ac}$ ) can finally be determined. Their values are respectively 3.64 ft and (0.95 ft; 4.77 ft). It can be noted that  $x_{ac}$  is graphically determined [14] since it depends on the aspect ratio, the compressibility effects and the sweep angle, contrary to MAC and  $y_{ac}$  which are analytically computed.

The dimensions of the wing are represented in Figure 5.4 and its characteristics are summarized in Table 5.2.

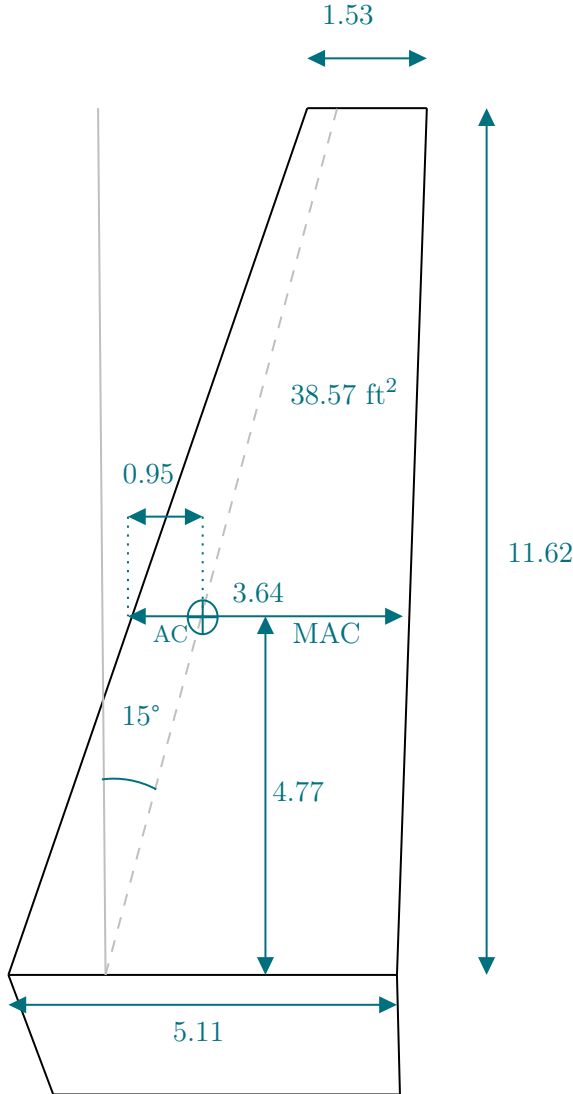


Figure 5.4: Wing geometry, dimensions in feet.

Table 5.2: Wing geometry parameters.

Property	Value
Aspect Ratio	7
Taper Ratio	0.3
$\alpha_{\text{root}}$	$2^\circ$
$\alpha_{\text{tip}}$	$1^\circ$
$C_{L_{W\alpha}}$	$6.02 \text{ rad}^{-1}$
$C_{L_W}$	0.34

## Flaps design

The goal of the flaps is to increase the lift in order to take off (or land) before the end of the runway. One approach is to find the maximum lift coefficient needed to take off exactly at the end of the runway and then design the flaps according to that. Another approach is to choose the flaps, design them and check if the requirements are verified. The second approach is chosen here applying Raymer’s methodology [9].

First, the maximum lift coefficient without flaps is determined as:

$$(C_{L_{\text{max}}})_{\text{clean}} = 0.95 \cos \Lambda_{1/4} \frac{(c_{l_{\text{max}}})_{\text{root}} + (c_{l_{\text{max}}})_{\text{tip}}}{2} \cdot 1.1 = 1.65,$$

with  $(c_{l_{\text{max}}})_{\text{tip}} = 1.55$  and  $(c_{l_{\text{max}}})_{\text{root}} = 1.75$  for a NASA SC(2)-0412 airfoil [14]. Single slotted flaps are



used because they have a light mechanism and can sufficiently increase the lift coefficient. Plain flaps have been considered but they do not produce enough lift to allow take-off. According to Raymer [9], the general flaps chord ratio (ratio of the chord taken by the flaps) is around 0.3 and the flaps span ratio (ratio of the span taken by the flaps) is around 0.4. The flapped area ratio is then equal to 0.42. Equation (5.1) expresses the maximum lift coefficient with flaps.

$$C_{L_{\max}} = (C_{L_{\max}})_{\text{clean}} + \Delta C_{L_{\max}} \quad \text{with} \quad \Delta C_{L_{\max}} = 0.9 \Delta c_{l_{\max}} \left( \frac{S_{\text{flapped}}}{S_W} \right) \cos \Lambda_{\text{H.L.}}, \quad (5.1)$$

where  $\Delta C_{L_{\max}}$  is the maximum increment of lift using flaps and  $\Delta c_{l_{\max}}$  is the maximum increment of lift depending on the flaps deflection and the type of flaps. The sweep angle of the hinge line  $\Lambda_{\text{H.L.}}$  is equal to  $7.4^\circ$ . The maximum lift coefficient at take-off  $C_{L_{\max, \text{TO}}}$  and landing  $C_{L_{\max, \text{LDG}}}$  can thus be computed. Considering a  $20^\circ$  flap angle,  $C_{L_{\max, \text{TO}}}$  is equal to 2.02 while  $C_{L_{\max, \text{LDG}}} = 2.23$  is obtained with a  $40^\circ$  flap angle.

The take-off and landing lift coefficients are respectively computed at the lift-off velocity  $V_{\text{LOF}} = 1.1 \cdot V_{\text{stall, TO}}$  and at the touch down velocity :  $V_{\text{TD}} = 1.1 \cdot V_{\text{stall, LDG}}$ . The stall velocity is expressed as:

$$V_{\text{stall}} = \sqrt{\frac{2 \cdot W_{\text{TO(LDG)}}}{\rho_0 \cdot C_{L_{\max, \text{TO(LDG)}}} \cdot S_W}},$$

and the lift coefficients can finally be computed:

$$\begin{cases} C_{L_{\text{TO}}} = \frac{2W_{\text{TO}}}{\rho S_w V_{\text{LOF}}^2} = 1.62; \\ C_{L_{\text{LDG}}} = \frac{2W_{\text{LDG}}}{\rho S_w V_{\text{TD}}^2} = 1.84. \end{cases}$$

### 5.1.3 Tail

#### Design choices

The tail of an aircraft plays a critical role in providing stability and control. For The Drop, a V-tail design is chosen instead of a classic design.

The main drawback of that configuration is that the design and construction of a V-tail are more complex than for a classic tail as they require specialized skills and techniques to manage the coordination of the control surfaces. It is also a more complex control configuration for maneuvers. In addition, a V-tail can provide less stability compared to a classic tail design, which can make the aircraft even more challenging to fly [15].

However, the advantages outweigh the disadvantages. First, a V-tail design provides a more aerodynam-

ically efficient shape compared to a classic tail design. The V-shape indeed reduces the amount of drag since there is less wetted surface area. This can improve the aircraft's overall efficiency and performances [9]. Furthermore, a V-tail design requires less material than a classic tail design, which can result in a lighter overall aircraft.

## Methodology

The geometry of the tail is determined in order to assure stability and maneuverability of the aircraft. The design steps follow Raymer's methodology [9]:

1. determine the required horizontal and vertical surfaces to assure maneuverability using the volume tail coefficients;
2. compute the tail total surface and dihedral angle;
3. verify stability and reiterate if necessary.

The volume coefficients are important parameters which allow to get an idea of the stability of the plane. These coefficients are defined as:

$$\begin{cases} c_{HT} = \frac{l_{HT}S_{HT}}{c_{w,MAC}S_W} = 0.6; \\ c_{VT} = \frac{l_{VT}S_{VT}}{b_W S_W} = 0.09, \end{cases}$$

where  $S_W$  is the area of the wing,  $b_W$  is the span of the wing,  $l_{HT}$  is the tail arm *i.e.* the distance between the tail quarter chord and the wing quarter chord,  $l_{VT}$  is the fin arm, which is equal to  $l_{HT}$  for a V-tail,  $S_{HT}$  is the horizontal surface of the tail,  $S_{VT}$  is the vertical surface of the tail and  $c_{w,MAC}$  is the mean aerodynamic chord of the wing.

Based on results of tail volume ratio from Raymer [9], the horizontal tail volume ratio is set to the average value of 0.6. Knowing the wing surface, the wing mean aerodynamic chord and the tail arm, the horizontal surface is computed as:

$$S_{HT} = \frac{c_{w,MAC}}{l_{HT}} S_W c_{HT} = 9.05 \text{ ft}^2.$$

To determine the vertical surface, the vertical volume tail ratio must be computed. It is found that it is equal to 0.09, following Torenbeek [16]. Knowing the wing surface, the wing span and the tail arm, the vertical surface is given by:

$$S_{VT} = \frac{b_W}{l_{VT}} S_W c_{VT} = 8.66 \text{ ft}^2.$$

Intuitively, the total surface of the tail would be found using the projection of the horizontal and vertical surfaces with some trigonometry relations. However, NASA report 823 [17] showed that the total surface of the V-tail should be upsized to the sum of the horizontal and vertical surfaces to obtain the same performances.

$$S_T = S_{HT} + S_{VT} = 27.86 \text{ ft}^2,$$

and the dihedral angle is given by:

$$\Gamma = \arctan \left( \sqrt{\frac{S_{VT}}{S_{HT}}} \right) = 44.4^\circ.$$

As the aspect ratios are very different between the horizontal tail (3-6) and the fin (0.7) [14], a trade-off is made. The aspect ratio is set to 4 as the horizontal projection of the tail is considered the most important in the choice of parameters. Finally, the taper ratio is set to 0.6 as the V-tail is somewhere between a conventional tail and a T-tail [9]. A sweep angle  $5^\circ$  larger than that of the wing is chosen [14]. Geometric parameters that can be computed are listed in Table 5.3. Also, the tail and all geometric values are schematically represented in Figure 5.5. Note that distances, such as the span, are measured along the tail and not in the reference frame.

### Airfoil profile

Since the aircraft center of gravity moves during cruising flight, the airfoil section must be able to create sometimes a positive and sometimes a negative lift. This requirement necessitates the tailplane to behave similarly in both positive and negative angles of attack [18]. Moreover, it should have a low thickness to avoid drag generation from both vertical and horizontal surfaces [14]. The tailplane must also be clean of compressibility effects. To ensure that, the tail lift coefficient is chosen to be less than the wing lift coefficient. This objective is fulfilled by selecting an airfoil profile thinner than the wing airfoil (12%) [18]. Therefore, a NACA0010 airfoil profile is selected for the V-tail.

Table 5.3: Tail geometry parameters.

Property	Value
Aspect Ratio	4
Taper Ratio	0.6
Rudder chord ratio	0.35
Rudder span ratio	0.7

---

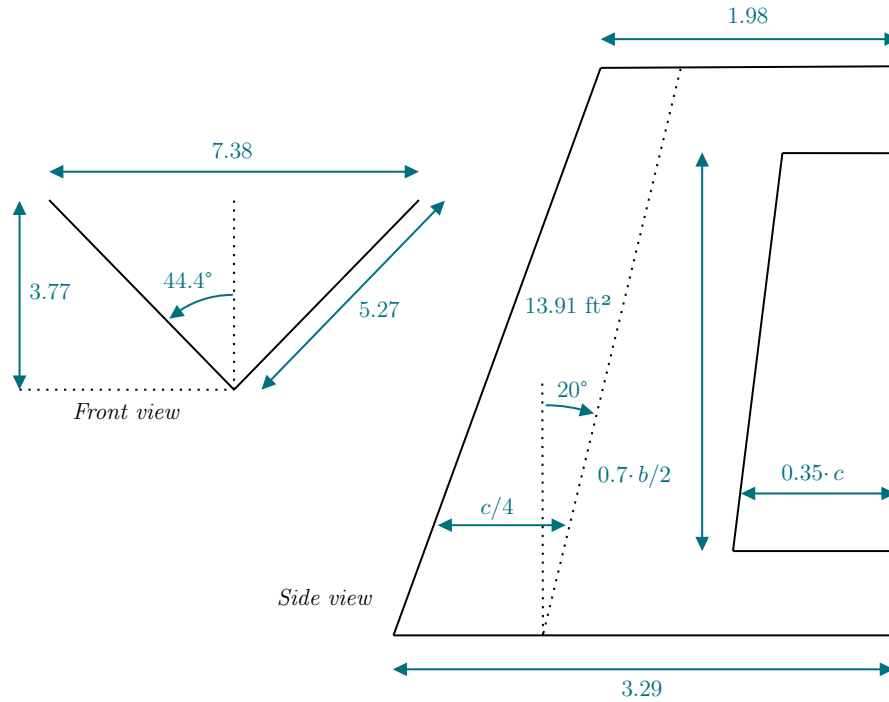


Figure 5.5: Tail geometry, dimensions in feet.

## Control surfaces

As a V-tail configuration is chosen, the control surfaces of horizontal and vertical tailplanes are merged into single control surfaces called ruddervators. This surface allows control for pitching and yawing momentum. The geometrical design of this control surface is made considering the methodology and typical values of Raymer [9] for the rudder as this control surface is considered more important than the elevator control surface. The surface is tapered in chord by the same ratio as the tail surface to allow spars to be straight-tapered rather than curved [9]. The main challenge of this control surface is to be sized to ensure take-off performances to satisfy Federal Regulations [19], while avoiding stall during the cruise. Moreover, the rudder contribution must enable landing in crosswind conditions, which is studied in Section 9.5.1.

The geometrical parameters are represented in Figure 5.5 and the maximum deflection angle of the ruddervator in both directions to ensure maneuverability is  $30^\circ$  following Sadraey [18]. For the next derivatives and calculations, the horizontal and vertical surfaces of the ruddervator are considered independently for this stage of the study, as assumed in the NASA report 823 [17]. Some complex effects leading to loss of control must be studied in the wind tunnel, thus simplifications are made for the latter results. The surface ratio  $S_R/S_F$  is 0.175.

### 5.1.4 Lift and drag coefficient

At cruise, the wing and the V-tail must compensate the weight of the aircraft by generating lift. However, since the main goal of the tail is to balance the aircraft, it only generates a small portion of the total lift. The different lift contributions can thus be computed thanks to a balance of the forces and moments represented in Figure 5.6. Note that the asymmetric shape of the fuselage creates a nonzero aerodynamic moment and lift. The latter are neglected at this stage of the design.

Knowing the configuration of The Drop, Eq. (5.2) gives the force and moment equilibrium. Thus, the ratio of lift generated by the wing and V-tail is respectively 80 % and 20 %.

$$\begin{cases} L_W + L_T = W; \\ (x_{CG} - x_{AC,W}) \cdot L_W = (x_{AC,T} - x_{CG}) \cdot L_T. \end{cases} \quad (5.2)$$

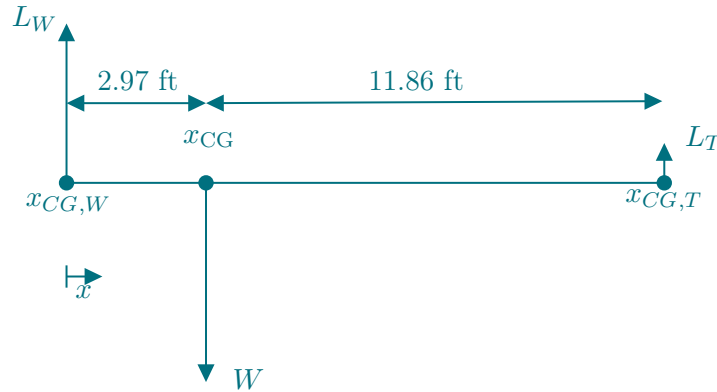


Figure 5.6: Force balance.

As already mentioned, the lift coefficient of the tail is designed to counterbalance the moment generated by the weight of the aircraft and the lift of the wing. Taking into account the arm corresponding to the distance between the center of gravity and the pressure center of the tail, the lift coefficient is fixed to 0.36 and the angle of attack of the tail to  $4^\circ$  to reach this lift coefficient. For a V-tail, the effective lift coefficient is given by [17]:

$$C_{L_{tail}} = C_{L_N} \cos(\Gamma),$$

where  $C_{L_N}$  is the lift coefficient normal to the surface of the Tailplane and  $\Gamma$  the dihedral angle of the tail. The angle of attack of the tail plain is computed using the normal lift coefficient to obtain the effective lift coefficient required. Based on experimental results [20], the angle of attack is set to  $4^\circ$ .

Knowing the lift coefficient of the wing and of the V-tail, the total lift coefficient is [9]:

$$C_L = C_{L_W} + \frac{S_T}{S_W} C_{L_T} = 0.425.$$

The drag coefficient is estimated as:

$$C_D = C_{D_0} + \frac{C_L^2}{e\pi AR} = 0.027,$$

where  $C_{D_0} = 0.017$  is the part of the drag independent of the lift. It is the middle value taken in the range 0.014-0.020 for high-subsonic jet [14]. The Oswald efficiency factor  $e$  is evaluated as [9]:

$$e = 1.78(1 - 0.045AR^{0.68}) - 0.64 = 0.84.$$

A first estimate of the total drag of the plane in cruise can thus be computed, and therefore the needed thrust generated by the engine. This first estimation is  $D = T = 449.6$  lbf.

## 5.2 Fuselage

### 5.2.1 Fuselage design choices

An elliptical fuselage design is chosen. That kind of fuselage indeed displays some advantages compared to a classical circular cross-section [21]. An elliptical fuselage provides a higher level of structural efficiency compared to other shapes as it can support more weight with less material. This can result in a lighter overall aircraft, which can improve its performances and efficiency. In addition, an elliptical fuselage can provide a more stable platform for the aircraft's systems, as the rounded shape helps to distribute loads more evenly.

Nevertheless, choosing an elliptical fuselage comes with drawbacks as well. The design and construction of an elliptical fuselage is indeed more complex than other shapes. This increases manufacturing costs. Moreover, compared to a circular shape, the stress on the fuselage is not as evenly distributed. It adds the complexity of having to take into account the fatigue damage it can cause. In fact, at each climb and descend, the not evenly distributed stress changes around the fuselage and in the long term, it can cause fatigue cracks at the location of higher stress concentration.

Additionally, as already mentioned, The Drop is a lifting body but its effects are not yet taken into account. They are studied later by doing a trade-off concerning the percentage of lift that the fuselage can

generate. The fuselage thus has an asymmetric shape, as observed in Figure 5.7a.

### 5.2.2 Fuselage geometry

The dimensions of the fuselage are displayed in Figure 5.7.

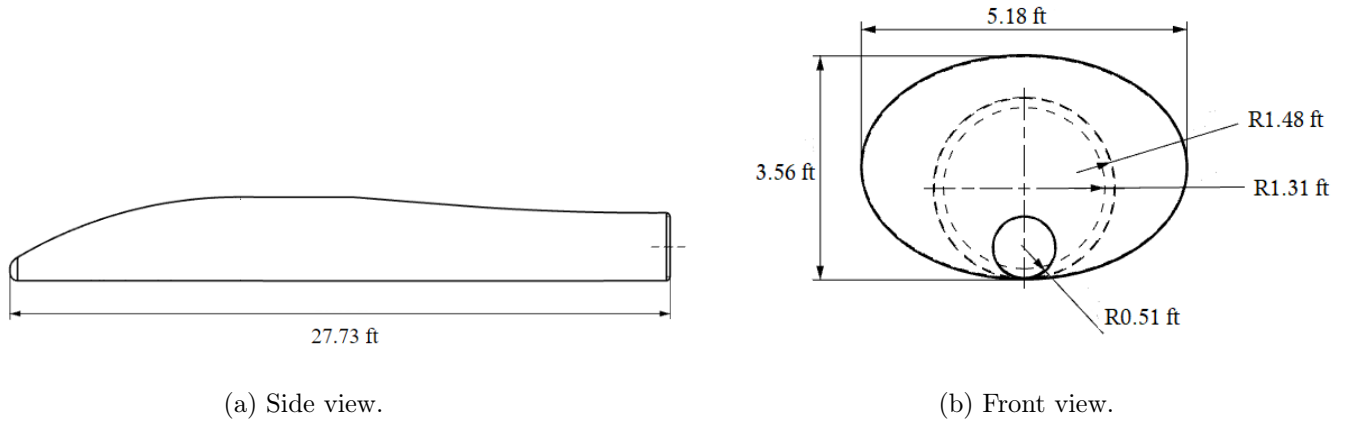


Figure 5.7: Fuselage geometry.

### 5.2.3 Internal arrangement of the fuselage

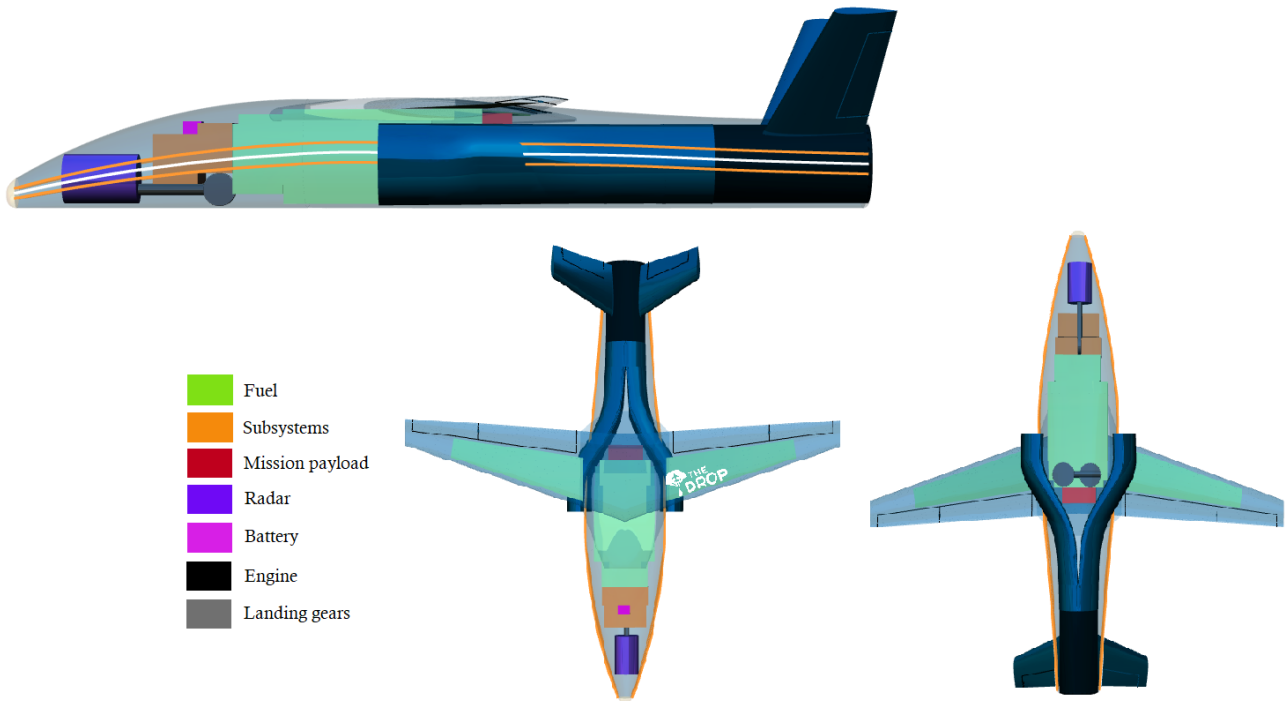


Figure 5.8: Internal arrangement of the fuselage.

The internal arrangement of the fuselage is displayed in Figure 5.8. The sensors are kept at the front of the aircraft in order to reduce the impact of mechanical vibrations coming from the engine, which is located at the very back of the fuselage. The fuel that cannot be stored in the wing is kept inside the fuselage. The latter represents 80% of the total volume of fuel, which corresponds to 71 ft<sup>3</sup>. The fuel tank is positioned around the center of gravity in order to minimize the imbalance when the fuel is consumed during the flight.

## 5.3 Propulsion System

The thrust provided by the engine must power the aircraft during all the phases of the flight and more specifically during critical phases of the flight such as take-off and landing. Moreover, the engine's weight and the fuel consumption of the latter directly impact other parts of the aircraft's design process such as the stability.

### 5.3.1 Engine selection

Since The Drop has to fly at transonic speed and at high altitude as stated in Table 2.1, a turbofan engine is chosen. In fact, turbofan engines are designed to operate over a wide range of speeds and altitudes. Therefore, the flexibility needed for The Drop to adapt to changing conditions in disaster zones can be achieved.

The weight as well as the specific fuel consumption are critical parameters that must be taken into account during the selection process of the engine. In fact, higher fuel consumption definitely leads to a higher aircraft weight. A compromise between fuel consumption and weight of the engine must then be made. Performances in cruise are here considered as usually this phase of the flight is the longest. In addition, the selected engine must be able to support the aircraft during critical phases of the flight such as take-off, landing and climbing while respecting the requirements listed in Table 2.1.

A single engine configuration is chosen. Despite the lack of redundancy and power limitation, this engine configuration has many advantages. Indeed, it simplifies the design of the aircraft because it is no longer necessary to provide complex systems to control and coordinate several engines, thus reducing the risk of mechanical failure. In addition, this configuration drastically reduces the weight of the propulsion system, which in turn improves the performances and efficiency of the aircraft. Furthermore, a single engine configuration is typically cheaper to purchase, install and maintain than multiple engines. The aircraft can thus be more affordable for disaster response organizations and aid agencies. The fact that there is no human being on board limits the need of redundancy. In case of engine failure and if the aircraft cannot reach an airport, the only cost would be the one of the aircraft. Therefore, costs savings, simplicity and performances outbalance the drawbacks.



A special focus is made on the engines from Williams international [22]. Williams international offers two engines that could be suitable for the mission. Their characteristics are listed in Table 5.4. Note that the specific fuel consumption of the engine is not provided by the engine manufacturer so an estimation [23] is made based on Eq. (5.3).

$$SFC = SFC_0 \sqrt{\theta} (1 + M)^n, \quad (5.3)$$

where  $\theta$  is the temperature ratio,  $M$  is the Mach number,  $n$  is set to 0.7, as advised in the Reference [23] and  $SFC_0$  is set to 0.53, based on the SFC of a similar engine FJ44-1A multiplied by the mass ratio of the two engines. The SFC obtained with this method for both engines is rounded to 0.7.

Both engines could satisfy the mission requirements since the first approximation of the drag that must be compensated is equal to 449.6 lbf. The FJ44-3AP engine would operate at 56% of its maximum available thrust whereas the FJ44-4A would operate at a lower regime of operation of approximately 30%. The latter is therefore oversized for the needs of the mission. The JT15D [24] engine from Pratt & Whitney could also be a good candidate for The Drop. However, because of its high specific fuel consumption and weight, it is not chosen. Therefore, the FJ44-3AP engine is selected.

Table 5.4: Possible engines for The Drop.

Engine	Static Thrust [lbf]	T/W [-]	TSFC [lb/(lbf·h)]	BPR [-]	Dry mass [lbf]
<b>FJ44-3AP</b>	<b>3,052</b>	<b>5.9</b>	<b>0.7</b>	<b>4.1</b>	<b>516</b>
FJ44-4A	3,621	5.4	0.7	4.1	670
JT15D	3,045	5	0.87	3.3	632

The variation of the maximum available thrust as a function of the altitude and the Mach number is unknown during the preliminary design study. The latter is approximated for different Mach numbers by using the thrust model of modern two-shaft turbofan engines proposed by Bartel and Young [25]. Equation (5.4) expresses the available thrust as a function of altitude and velocity.

$$T = T_0 \left( A - \frac{0.377(1 + \lambda)}{\sqrt{(1 + 0.82\lambda)G}} Z \frac{P_{\text{amb}}}{P_{\text{amb},0}} M + (0.23 \cdot 0.19 \sqrt{\lambda}) X \frac{P_{\text{amb}}}{P_{\text{amb},0}} M^2 \right), \quad (5.4)$$

where

$$\begin{cases} A = -0.4327 \left( \frac{P_{amb}}{P_{amb,0}} \right)^2 + 1.3855 \frac{P_{amb}}{P_{amb,0}} + 0.0472; \\ X = 0.1377 \left( \frac{P_{amb}}{P_{amb,0}} \right)^2 - 0.4374 \frac{P_{amb}}{P_{amb,0}} + 1.3003; \\ Z = 0.9106 \left( \frac{P_{amb}}{P_{amb,0}} \right)^2 - 1.7736 \frac{P_{amb}}{P_{amb,0}} + 1.8697. \end{cases}$$

The static thrust at sea level is  $T_0$ ,  $\lambda = 4.1$  is the by-pass ratio,  $G = 1.1$  is an adimensional number according to Torenbeek [16],  $M$  is the Mach number and  $\frac{P_{amb}}{P_{amb,0}}$  is the pressure ratio. The latter is computed as:

$$\frac{P_{amb}}{P_{amb,0}} = \left( 1 + \frac{L_b}{T_b} h \right)^{\frac{-g \cdot M_M}{L_b \cdot T_b}},$$

where  $L_b$  is the temperature increment,  $T_b$  the temperature at sea level,  $h$  the altitude,  $g$  the gravity constant and  $M_M$  the molar mass of air.

The results are highlighted in Figure 5.9. Only four Mach numbers are represented: the static case (Mach 0), the range in which the takeoff takes place (Mach 0.1 - Mach 0.2) and the cruise condition (Mach 0.7). As it can be seen in Figure 5.9, the available thrust at cruise altitude for the FJ44-3AP is equal to 803 lbf.

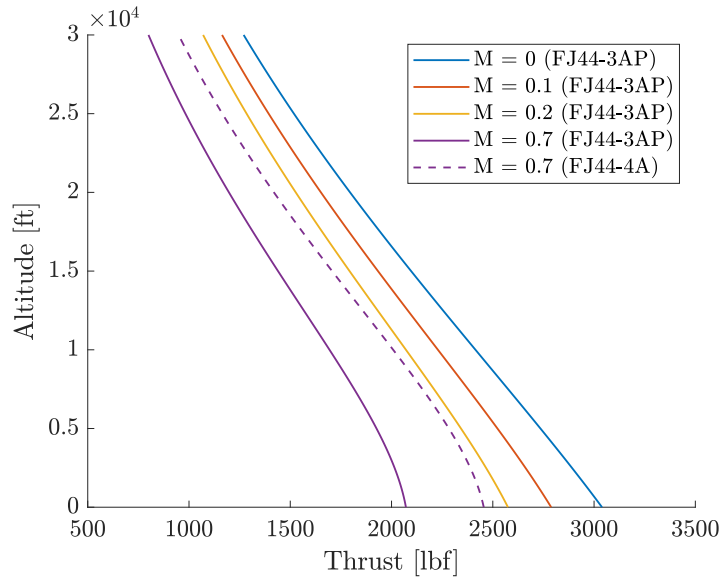


Figure 5.9: Available thrust as a function of the flight altitude and velocity.

### 5.3.2 Air intakes

The engine is located at the back of the fuselage and inside it to avoid the interference effects and limit the size of the V-tail. This configuration requires the use of air intakes which can be positioned in different ways.

The design of the air inlets has to be thought through in order to minimize losses inside the duct. A massive flow separation can indeed occur downstream the first bend if it is too sharp. This phenomenon leads to high losses in the total pressure and thus needs to be avoided. To this extent, the ducts are given a smooth S-shape, as seen in Figure 5.10a [26]. According to The Aircav [27], side inlets enable to use shorter ducts and thus minimize the eventual losses inside of them. This design is therefore chosen for the air intakes of The Drop. Those are placed under the wing, in the wing-root area. The frontal area of each inlet is equal to  $2.69 \text{ ft}^2$  which is equivalent to half the area of the engine. The two ducts later meet, inside the fuselage, a little bit upfront of the engine, as observed in Figure 5.10a.

The ducts are offset from the fuselage of a few inches, as shown in Figure 5.10b, in order to avoid ingesting the boundary layer of the flow in the intakes. The flow should indeed be free of turbulence in order to be able to reach the desired efficiency of the engine.

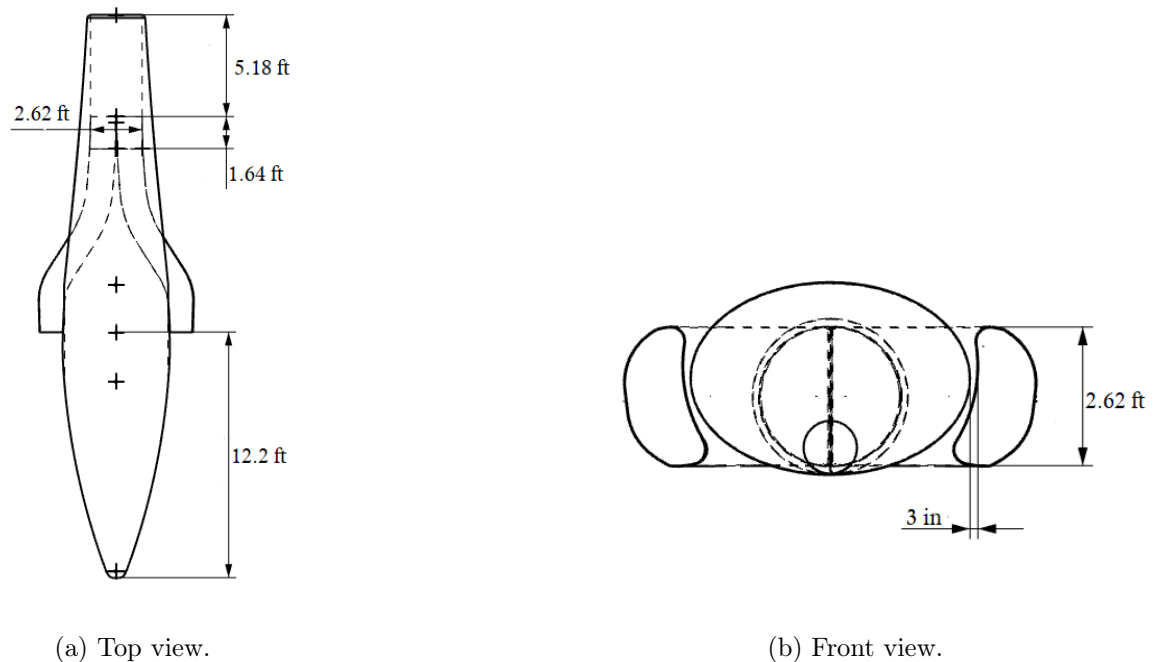


Figure 5.10: Fuselage and air intakes geometry.

## 5.4 Landing gear

The landing gears of The Drop must withstand high levels of efforts for a high number of cycles. Therefore, it is essential for them to have a high fatigue resistance. The chosen configuration is a tricycle landing gear as the mass of the aircraft is small enough. This configuration is made of two wheels behind the center of gravity and an auxiliary wheel supporting the nose of the aircraft. The main advantage of this configuration is the

static and dynamic stability that it offers on the ground.

### 5.4.1 Landing gear position and characteristics

The configuration of the landing gear must satisfy different requirements [9]:

- the tip back angle should be between 15° and 25°;
- the tail should not hit the ground during landing;
- the nose wheel should carry between 8% and 15% of the aircraft's weight.

The landing gear can either be fixed or retractable. Regarding the cruise speed of the aircraft, the choice of having retractable landing gears is non negotiable. Fixed landing gears would indeed induce too much drag in cruise condition and therefore impact the general performances of The Drop.

### 5.4.2 Design

First, the landing gear's height must be large enough to avoid hitting the ground with the tail of the aircraft. According to Raymer [9], to prevent that situation in a tricycle configuration, the theta angle  $\theta$ , which is the angle formed between the main wheel position and the center of gravity of the aircraft, must always be greater or equal than the tip back angle. Additionally, it must range between 16° and 25°. Moreover, the take-off angle should be lower than the tip back angle in order to avoid the tail of the aircraft to touch the ground while taking-off. The take-off angle should range between 1° and 15°. It is computed as:

$$\alpha_{take-off} = \frac{1}{C_{L0}} [(C_{l,max})_{cruise} - C_{l,cruise} - p(C_{l,max})_{take-off}] = 3.55^\circ,$$

where  $p$  is a margin approximated to 0.15.

Finally, the turning radius is computed as:

$$r = E \tan(90 - \beta) + f/2,$$

where  $E$  is the wheel base,  $\beta$  the gear steering angle, which is assumed to be 50°, and  $f$  the wheel-track. The characteristics of the landing gears are summarized in Table 5.5 and represented in Figure 5.11.

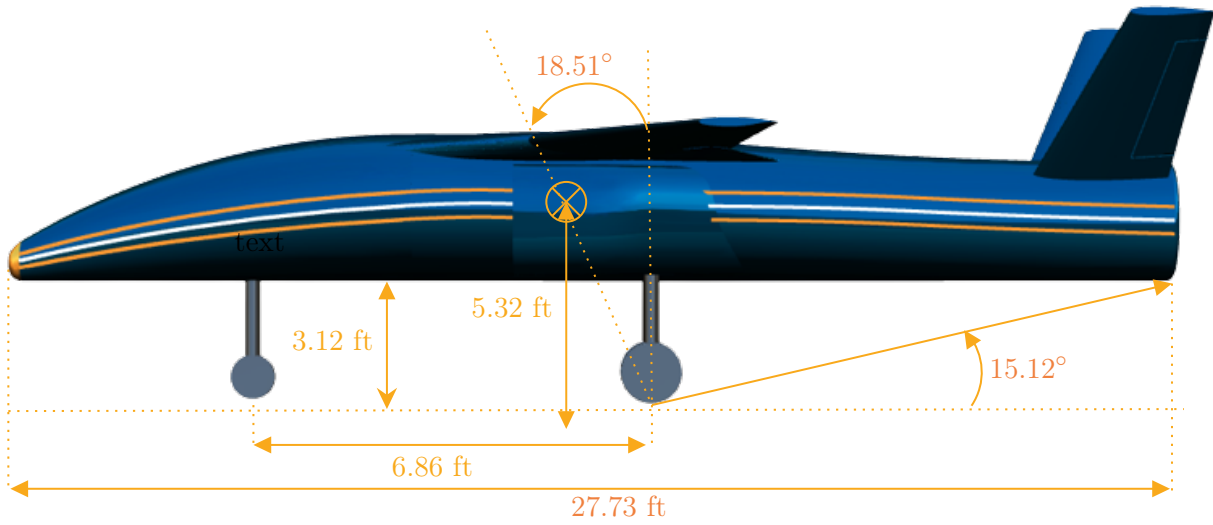


Figure 5.11: Landing gears main dimensions.

Table 5.5: Characteristics of the tricycle landing gear system during taxi at MTOW.

Parameter	Value
Force taken by the front wheel	1,040.41lbf
Force taken by the rear wheel	2,947.92 lbf
Wheel-track	3,03 ft
Turning radius	6.78 ft
Overturn angle	62.8°

### 5.4.3 Characteristic of the tires

The tires of a tricycle landing gear must sustain the different loads that manifest during landing, take-off and ground operations. According to Raymer [9], the back wheels have to support 85% of the total weight whereas the nose wheel has to support the remaining 15%. The dimensions of the wheels and tires are summarized in Figure 5.12. The type of tires of the nose and back wheels are respectively Type III 5.00-4 and Type III 7.00-8.

### 5.4.4 Shock absorber

Shock absorbers absorb the energy and dissipate it during landing and take-off, thus reducing oscillations and deformation. The chosen shock absorber is an oleopneumatic shock absorber. This mechanism can be described

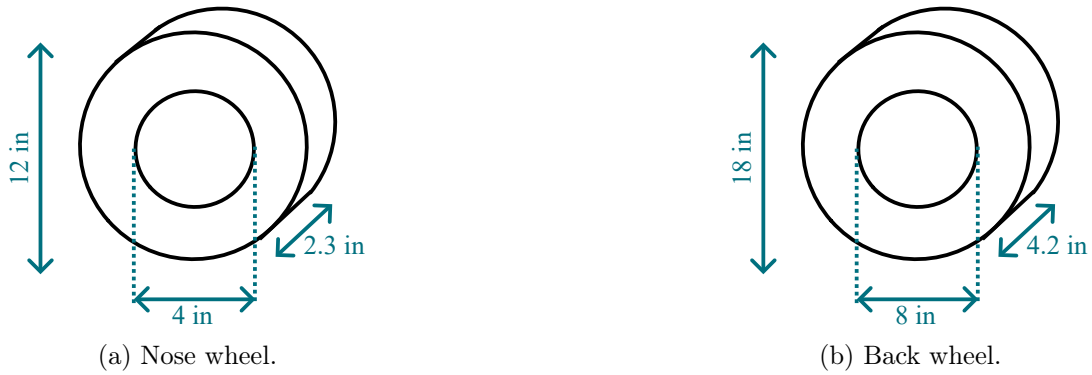


Figure 5.12: Wheels and tires dimensions.

as a cylindrical piston device that is able to damp out vertical oscillations. The oleopneumatic shock absorber combines both damping effect and spring function.

In order to design the shock absorber, some parameters of the aircraft have to be assumed or determined empirically. The sink velocity  $V_{vertical}$  is set to 15 fps in order to meet the requirements at landing at maximum take-off weight. According to Raymer [9], the shock absorber efficiency for an oleopneumatic with a fixed orifice  $\eta$  ranges between 0.65 and 0.8. The efficiency of the tire  $\eta_t$  is fixed at 0.4. The gear load factor for general aviation aircraft is  $N = 3$  and the stroke of tire  $S_t$  is equal to half the diameter of the wheel minus the rolling radius. According to Raymer [9], the value of the stroke should be increased by 1 in as a safety margin. The stroke is computed as:

$$S = \frac{V_{vertical}^2}{2gN\eta} - \frac{\eta_t}{\eta} S_t + 1.$$

The corresponding values for the stroke of the landing gears are listed in Table 5.6.

Table 5.6: Shock absorbers characteristics.

	Stroke of tire [ft]	Stroke [ft]
Nose landing gear	0.79	1.03
Main landing gear	1.46	0.96

## 5.5 Avionics, subsystems and sensors

The Drop is designed to be an autonomous aircraft. The main advantage of this configuration is its versatility. There is no need for a qualified remote pilot in contrast with a remotely controlled aircraft. On the one hand, The Drop can therefore be deployed without mobilizing any skilled personnel that could be useful in the management of other parallel missions. On the other hand, the response time can, as a result, be decreased. In fact, a smaller ground crew must be enlisted to take-off [28].

In order to ensure that The Drop fulfills its mission, numerous avionics, subsystems and sensors must thus be included. The avionics provide accurate information about the navigation. The function of these devices is thus to check that the aircraft flies properly. The minimum flight and navigation instruments required for an autonomous aircraft are specified by FAR regulations [19].

The subsystems and the sensors include the communication and identification instruments. They are specified in the proposal from AIAA [4]. Selecting the right sensors is thus important to successfully fulfill the mission. The LIDAR must indeed be able to accurately identify the position of the victims in order to efficiently deliver the packages. A proposed EO/IR/LIDAR is the Teledyne fir STAR SAFIRE 380-HD [29]. It is a LIDAR which is used for patrol and protection. It can be used at up to 50,000 ft and weights less than 100 lbs. Its resolution is 720p/1080p HD. Regarding these characteristics, that LIDAR ensures that the victims location is correctly estimated, consequently the packages are delivered more accurately. The other sensors and subsystems are not precisely selected since their choice is not a key for the fulfillment of the mission.

## 5.6 Payload release

The aim of The Drop is to provide communication radio and drinking water to disaster victims assuming that each group of victims consists of a maximum of two individuals. Additionally, it is presumed that victims are stranded in immediate need of drinking water and will remain stranded for at least six additional hours until helps arrive. According to existing literature, multiple payload release systems exist. The most commonly used system is the one identical to the payload release system of the F-35 represented in Figure 5.13a. It consists of a door located under the aircraft allowing the release of the payload. Another solution is a door that acts as a launch pad for the payload. This solution is implemented in the C-130 shown in Figure 5.13b.

Each of the mentioned payload release system has its pros and cons. They are listed in Table 5.7.



(a) F-35 payload release system [30].



(b) C-130 payload release system [31].

Figure 5.13: Review of existing payload release system.

Table 5.7: Pros and cons of each payload release technique.

Bay door release	Back door release
+ High altitude release with parachute	+ Low altitude release without parachute
+ Convenient for aerodynamic payload	+ Convenient for all types of payload
+ Possible payload segmentation	+ Possible payload segmentation
+ Limited additional drag when door is open	– Significant drag when door is open

Regarding listed pros and cons of Table 5.7, a bay door release system at high altitude is chosen. The main advantage regarding the mission is that The Drop will not have to decrease its altitude in order to release the packages. This allows to increase the loiter range which is, as a reminder, the secondary mission of the AIAA proposal [4].

### 5.6.1 Survival kit composition

The Drop is able to deliver survival kits to a group of maximum two people. The volume allocated to the payload in the fuselage is  $6.62\text{ft}^3$ . Each survival kit is composed of water packs, a survival kit and a blanket. In addition, a satellite phone, GARMIN inReach Mini 2 [32], is included in the delivered package in order for victims to communicate with rescue services. In fact, this satellite phone is able to communicate with satellite from the GPS and Galileo constellation which covers the entire Earth’s surface. The water packs fill up the empty space around the satellite phone and the survival kit as they are soft. The content of one capsule is displayed in Figure 5.14.



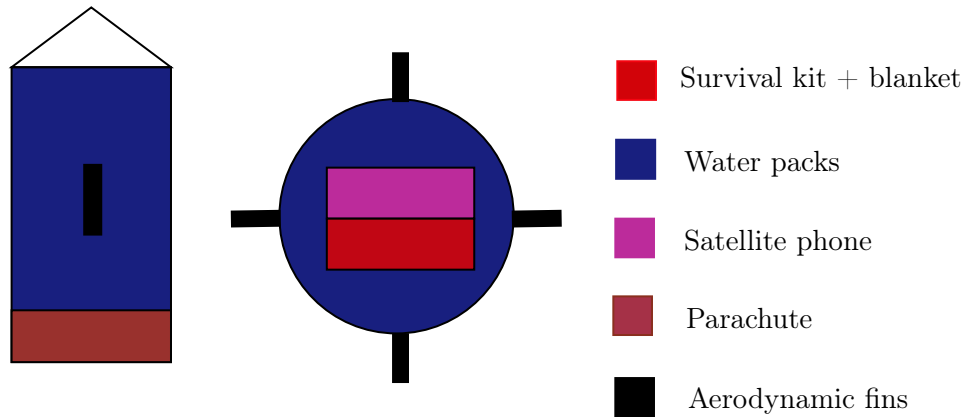


Figure 5.14: Content of the capsules: side view on the left and top view on the right.

### 5.6.2 Design and internal arrangement of the survival kits

As the survival kits are dropped from 30,000 ft, they must be integrated into an aerodynamic device in order to be precisely dropped where victims are lying.

As the volume of the payload is limited, only a certain number of devices can be stored in The Drop. In view of the space allocated to the payload in the fuselage, 63 aerodynamic devices can be stored in it. The position of the box containing the capsules in the fuselage is shown in Figure 5.8. Moreover, the arrangement of the capsules is shown in Figure 5.15. The front and side views of the capsule box correspond to the view obtained when looking at The Drop respectively from the front and the side. On the outside of the aerodynamic dynamic devices are placed fins in order to control the capsule during its fall to the target. Inside the aerodynamic device, an altimeter as well as a parachute are stored. The altimeter will allow to deploy the parachute and slow down the payload at the end of its free fall towards the victims.

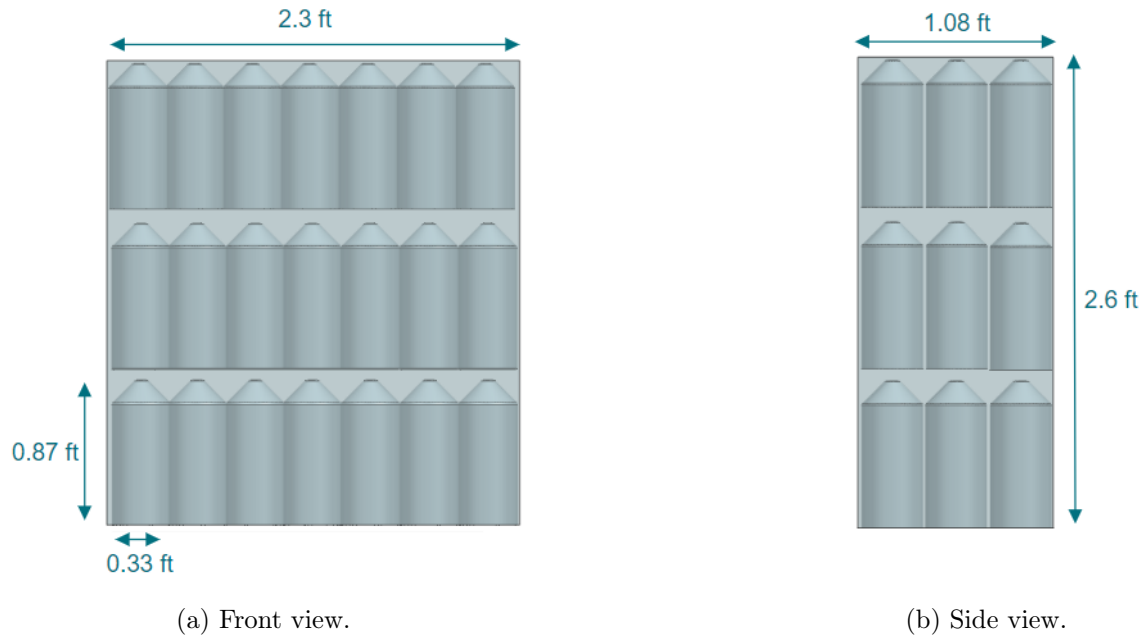


Figure 5.15: Arrangement of the capsules inside the fuselage.

### 5.6.3 Delivery

The delivery of the payload is operated in several steps. First, a certain number of capsules are dropped from the aircraft. This number can be controlled thanks to the presence of rails between the capsules, which enable to avoid dropping all of them at the same time. Then, the aerodynamic fins on the sides of the capsule are used to move it towards the right direction. Finally, using an altimeter, the parachute is deployed to slow down the free fall of the capsule and damp its impact on the ground. The hardware controlling the fins is supposed to be simple as it is assumed that there will always be someone able to pick up the capsules in the surroundings.

## 5.7 Weights and centers of gravity

The total weight is computed precisely using empirical relationships provided by Raymer [9]. The resulting weight of each main component is given in Table 5.8. The position of the centers of gravity of the different elements of The Drop are also displayed in Table 5.8. The longitudinal and vertical distributions of the different centers of gravity are shown in Figure 5.16. The computations of the position of the centers of gravity are detailed in Section 6.

Table 5.8: Weight estimation and position from nose of the centers of gravity of The Drop.

Item	Weight [lbs]	CG position [ft]
1. Sensors	59.5	2.62
2. Battery	28.7	3.28
3. Subsystems	222	5.9
4. Fuselage	920.3	11.01
5. Fuel	4,233.3	14.03
6. Wing	213.2	14.7
7. Payload	330.7	14.76
8. Installed thermal engine	535.3	24.26
9. Tail	116.9	26.13
10. Nose landing gear	64.3	4.26
11. Main landing gear	210.3	16.04
The Drop empty	2,370.4	14.53
12. The Drop at MTOW	6,934.4	14.23

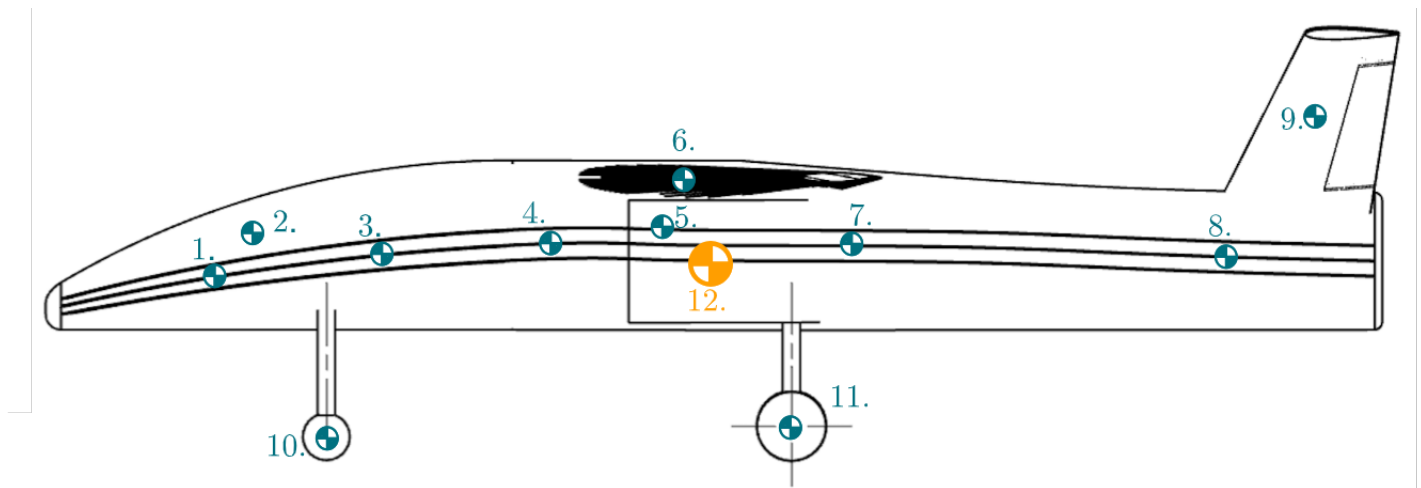


Figure 5.16: CG distribution of The Drop.

## 6 Stability

### 6.1 Static stability

#### 6.1.1 Characteristic points

In order to verify the static stability of The Drop, some characteristic points must be determined, such as the center of gravity which will vary according to different flight configurations, the aerodynamic center and the neutral point.

#### 6.1.2 Center of gravity

The longitudinal position (along the  $x$ -axis) of the center of gravity from the nose,  $x_{CG}$ , is determined with the ratio of the total moment over the total weight of the aircraft, which is the method from Sadraey's book [18]. The total moment is computed as the sum of each element contribution using a lever arm with respect to the nose, which is set as the origin.

Considering the aircraft fully loaded, so that the weight is equal to the maximum take off weight denoted MTOW, the position of the center of gravity from the nose is 14.2 ft. The centers of gravity of each component are displayed in Table 5.8 and in Figure 5.16. The overall position of the center of gravity is also computed for different configurations. The results are resumed in Table 6.1.

#### 6.1.3 Aerodynamic center

The position of the aerodynamic center expressed as a percentage of the mean aerodynamic chord MAC is determined with the Mach number, the sweep angle and the aspect ratio. Using the graphs from L. Noels course Conceptual Design [14], it is approximated to 27% of the MAC. Based on Section 5.1.1, the MAC of the wing is equal to 3.65 ft so, the position of the aerodynamic center from the nose along the  $x$ -axis is at 14.22 ft.

#### 6.1.4 Neutral point

The neutral point can be determined using the following relation :

$$h_n = h_0 + \frac{dC_{LT}}{dC_{L_w}} V_T - \frac{dC_{m_{fus}}}{dC_{L_w}},$$

where  $h_n$  and  $h_0$  are the position of the neutral point and the position of the aerodynamic center in percentage of the MAC. The second term of the right hand side of the equation is the tail contribution to the position of the neutral point and the third term is the effect of the fuselage. Using the equations from Reference [14], they are respectively given by :

$$\frac{dC_{L_T}}{dC_{L_w}} V_T = V_T \frac{C_{L_{T\alpha}}}{C_{L_{W\alpha}}} \left( 1 - \left( \frac{d\epsilon}{d\alpha} \right) \right) \quad \text{and} \quad \frac{dC_{m_{fus}}}{dC_{L_w}} = \frac{k_{fus} w_{fus}^2 l_{fus}}{S_W c_{w,MAC} C_{L_{W\alpha}}}.$$

Regarding the contribution of the tail,  $V_T$  is the tail volume ratio,  $C_{L_{T\alpha}}$  is the slope of the tail lift coefficient,  $C_{L_{W\alpha}}$  is the slope of the wing lift coefficient and  $\frac{d\epsilon}{d\alpha}$  is the derivative of the downwash angle,  $\epsilon$ , with respect to the angle of attack. The derivative  $\frac{d\epsilon}{d\alpha}$  is estimated at 0.5 using the estimations provided by Raymer [9].

Regarding the fuselage contribution,  $k_{fus}$  is a fuselage parameter evaluated to be equal to 0.608 using approximations given in Reference [14],  $w_{fus}$  is the width of the fuselage,  $l_{fus}$  is the length of the fuselage,  $S_W$  is the surface of the wing and  $c_{w,MAC}$  is the MAC of the wing.

The position of the neutral point along the  $x$ -axis in percentage of the MAC is 0.42. The distance from the nose of the aircraft is thus 14.76 ft.

### 6.1.5 Longitudinal stability

The longitudinal stability of the aircraft is governed by the static margin. It corresponds to the stability of the aircraft in the direction of the pitching motion, around the  $y$ -axis. As stated in G. Dimitriadis course Stability and Control [33], to ensure that the aircraft is statically stable, the static margin given by Eq. 6.1.5 must be positive.

$$K_n = -\frac{dC_m}{dC_{L_W}} = h_n - h > 0,$$

with  $C_m$  the total moment coefficient,  $C_{L_W}$  the lift coefficient of the wing,  $h_n$  the position of the neutral point and  $h$  the center of gravity in percentage of the MAC. The center of gravity must be ahead of the neutral point. Certification authorities state that  $K_n \geq 0.05$  [33]. To ensure enough longitudinal stability for a good control of the aircraft, the static margin must thus be in the range  $0.05 \leq K_n \leq 0.20$ .

The static margin is computed for limit configurations. First, the stability is verified for the fully loaded aircraft with the weight equal to the maximum take-off weight and for the empty aircraft with the minimum weight. Then, it is verified for the most forward position of the center of gravity considering all the fuel in the aircraft but no payload, and the most backward center of gravity considering all the payload in the aircraft but no fuel.

The results are listed in Table 6.1.

Table 6.1: Stability margin for different configurations.

	Weight of the aircraft [lbs]	$x_{CG}$ [ft]	Static margin [-]
Only fuel	6,605	14.20	0.15
MTOW	6,934	14.24	0.14
Empty aircraft	2,370	14.53	0.07
Only payload	2,701	14.56	0.06

The CG range is illustrated in Figure 6.1. The axis on the scheme represents the horizontal distance from the nose of the fuselage. The center of gravity range, noted as CG range, is characterized by its most forward and its most backward position. Its distance from the neutral point, referenced as NP, gives the static margin. It is highlighted that the center of gravity range is well within it. In order to have a better visualization, the aerodynamic center ahead of the center of gravity is also displayed.

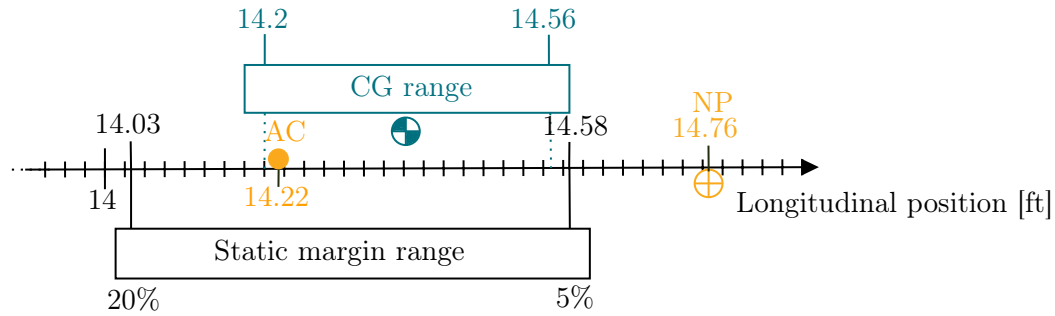


Figure 6.1: CG range along the fuselage.

The longitudinal static stability is also characterized by the rate of change of pitching moment coefficient with respect to angle of attack  $C_{m_\alpha}$ . According to Sadraey [18], a common value for this derivative ranges between  $-0.3$  and  $-1.5 \text{ rad}^{-1}$ . As displayed in Table A.1 in Appendix A, its value is equal to  $-0.9194 \text{ rad}^{-1}$ , which corresponds to a typical magnitude. This value is computed using the USAF DATCOM [34] resumed in G. Dimitriadis course Flight Dynamics and Control [35].

### 6.1.6 Lateral stability

The lateral stability is governed by the roll motion. The roll corresponds to the motion around the  $x$ -axis. The condition for a stable aircraft in roll, as stated in Sadraey's book [18], is given by :

$$\frac{dC_l}{d\beta} < 0, \quad (6.1)$$

where  $C_l$  is the rolling moment coefficient and  $\beta$  is the sideslip angle.

This derivative is computed using USAF DATCOM [34] taking into account the contributions of the wing and the body  $\frac{dC_{l_{WB}}}{d\beta}$ , and the contribution of the tail  $\frac{dC_{l_T}}{d\beta}$ . The values of these contributions are:

$$\frac{dC_l}{d\beta}_{WB} = -0.114 \text{ rad}^{-1}, \quad \frac{dC_l}{d\beta}_T = -0.017 \text{ rad}^{-1}.$$

As these two values are negative, both contributions are stabilizing and ensure a good lateral stability.

The final value of the derivative of the rolling moment coefficient with respect to the sideslip angle  $\frac{dC_l}{d\beta}$  is equal to  $-0.131 \text{ rad}^{-1}$  and verifies Eq. (6.1).

The high mounted wing is also a favorable parameter to the stability in roll motion. In order to increase the manoeuvrability, the lateral stability could be decreased by adding an anhedral angle (negative dihedral angle) to the wing. The vertical position of the center of gravity of the aircraft, which is about 5.32 ft, is relatively close with respect to the vertical position of the wing, which is about 5.67 ft. Taking this into consideration and since the mission of The Drop is to deliver some packages and identify victims with a minimum of accuracy, a small anhedral angle of about 1 to 3 degrees could have been used without impacting the overall performances. However, since The Drop does not have to make very precise maneuvers or acrobatic figures, an anhedral angle is not necessary and the design can remain the same.

### 6.1.7 Directional stability

Directional stability corresponds to the stability in the direction of the yaw motion. The stability condition for the yaw motion, as stated in Sadraey's book [18], is :

$$\frac{dC_n}{d\beta} > 0,$$

where  $C_n$  is the yaw coefficient.

The yaw motion corresponds to the motion around the  $y$ -axis. The aircraft must be stabilizing in yaw

which means that after a sideslip perturbation, the aircraft must return in its original direction and position. Even if, in this case, the derivative must be positive, this requirement corresponds to a stabilizing condition. The derivative of the yaw coefficient with respect to the yaw angle is the sum of the high-mounted wing/body effect  $\frac{dC_n}{d\beta}_{WB}$  and the tail contribution  $\frac{dC_n}{d\beta}_T$ . These two contributions, computed using USAF DATCOM [34], are equal to:

$$\frac{dC_n}{d\beta}_{WB} = -0.172 \text{ rad}^{-1}, \quad \frac{dC_n}{d\beta}_T = 0.472 \text{ rad}^{-1}.$$

The wing/body contribution is a bit destabilizing and the tail must be sufficiently stabilizing to counterbalance this effect. The total derivative  $\frac{dC_n}{d\beta}$  is equal to  $0.299 \text{ rad}^{-1}$ . So the condition is verified and the aircraft is stable in the direction of yaw motion.

## 6.2 Dynamic stability

The dynamic stability of the airplane was computed using the USAF DATCOM [34] methodology. This methodology is empirical which means that the results should be used carefully and a real analysis in a wind tunnel would be preferable. The first step is to compute the aerodynamic derivatives, which are listed in Table A.1 in Appendix A. For all calculations, the V-tail horizontal and vertical surfaces are represented separately and independently as for a conventional tail. This is advised in NASA report 823 [17] since complex interference effects are too hard to model at this stage and would necessitate experimental studies.

The longitudinal dynamic stability is characterized by the rate of change of pitching moment coefficient with respect to pitch rate  $C_{m_q}$ . This derivative is equal to  $-16.920 \text{ rad}^{-1}$ . According to Sadraey's book [18], this derivative has a typical value that ranges between  $-5$  and  $-40 \text{ rad}^{-1}$ . It therefore corresponds to an acceptable value.

The lateral dynamic stability is characterized by the rate of change of yawing moment coefficient with respect to the yaw rate  $C_{n_r}$ . Sadraey [18] recommends a range for this derivative between  $-0.1$  and  $-1 \text{ rad}^{-1}$ . It is computed to  $-0.456 \text{ rad}^{-1}$  which is in the required range.

The equations governing the control of the airplane are in state-space :

$$\dot{\mathbf{x}}(t) = \mathbf{A}\mathbf{x}(t) + \mathbf{B}\mathbf{u}(t),$$

where  $\mathbf{x}(t)$  is the vector containing the system state *i.e.*  $\mathbf{x} = [u \ v \ w \ p \ q \ r \ \phi \ \theta \ \psi]^T$  and  $\mathbf{u}(t)$  is the vector containing the control surface state *i.e.*  $\mathbf{u} = [\xi \ \eta \ \zeta \ \tau]^T$ . The matrix  $\mathbf{A}$  is computed using the methodology explained in Reference [33] for both longitudinal and lateral stability. Knowing these matrices, the dynamic



stability of the aircraft can be characterized with their eigenvalues. Indeed, as explained in Reference [33] and Reference [36], the aircraft is dynamically stable if all the eigenvalues of the matrices have a negative real part. The eigenvalues values are given in Table 6.2. These values are consistent with the intervals given in Reference [18].

Table 6.2: Eigenvalues of  $\mathbf{A}$  in longitudinal and vibration lateral modes of The Drop.

Longitudinal	Lateral
-2.2641 + 1.0694i	-3.1306 + 0.0000i
-2.2641 - 1.0694i	-0.3546 + 3.6386i
-0.0071 + 0.0349i	-0.3546 - 3.6386i
-0.0071 - 0.0349i	-0.0148 + 0.0000i
	-0.0000 + 0.0000i

As all the longitudinal eigenvalues have a negative real part and at least one of the lateral eigenvalues has a zero real part, the aircraft is dynamically stable longitudinally, and neutrally dynamically stable laterally.

### 6.2.1 Longitudinal modes

The parameters of the longitudinal modes are determined from the eigenvalues of the longitudinal matrix  $\mathbf{A}$ . The two sets of eigenvalues correspond to the two longitudinal modes.

The first set with a higher magnitude corresponds to the short period oscillation mode and the second set to the phugoid. The characteristics of the two modes, the natural frequency and the damping ratio, are resumed in Table 6.3. The natural frequency is given by the magnitude of the eigenvalue and the damping ratio is given by the opposite of the real part of the eigenvalue over the natural frequency.

Table 6.3: Longitudinal modes of The Drop.

	$\omega$ [rad/s]	$\zeta$ [-]
Short period oscillation	2.5039	0.9042
Phugoid	0.0356	0.1994

According to Sadraey’s book [18], some requirements about damping ratios must be respected. Considering the phugoid mode and a level 1 of acceptability, the damping ratio must be above 0.04 for an

acceptable level of comfort for the pilot. Since there is no pilot in The Drop, this level of accessibility may not be necessary. Nevertheless, level 1 also allows to avoid degradation in mission effectiveness and is then preferable. This condition is met for this configuration.

For the short period oscillation, the damping ratio must be between 0.3 and 2 considering a flight phase category B, which corresponds to phases in cruise, in loiter, in climb or in descent. This requirement is also met.

## 6.2.2 Lateral modes

The different lateral modes can be computed from the eigenvalues of the lateral matrix  $\mathbf{A}$ . The two conjugated eigenvalues correspond to dutch roll. The most negative one corresponds to roll subsidence and the one with the lower amplitude corresponds to spiral mode. The parameters of the lateral modes are listed in Table 6.4.

Table 6.4: Lateral modes of The Drop.

	$\omega$ [rad/s]	$\eta$ [-]	Time constant $\tau$ [s]
Roll subsidence	-	-	1.02
Spiral mode	-	-	63.71
Dutch roll	3.69	0.099	-

Sadraey [18] presents the required values of the lateral modes for multiple kinds of aircraft, flight phases and levels of acceptability. The Drop is considered as an aircraft of class I (mass below 13,228 lbs). Flight phases B and C are more relevant in the studied case since they include cruise, climb, loiter, descent, take-off and landing. Moreover, the higher the level of acceptability the better the aircraft reacts to disturbance, the level 1 is therefore desired as often as possible. Firstly, for roll mode, the time constant is lower than 1.4 s which verifies levels of acceptability for all phases. For spiral mode, the time constant is greater than 20 s, which provides best level of acceptability for all phases. Finally, dutch roll mode damping factor and frequency of oscillation satisfy levels of acceptability, as the damping ratio is greater than 0.08 s and the frequency is greater than 1 rad/s.

## 7 Aerodynamics

The aerodynamic properties of The Drop were first evaluated using empirical correlations during the conceptual stage design. In this section, a numerical study is carried out in order to confirm or update results obtained with the empirical approach. The numerical study is performed using DARTFLO<sup>1</sup> software, developed by A.Crovato [37]. DARTFLO is an open-source software which solves transonic potential flow equations. During this analysis, the focus is on the lift and drag produced by the wing. This model allows to verify that the designed wing behaves as expected in terms of lift and drag generation.

In addition, a drag study is carried out based on the component build-up method with the equations described in Torenbeek [16]. This drag study allows estimating the drag during cruise, take-off and landing configurations. Finally, the lift distribution obtained using DARTFLO is used to model the wing in finite element analysis.

### 7.1 Lift analysis

#### 7.1.1 Wing model

The aerodynamic of the wing must be verified as the wing is the largest lifting surface of The Drop and thus the largest source of induced drag. Therefore, optimizing the lift to drag ratio is a major concern in the design. In order to ensure the validity of the results, a convergence study over different parameters is conducted. First, a convergence analysis over the lift and drag coefficients is done in order to find the appropriate domain size which leads to independent results. Then, a convergence study is done on the mesh size as well as on the growth ratio by analysing the convergence of the lift and drag coefficient.

Figure 7.1 highlights the evolution of the lift coefficient curve as a function of the angle of attack in cruise condition. The results enable to reassess the slope of the 3D lift coefficient obtained using empirical correlations.

It can be observed that the results obtained empirically and numerically are close to each other. This is directly reflected by the slope values of the wing lift coefficient listed in Table 7.1. The wing is thus designed with accurate estimations. In addition, DARTFLO correctly estimates the lift produced by the wing.

Furthermore, Table 7.1 shows that the lift to drag ratio computed empirically is significantly higher than the

---

<sup>1</sup>gitlab: <https://gitlab.uliege.be/am-dept/dartflo>

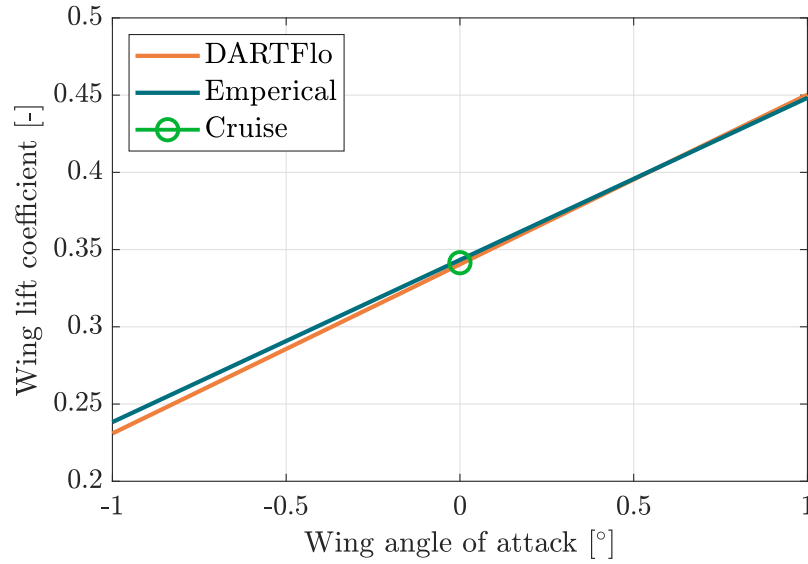


Figure 7.1: Wing lift coefficient with respect to the angle of attack.

one estimated using DARTFLO. In fact, DARTFLO does not take any viscosity into account into its drag computation. Thus, it is underestimated which leads to aberrant lift to drag ratios that cannot be considered correct. The empirical value is then used rather than the numerical one.

Table 7.1: Wing lift characteristics of The Drop.

	Empirical	Numerical
Lift coefficient slope [ $rad^{-1}$ ]	6.02	6.29
Lift to drag ratio [-]	33	54.73

It is also interesting to investigate the evolution of the moment coefficient of the wing with respect to its angle of attack. The evolution of the moment coefficient is considered at the predicted aerodynamic center of the wing. Its evolution is highlighted in Figure 7.2. The values of the slope of the moment coefficient and the main characteristics of the aerodynamic center are listed in Table 7.2. As the value of the slope of the moment coefficient with respect to the wing angle of attack is small, it is not necessary to investigate a new position of the aerodynamic center using CFD computations. Therefore, the aerodynamic center characteristics computed during the preliminary design phase of the aircraft are still considered as valid.

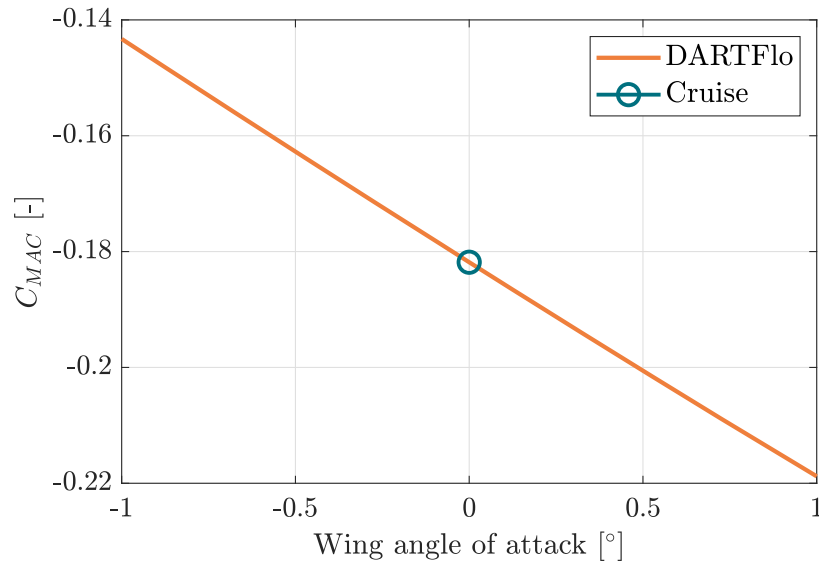


Figure 7.2: Moment coefficient at the aerodynamic center with respect to the angle of attack.

Table 7.2: Aerodynamic center characteristics of the wing.

The Drop	
$C_{MAC}$ [-]	-0.18
$x_{AC}$ [ft]	0.95
$y_{AC}$ [ft]	4.77
MAC [ft]	3.64
Slope [ $\text{rad}^{-1}$ ]	2.18

The span-wise lift distribution of The Drop is highlighted in Figure 7.3. The lift distribution is compared to the elliptical lift distribution in order to determine how far the lift distribution obtained with DARTFLO is from the optimal lift distribution. The elliptical lift distribution is computed using the lifting line theory. Since the wing is not elliptical, the lift distribution cannot be elliptical. However, it can be seen that the lift profile is close to the elliptical one. The wing thus generates almost optimal lift as designed in Section 5.1.1. Moreover, the lift profile computed using DARTFLO is thus validated. It can therefore be used in the design of the structure of the wing.

Figure 7.4 highlights the fact that no shocks occur along the mean aerodynamic chord.

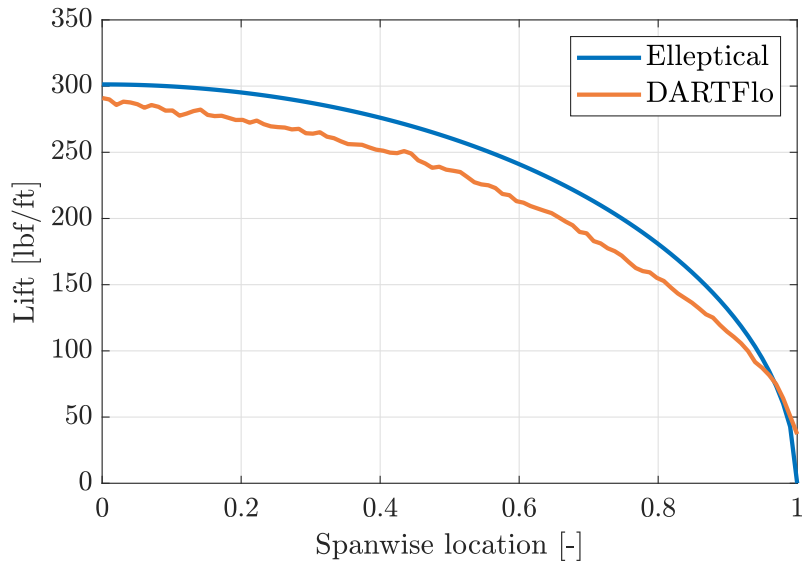


Figure 7.3: Moment coefficient at the aerodynamic center with respect to the angle of attack.

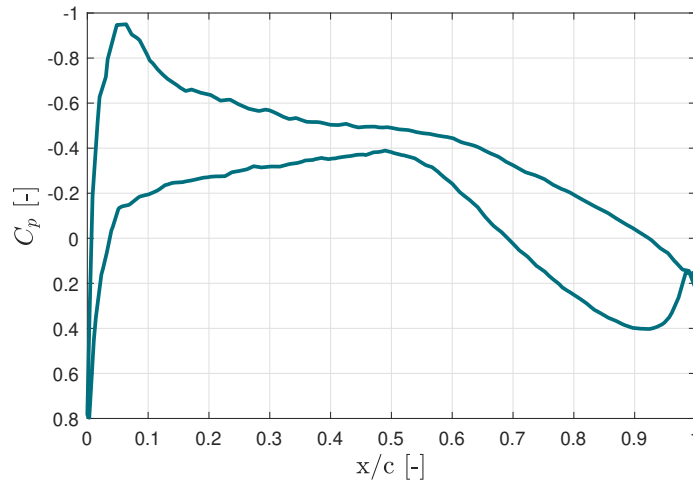


Figure 7.4: Evolution of the pressure coefficient along the mean aerodynamic chord.

## 7.2 Drag analysis

### 7.2.1 Drag in cruise configuration

A study of the drag applied to The Drop is first conducted in the cruise configuration, with the aircraft flying at Mach 0.7. The drag can be divided into the following contributions: vortex-induced drag, profile drag, interference effects and drag due to protuberances. Note that the aircraft is not subjected to wave drag as there are no shock waves, as shown by the lift analysis. Each contribution has its specific origin, as summarized in Figure 7.5. The study of the drag is led following Torenbeek's Appendix F [16].

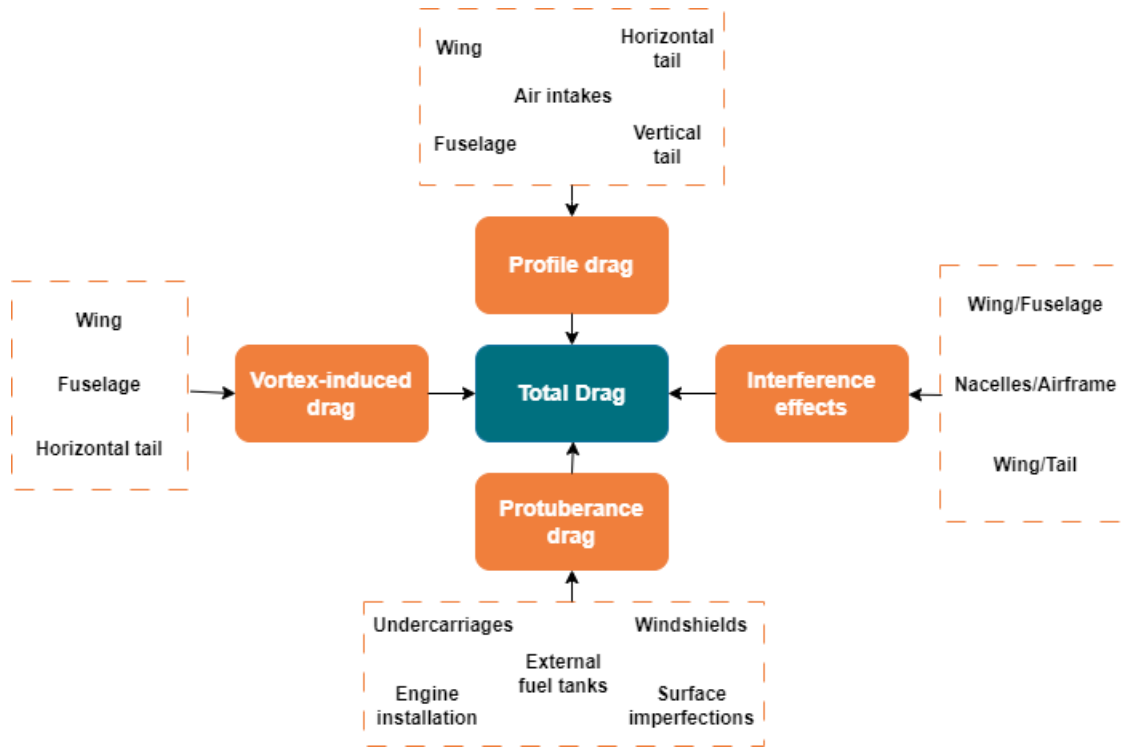


Figure 7.5: Drag breakdown

As mentioned in Section 5.1.4, the drag coefficient in cruise configuration can be expressed as:

$$C_D = C_{D_0} + \frac{C_L^2}{e\pi AR} = C_{D_0} + C_{D_i}. \quad (7.1)$$

In Eq. 7.1, the term  $C_{D_0}$  corresponds to the zero-lift drag which is a combination of the profile, interference and protuberance drag. The term  $C_{D_i}$  corresponds to the drag induced by lift. Both of these terms are first estimated in Section 5.1.4. Their values are compared to the analytical results obtained in this section.

### Vortex-induced drag

This form of drag is related to the pressure drag associated to the presence of trailing vortices and downwash and therefore to lift. The fuselage is not taken into account as it does not produce any lift at this stage of the design. The wing and tail are here considered as isolated bodies and their contribution to the vortex-induced drag can be computed separately. Regarding the wing, its contribution is first computed using approximated results of the lifting line theory. A correction accounting for its twist is then added. Only the horizontal part of the V-tail generates this type of drag and its contribution can be obtained in a similar manner as for the wing. The vortex-induced drag coefficients of the wing and the horizontal tail in cruise condition are given in Table 7.3.

Table 7.3: Vortex-induced drag, in cruise configuration.

	Wing	Horizontal tail
$C_D$ [-]	0.0054	0.003

### Profile drag

This type of drag is caused by the skin friction and the pressure drag due to the boundary layer. The contribution of each main part of the aircraft is computed using the flat plate analogy. A shape correction factor  $\varphi$  is then defined to account for three effects:

- the boundary layer around a body develops differently than around a flat plate;
- the thickness of the body being non zero, the velocity of the flow outside of the boundary layer is higher than the free stream velocity. The skin friction is therefore increased;
- the frontal area of the body undergoes noticeable pressure drag.

The profile drag of each main part of the aircraft can be computed as:

$$C_{DS} = C_F(1 + \varphi)S_{wet}.$$

$S_{wet}$  corresponds to the wet surface of the considered component of the aircraft while  $C_F$  corresponds to the friction coefficient.

To this estimation of the profile drag is added a correction. For the wing, the latter accounts for the increment in drag at the stalling angle of attack while for the fuselage, it takes into consideration its axisymmetric shape and the incidence and elevator deflection for the horizontal tail.

Finally, the profile drag generated by the air intakes has to be considered. The latter can be computed by summing the drag caused by the surface of the duct in contact with the flow and the pressure loss inside the intake, which leads to a decrease in thrust and thus, an increment in drag. The profile drag coefficients of the wing, the fuselage, the air intakes and the V-tail are given in Table 7.4.

Table 7.4: Profile drag of each main part, in cruise configuration.

	Wing	Fuselage	Air intakes	V-tail
$C_D$ [-]	0.0048	0.0086	0.0015	0.0036



### Subcritical interference effects and corrections

Until now, the contribution to drag of each main part of the aircraft was computed as if they were isolated bodies. The interactions between these parts are now taken into account. The interference between the wing and the fuselage is considered with a first correction that is done regarding the vortex-induced drag. The latter adds a term accounting for the lift transferred by the wing to the fuselage when it is at zero angle of attack. Then, the viscous interference occurring at the junction between the wing and the fuselage due to the thickening of the boundary layer is taken into account. Finally, the interference between the wing and the tail is considered. This correction accounts for the effect on the tail of the downwash behind the wing.

### Protuberance drag

In this case, only the surface imperfections are relevant in the protuberance drag. Those account for a certain percentage of the profile drag related to the wing, the fuselage and the tail.

### Total drag

The total drag can be computed according to the drag breakdown previously developed. All of the contributions are related to the gross wing area  $S$  as:

$$C_{D_j} = \frac{(C_D S)_j}{S}. \quad (7.2)$$

Eq. 7.2 defines the drag areas, which enable to express the drag as a function of the aircraft lift coefficient  $C_L$ .

The total drag coefficient is finally obtained with:

$$C_D = \frac{\sum (C_D S)_j}{S} = A + BC_L + DC_L^2.$$

The values of the drag coefficients are summarized in Table 7.5.

Table 7.5: Drag coefficients, in cruise configuration.

	Vortex induced drag ( $C_{D_i}$ [-])	Zero lift drag ( $C_{D_0}$ [-])	Total ( $C_D$ [-])
Drag study results	0.0084	0.0202	0.0286

From the total drag coefficient given in Table 7.5, the total drag of the aircraft in cruise is computed and is equal to 496 lbf. This value is close to the first estimation computed in Section 5.1.4, which thus validates the design. As mentioned in Section 5.3, the maximum thrust generated by the engine in cruise is 803 lbf.

This means that The Drop flies at 62% of the thrust available by the engine in cruise. The value of the drag applied on The Drop in cruise condition can thus be easily compensated by the thrust generated by the engine FJ44-3AP.

### Comparison with DARTFLO

In DARTFLO, only pressure drag is computed (contribution of wave drag and induced drag) as it solves inviscid flows. As a result, the estimation of the drag made in DARTFLO does not represent the reality since it does not take into account any effect of viscosity.

It is interesting to compare results obtained with DARTFLO with the ones computed analytically. The analytical study is indeed based on empirical correlations which take into account viscous effects. The difference between the two methods is represented in Figure 7.6. As the wing is oversized in cruise condition, the wave drag is null. Therefore, the wing does not produce any wave drag. Even though the wave drag is minimized in

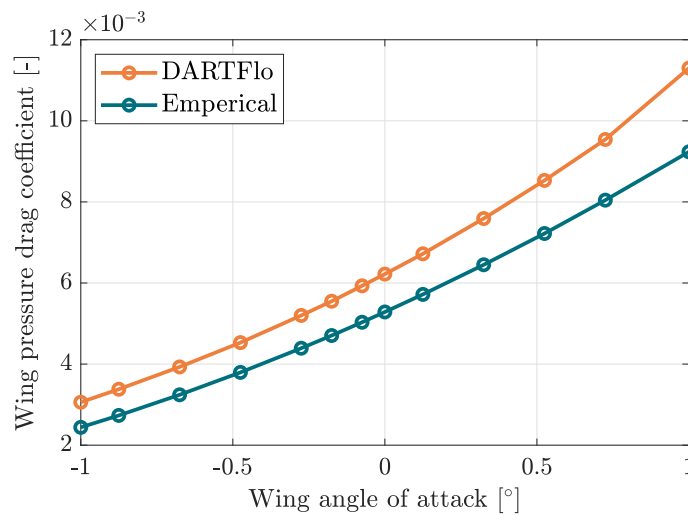


Figure 7.6: Pressure drag coefficient with respect to the angle of attack. Comparison between numerical method and empirical correlations in cruise condition.

cruise condition using DARTFLO, it is still overestimated. Therefore it is preferable to trust results obtained with the drag study.

### 7.2.2 Drag in take-off and landing configurations

The drag analysis of The Drop can now be conducted in take-off and landing configurations. The drag is studied following Torenbeek's Appendix G [16], which is adapted for an aircraft flying at a low speed. In these

configurations, some drag increments have to be added to the drag estimated by Eq. 7.1:

$$C_D = C_{D_0} + \frac{C_L^2}{\pi A R e} + \Delta_f C_{D_p} + \Delta C_{D_v} + \Delta_{trim} C_D. \quad (7.3)$$

In Eq. 7.3,  $\Delta_f C_{D_p}$ ,  $\Delta C_{D_v}$  and  $\Delta_{trim} C_D$  correspond respectively to the increment in induced drag, profile drag and trim drag coefficients. Note that the second term in Eq. 7.3 has to be evaluated with the lift coefficient during landing or take-off. Moreover, the value of  $C_{D_0}$  that is used is the one obtained using the drag analysis in cruise but adapted to the take-off and landing conditions. Finally, the drag generated by the landing gears, which are now out of the fuselage, should be added to the protuberance drag compared to the cruise configuration.

The drag coefficients in cruise, take-off and landing are summarized in Table 7.6. The contribution of each type of drag to the total one, for each flight configuration, is also displayed in Figure 7.7.

Table 7.6: Drag coefficients for different flight configurations.

	$C_L$ [-]	$C_D$ [-]
Cruise	0.425	0.0286
Take-off	1.62	0.1966
Landing	1.84	0.3196

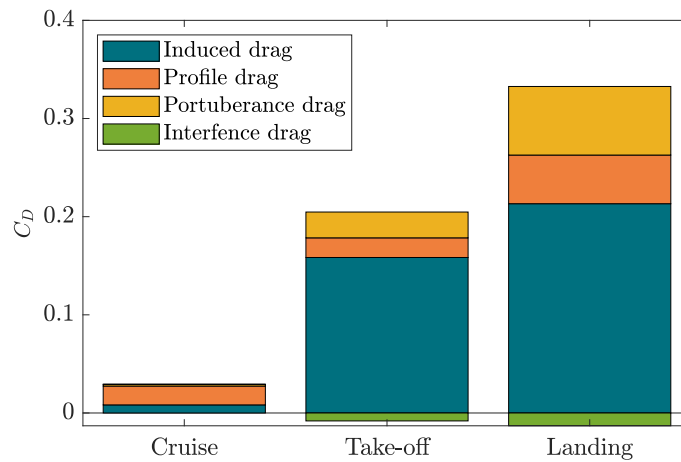


Figure 7.7: Drag breakdown for different flight configurations.

Two main observations can be made. First, the induced drag greatly increases for the take-off and landing configurations. It also becomes the most significant contribution to total drag compared to the cruise configuration. This is due to the large increase in lift occurring because of the flaps deflection. Then, the interference drag becomes a non-negligible contribution to the total drag in high lift configurations as opposed to the cruise one. The latter is indeed mainly due to trim drag, which accounts for the effect of the horizontal tail and thus to its interference with the wing. This drag is negative, meaning that it contributes to a reduction of the total drag. The possibility of such a result is confirmed by Torenbeek in Section F-4.4 [16].

### 7.2.3 Lift to drag ratio

In this section, the lift and drag of The Drop were studied and quantified. From these results, the lift to drag ratio of the aircraft can be determined in the three considered configurations: cruise, take-off and landing. Regarding the cruise configuration, this ratio is evaluated using the lift obtained with DARTFLO and the drag obtained with the drag analysis in cruise. Since the lift is not studied in take-off and landing configurations with DARTFLO, the lift to drag ratio is evaluated using the lift coefficients computed in Section 5.1.2, in the flaps design. The lift to drag ratios of the entire aircraft, for the three configurations, are given in Table 7.7.

Table 7.7: Lift to drag ratios of The Drop for different flight configurations.

	Cruise	Take-off	Landing
$L/D$ [-]	14.99	8.24	5.75

### 7.2.4 Drag polar

The drag polar is constructed using the relation presented in Section 5.1.4 for different angles of attack. By plotting the tangent to the curve from the origin of the polar, the optimal design point is determined. This is highlighted in Figure 7.8.

The optimal design point from the graph corresponds to a lift coefficient of 0.667. The lift coefficient of The Drop is equal to 0.425. The optimal point is the point with minimal drag conditions for a given lift and angle of attack. The difference between the design point and the optimal point can be explained by a priority given to other parameters such as the stability and the cruise speed instead of a minimum drag. This graph being plotted later in the design conception, other parameters were already prioritized and a change in the design point could impact the fuel consumption or the stability which are very important for the mission as much as

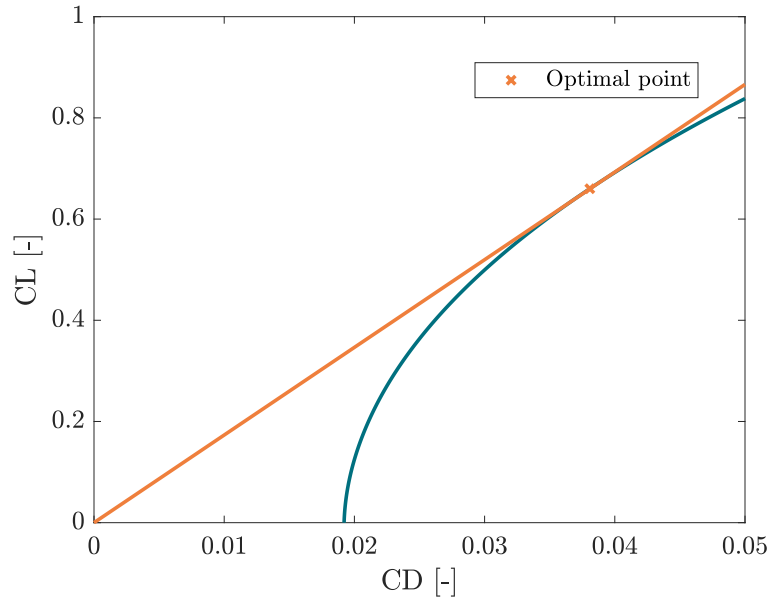


Figure 7.8: Drag polar.

cruise speed. Thus, in order to reach the optimal design point, some changes in the design of the wing or the propulsion system may be needed. A trade-off study about which parameters could improve the performances to reach the optimal design point is made in Section 11.

## 8 Structure

### 8.1 Materials selection

The choice of materials directly influences the performances of the aircraft as well as the operating costs. The materials used in the manufacturing of the aircraft thus face three main challenges:

- **Mass reduction:** As for every aeronautical structure, the main objective is to reduce the mass. In fact, the higher the mass, the higher the fuel consumption and the lower the performances of the aircraft.
- **Cost reduction:** In the design of the aircraft, the cost reduction is not a key parameter. However, regarding the hazards of The Drops mission, the costs should nevertheless be taken into account. It is indeed mentioned in the AIAA proposal [4] that there is a risk of losing the aircraft during the mission. Therefore, its costs should be low in order to minimize the importance of the lost.
- **Environmental impact:** The third challenge aims to reduce the emissions of pollutants during the manufacture of the various materials used in The Drop as well as studying the possibilities of recycling.

The Drop will suffer different loads during its lifetime. Therefore, chosen materials must have a high yield strength and a high tensile strength. The selected materials must indeed remain within their elastic operating range in order to avoid the propagation of cracks already potentially present in the structure. As the aircraft is supposed to live for a long time, the materials must have good fatigue resistance and high fracture toughness. Finally, the aircraft is exposed to the ambient air and to the weather. Therefore, chosen materials must be oxidation and corrosion resistant.

### 8.1.1 Landing gears

The landing gears must sustain the shock at landing but also the weight of the aircraft during ground operations. Thus, the chosen material must display a high buckling resistance, a high fracture toughness, a high fatigue resistance and a high bending resistance. Additionally, in order to reduce the manufacturing and flight costs, both the mass and the costs of the material need to be minimized.

First, the Ashby diagrams are drawn for each constraints using the *CES* [38] software. A set of materials can then be retained. In order to determine the most efficient among them, a weight-factor method is applied for both objectives: the minimization of the mass and of the costs. The material which stands out is *low alloy steel*. Therefore, it is the material that is chosen for the landing gears. The selection was refined to AISI 4340 as it has good strength performances and low price. Its main properties are given in Table 8.1.

Table 8.1: AISI 4340 low alloy steel properties [38].

Property	Value
Density	0.1 lbs/in <sup>3</sup>
0.01 % proof stress	33,600 psi
Shear strength	21,030 psi
Price	0.86 \$/lbs

### 8.1.2 Skin, stringers, flaps and frames

Due to the mission of The Drop, the aircraft might be submitted to intense efforts during flight. A high toughness is thus required. Additionally, the three main challenges mentioned previously must be taken into account in order to maximize The Drop performances. An analysis performed on CES [38] software is performed taking into consideration the following indices: strength to weight ratio (structural), price to weight (costs),

carbon footprint and embodied energy (ecological impact). The retained material is Aluminum 7075 alloy. This seems a fair choice since aluminum alloys are commonly used in the aeronautic industry. The European leader in the manufacturing of flaps, *Sonaca* [39], indeed suggests the use of aluminum alloys for the flaps. The mechanical properties of Aluminum 7075 alloy are highlighted in Table 8.2.

Table 8.2: Mechanical properties of the Aluminium 7075 alloy [38].

Property	Value
Density	0.102 lbs/in <sup>3</sup>
Tensile strength	83,000 psi
Elastic modulus	10,400,000 psi
Yield strength	73,000 psi
Shear strength	48,000 psi

## 8.2 Characteristic diagrams

### 8.2.1 Placard diagram

The placard diagram is represented in Figure 8.1. It corresponds to the evolution of the true airspeed with respect to the altitude. The design cruise velocity  $V_c$ , or dash speed, is the velocity of the aircraft at maximum thrust. It is computed as:

$$V_c = \sqrt{\frac{T_{max}}{0.5 \cdot \rho \cdot S_W \cdot C_D}} = 497.91 \text{ kts}, \quad (8.1)$$

where  $C_D$  depends on  $V_c$  itself. The cruise speed is thus computed with an iterative process. It is important to note that the compressibility effects must be taken into account since the associated Mach number, equal to 0.84, is greater than the divergence Mach of the airfoil, which is equal to 0.78 as stated in Section 5.1.2. The drag indeed drastically increases above that speed. Lastly, it can be noted that this computation is in accordance with the dash speed  $M = 0.8$  considered in the wing design. That additional drag contribution is taken into account accordingly to Reference [40].

The dive velocity  $V_d$ , which is the maximum velocity, is computed according to FAR regulations [19]. At cruise altitude, it is evaluated to 532.77 kts. Above the cruise altitude, the aircraft flies at constant Mach while

under this altitude, the equivalent velocity is kept constant. The equivalent velocity is expressed as:

$$V_e = \sqrt{\frac{\rho}{\rho_0}} V_c = 304.91 \text{ kts},$$

where  $\rho$  is the air density at cruise altitude and  $\rho_0$  is the air density at sea level.

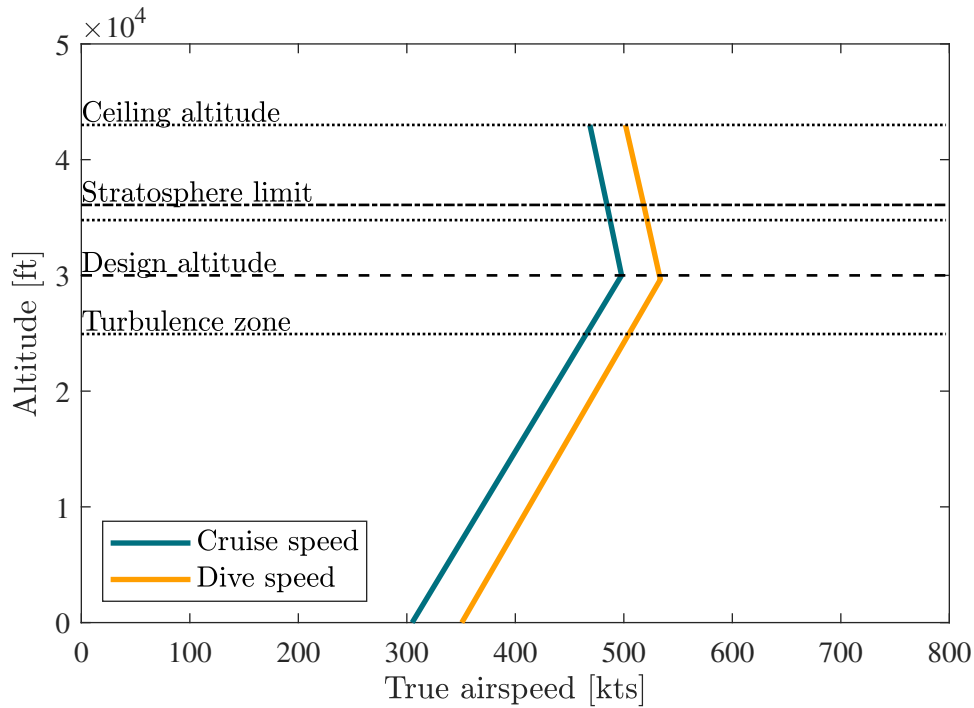


Figure 8.1: Placard diagram.

### 8.2.2 Maneuver envelope

The flight envelope describes the relation between the load factor experienced by the aircraft and its equivalent airspeed at cruise altitude. The load factors meeting the requirements from Table 2.1 are developed here after. Thus, the minimum and the maximum load factor that the airplane should experience during its flight are denoted respectively by  $n_{min}$  and  $n_{max}$  and have a value of -1.5 and 3. No deformation is expected below these factors. The ultimate load factor,  $n_{limit}$ , corresponds to  $1.5 \cdot n_{max} = 4.5$  and is the design load factor of the structure.

The limits of the envelope and their associated velocities are obtained using the method of Federal Aviation Regulation [19] in the case of light airplanes.



The maneuver envelope is represented in orange in Figure 8.2 and is computed as:

$$n = \frac{L}{W} = \frac{\rho_0 V_e^2 S_W C_{Lmax}}{2W},$$

with  $\rho_0$  the air density at sea level,  $S_W$  the wing area and  $W$  the weight of the aircraft.

The characteristic speeds obtained with the maneuver envelope are listed in Table 8.3. The equivalent stall velocity in cruise in flaps up configuration is  $V_{s1}$ ,  $V_a$  is the maximum equivalent airspeed representing the maximum authorized deflection of the controls,  $V_b$  is the minimum speed to enter a gust region.  $V_c$  and  $V_d$  were previously detailed in Section 8.2.1.

The gust envelope is represented in dotted blue lines in Figure 8.2. It highlights the impact of the gusts on the maneuverability of the plane. The associated load factor is computed as:

$$n_g = 1 + \frac{FC_{L\alpha plane} U_e V_e S_W}{498W},$$

with  $F$  the gust alleviation factor,  $U_e$  the equivalent gust velocity of 36 ft/s for  $V_a$  and for  $V_b$ , and of 18 ft/s for  $V_d$ . The gust alleviation factor  $F$  and the airplane weight ratio  $\mu$  are defined as:

$$F = \frac{0.88\mu}{5.3 + \mu} \quad \mu = \frac{2W}{\rho C_{L\alpha plane} c g S_W},$$

where  $c$  is the mean aerodynamic chord of the wing.

In order to ensure that The Drop resists to the loads during flight, the worst cases are considered. They correspond to the points listed in Table 8.4 and highlighted in the envelope of Figure 8.2.

Table 8.3: Characteristic speeds of The Drop.

Speed	Value [kts]
$V_{s1}$	127
$V_a$	221
$V_b$	165
$V_c$	305
$V_d$	351

Table 8.4: Critical points for The Drop.

Points	$n$ [-]	V [kts]
A	3	221
B	4.5	305
C	3	351
D	-1.5	351
E	-1.5	305

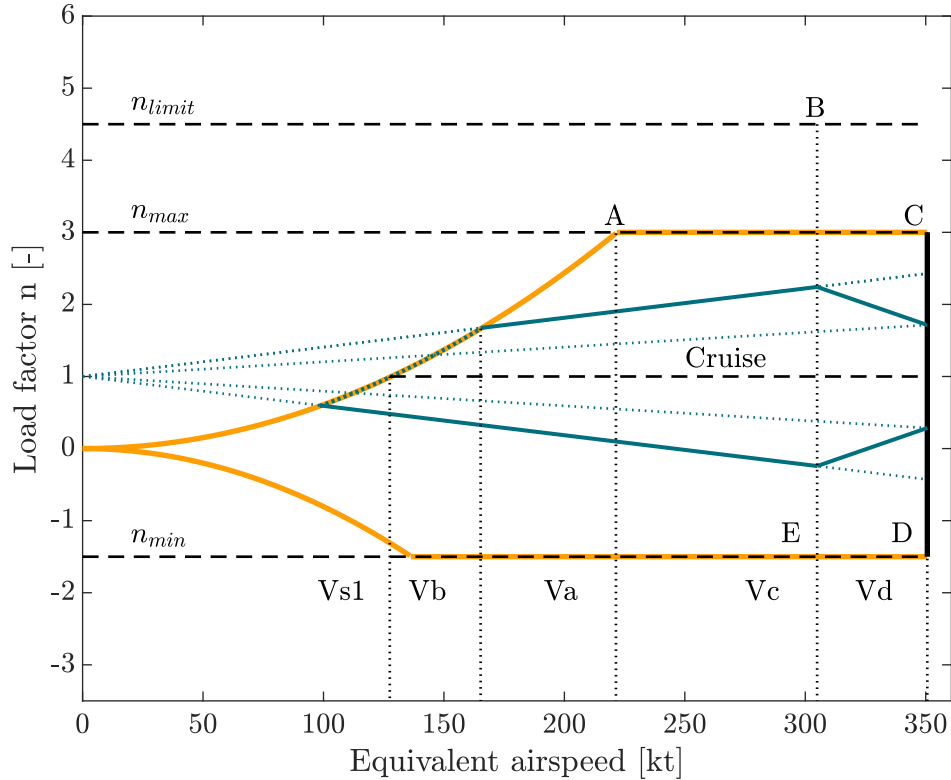


Figure 8.2: Maneuver envelope (in orange), gust envelope (in blue) and gust loads (dotted blue lines) at 30,000 ft.

## 8.3 Loads computation

For each point of the maneuver envelope listed in Table 8.4, the structural loads are computed at the fuselage and at the wing. Beforehand, the aerodynamic loads are determined at the wing and at the empennage. Those results are then used in Section 8.4 to determine the structural design of the fuselage and of the wing.

### 8.3.1 Aerodynamic loads

In Figure 8.3 are displayed the loads acting on The Drop. The loads are computed for each point of the maneuver envelope following the FAR 23.441 regulations [19]. The Drop corresponds to aircraft category (a). For the maximum yaw angle, requirement (3) is considered. Its value is thus  $\phi = 15$  deg. Concerning the maximum pitch acceleration, the FAR 23.423 regulation is not followed, the commonly used value  $\ddot{\theta} = 60$  deg/s<sup>2</sup> is rather used.

Performing a vertical and momentum equilibrium on the aircraft leads to the system of Eq. (8.2).

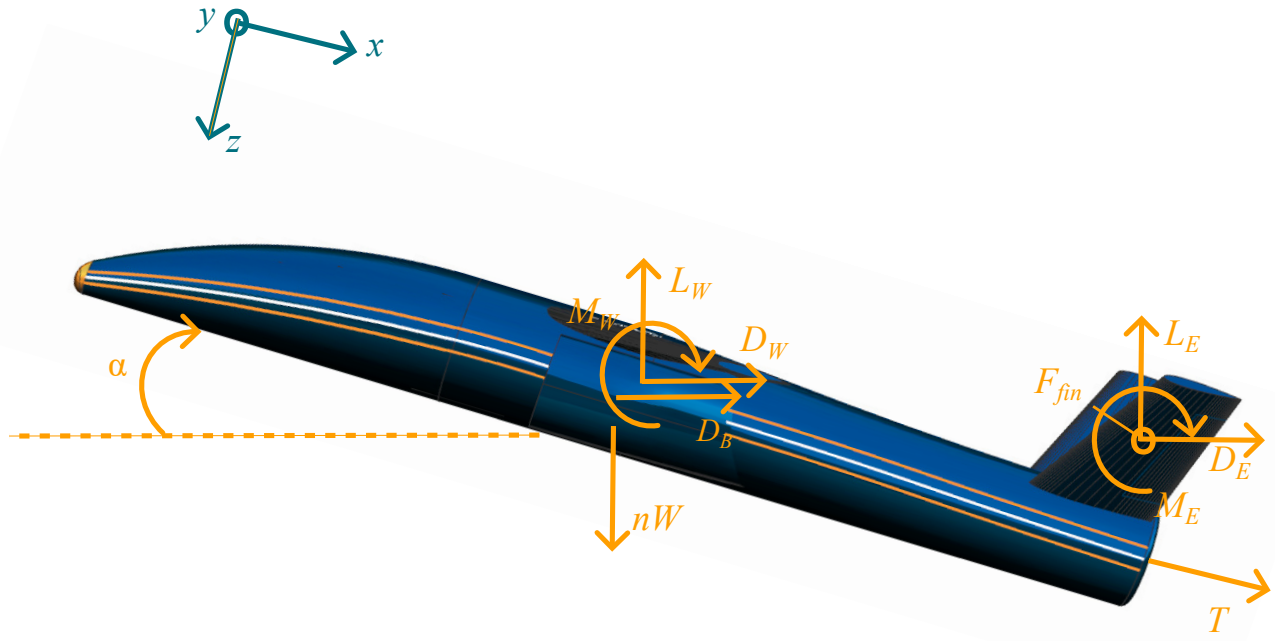


Figure 8.3: Aerodynamics loads applied to The Drop during flight.

$$\begin{cases} L_W + L_E = n \cdot W - T \sin(\alpha); \\ l_W \cdot L_W - l_E \cdot L_E = I_\theta \cdot \ddot{\theta} - M_E - M_W - l_{DB} \cdot D_B + l_E \cdot D_E - l_W \cdot D_W + l_T \cdot T, \end{cases} \quad (8.2)$$

where  $l_i$  is the lever arm with respect to the center of gravity of the aircraft,  $L_i$  is the lift,  $D_i$  is the drag,  $M_i$  is the momentum all associated to component  $i$ ,  $D_{DB}$  is the body drag,  $T$  is the thrust and  $I_\theta$  is the moment of inertia of the fully loaded aircraft around its center of mass computed with *NX-Siemens* software [41].

For each point of the maneuver envelope, the angle of attack is such that the lift counterbalances the weight of the aircraft. The results are listed in Table 8.5.

Table 8.5: Aerodynamic loads at each point of the maneuver envelope.

Points	$n$ [-]	$V$ [kts]	AoA [ $^\circ$ ]	$L_W$ [lbf]	$L_E$ [lbf]	$M_{fus}$ [lbf · ft]	$M_{tail}$ [lbf · ft]	$F_{fin}$ [lbf]
A	3	221	35.3	14,155	7,785	11,664	5	1,002
B	4.5	305	27.2	21,431	11,726	22,161	10	1,903
C	3	351	13.5	14,659	7,496	29,320	14	2,518
D	-1.5	351	-7.7	-6,934	-4,107	29,320	14	2,518
E	-1.5	305	-10.4	-6,551	-4,462	22,161	10	1,903

### 8.3.2 Structural loads at the fuselage

Considering the section right after the end of the wing, the structural loads at the fuselage can be computed. The equilibrium is computed with the system Eq. (8.3) where  $W_i$ ,  $x_{cg,i}$  and  $w_{ac,i}$  are respectively the weight, the distance between the fuselage section and the center of gravity, and the distance between the fuselage section and the aerodynamic center of component  $i$ . The angle between the wing and the fuselage is noted  $\alpha_W$ . The structural loads of the rear of the fuselage for each point of the maneuver envelope are listed in Table 8.6.

$$\left\{ \begin{array}{l} T_x = (-n(W_{fuselage} + W_{tail} + W_{engine} + W_{air-intakes}) + L_E) \sin(\alpha - \alpha_W); \\ T_y = -F_{fin}; \\ T_z = (n(W_{fuselage} + W_{tail} + W_{engine} + W_{air-intakes}) - L_E) \cos(\alpha - \alpha_W), \\ M_x = -M_{fus}; \\ M_y = (n(W_{tail} \cdot x_{cg,tail} + W_{fuselage} \cdot x_{cg,fuselage} + W_{engine} \cdot x_{cg,engine} + W_{air-intakes} \cdot x_{cg,air-intakes}) \\ \quad - L_E \cdot x_{ac,empennage}) \cos(\alpha - \alpha_W); \\ M_z = F_{fin} \cdot x_{ac,fin}. \end{array} \right. \quad (8.3)$$

Table 8.6: Structural loads computed at the fuselage section right after the wing for each point of the maneuver envelope.

Points	$T_x$ [lbf]	$T_y$ [lbf]	$T_z$ [lbf]	$M_x$ [lbf·ft]	$M_y$ [lbf·ft]	$M_z$ [lbf·ft]
A	2,169	-1,002	-3,251	-11,664	-50,733	12,449
B	2,555	-1,903	-5,330	-22,161	-83,039	23,652
C	747	-2,518	-3,541	-29,320	-56,159	31,292
D	350	-2,518	2,140	-29,320	32,728	31,292
E	524	-1,903	2,468	-22,161	36,749	23,652

### 8.3.3 Structural loads at the wing

The structural loads at the wing can be computed considering the equilibrium of the forces at the wing root. Since the lift, the drag, the momentum, the weight of the wing and the fuel weight are the only forces acting

on the wing, the structural loads can be expressed as in the system Eq. (8.4).

$$\left\{ \begin{array}{l} T_x = \frac{L_W}{2} \sin(\alpha) + \frac{D_W}{2} \cos(\alpha); \\ T_y = 0; \\ T_z = \frac{L_W}{2} \cos(\alpha) + \frac{D_W}{2} \sin(\alpha) - n \frac{W_W + W_{W, fuel}}{2} \cos(\alpha); \\ M_x = - \left( \frac{L_W}{2} \cos(\alpha) + \frac{D_W}{2} \sin(\alpha) \right) \cdot y_{acW} - n \frac{W_W + W_{W, fuel}}{2} \cos(\alpha) \cdot y_{cgW}; \\ M_y = \frac{L_W}{2} \frac{MAC}{4} + \frac{M_W}{2} + n \frac{W_W + W_{W, fuel}}{2} \frac{MAC_W}{2}; \\ M_z = \left( -\frac{D_W}{2} \cos(\alpha) + \frac{L_W}{2} \sin(\alpha) \right) \cdot y_{acW} - n \frac{W_W + W_{W, fuel}}{2} \sin(\alpha) \cdot y_{cgW}. \end{array} \right. \quad (8.4)$$

Since the wing is symmetric, only its half is considered. Therefore, all the loads acting on the wing have a contribution divided by two. The structural loads at the wing root for each point of the maneuver envelope are listed in Table 8.7.

Table 8.7: Structural loads computed at the wing root for each point of the maneuver envelope.

Points	$T_x$ [lbf]	$T_y$ [lbf]	$T_z$ [lbf]	$M_x$ [lbf·ft]	$M_y$ [lbf·ft]	$M_z$ [lbf·ft]
A	-2,191	0	6,016	-44,691	-2,870	9,095
B	-2,200	0	9,112	-68,981	-4,438	8,544
C	-263	0	6,159	-47,562	-3,148	173
D	6	0	-2,829	22,494	-171	-409
E	-878	0	-2,504	20,612	1,122	4,436

## 8.4 Structural design

Using the structural loads computed in the previous subsection, the stringers, frames and skin panels of the fuselage and of the wing can be designed. The design is here based on a 2D analytical analysis. Thus, for the fuselage, the section right after the wing is considered. The fuselage cross section is assumed to be a single cell structure made of stringers and skin panels. Regarding the wing, the section at the root is considered. As it is the common configuration, the cross section is assumed to be a triple cell structure made of stringers, spars and skin panels.

Numerous assumptions are made in this study. First, the stringers are represented by booms that sustain

solely direct stresses while the skin panels only carry shear stress. Then, in order to keep Saint-Venant principle valid, a low section variation is considered. Moreover, by neglecting the clamping effect, there is no additional stress caused by warping. The coupling between shearing and bending is neglected as well. The pure bending theory can thus be used to estimate the direct stress. Additionally, the plastic domain is not entered during the loading. Finally, in order to ensure safety, according to the requirements listed in Table 2.1, a safety factor  $s = 1.5$  is considered such that the maximum tensile and shear strength are reduced with respect to the tensile stress  $\sigma_r$  and shear strength  $\tau_r$  listed in Section 8.1:

$$\begin{cases} \sigma_{xx,max} = \frac{\sigma_r}{s} = 48,635 \text{ psi;} \\ \tau_{max} = \frac{\tau_r}{s} = 32,005 \text{ psi.} \end{cases}$$

Then, in order to assess the results, the fuselage and the wing are modeled and studied through finite element analysis using the *NX-Siemens* software with the *Samcef* solver [41]. A *2D mapped mesh* is used on the structure, i.e. the skin, the spars and the ribs. For the stringers and the frames, a *1D mesh* is applied. Additionally, both the wing root and the section of the fuselage right after the wing are assumed to be clamped. The displacement field, the principal stresses and the shear stresses of the structure are then computed. These results ensure that the structure resists to the drag, the lift, the weight of the components inside the structure and the weight of the structure itself.

### 8.4.1 Fuselage

In order to design the structure of the fuselage, 24 stringers are placed around the fuselage surface. The number of stringers is chosen such that the distance between the stringers is equal to 6.4 in, which is included in the recommended range 3.9-7.8 [42]. The stringers are placed such that the distance between each of them is constant. This distribution is preferable to a distribution associated with a constant angle between the stringers since considering a constant angle leads to a variable distance between each stringer. Flexion of the structure could then be induced between the largely spaced stringers. In order to avoid this situation, the stringers are equidistant as represented in Figure 8.4.

As mention previously, the direct stress is assumed to only be carried by the stringers. It is expressed as:

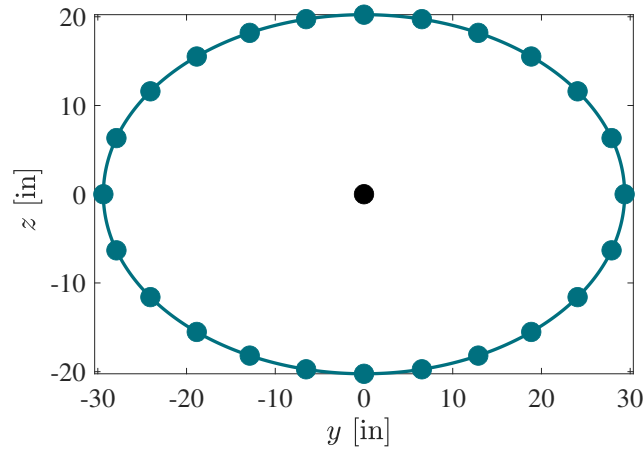


Figure 8.4: Structure of the cross-section right after the wing.

$$\sigma_{xx,i} = \frac{(I_{zz,i} \cdot M_{y,i} + I_{yz,i} \cdot M_{z,i})z_i - (I_{yz,i} \cdot M_{y,i} + I_{yy,i} \cdot M_{z,i})y_i}{I_{yy,i} \cdot I_{zz,i} - I_{yz,i}^2} + \frac{T_{x,i}}{\sum_i B_i},$$

where  $I$  is the second moment of inertia and  $(y_i, z_i)$  are the coordinates of the  $i^{th}$  stringer with respect to the centroid, represented in black in Figure 8.4. Since the stringer area is assumed to be constant over the cross section, the minimum stringer area is computed for each point of the maneuver envelope as:

$$B_{min} = \max \left| \frac{B\sigma_{xx,i}}{\sigma_{xx,max}} \right|. \quad (8.5)$$

The minimum stringer area for the fuselage is  $0.082 \text{ in}^2$ .

In order to compute the minimum thickness of the skin, the shear flux in the structure must be computed. It is expressed in Eq. (8.6).

$$q(s) = -\frac{I_{zz}T_z^{web} - I_{yz}T_y^{web}}{I_{yy}I_{zz} - I_{yz}^2} \left[ \sum_{i:s_i \leq s} z_i B_i \right] - \frac{I_{yy}T_y^{web} - I_{yz}T_z^{web}}{I_{yy}I_{zz} - I_{yz}^2} \left[ \sum_{i:s_i \leq s} y_i B_i \right] + \sum_j q^j(0), \quad (8.6)$$

where

$$\begin{cases} T_y^{web} &= T_y - \sum_i \mathbf{P}_x^i \frac{\delta y^i}{\delta x}; \\ T_z^{web} &= T_z - \sum_i \mathbf{P}_x^i \frac{\delta z^i}{\delta x}, \end{cases}$$

and  $q^j(0)$  is the closed-cell correction term of the  $j^{th}$  cell deduced from the moment equilibrium.

The minimum thickness of the skin can then be found computing Eq. (8.7) and is equal to  $0.0064 \text{ in}$ . However, since the fuselage will be exposed to extreme meteorological conditions, the skin thickness is set to

0.02 in. This will also facilitate the assembly of The Drop, in particular rivets placement [43].

$$t_{min} = max \left| \frac{q(s)}{\tau_{max}} \right|. \tag{8.7}$$

The dimensions of the structure are summarized in Table 8.8. Based on these results, the rear of the fuselage can be modeled. Its internal structure is represented in Figure 8.5. The frames are equally spaced of 28 in.

Table 8.8: Structural elements characteristics of the rear of the fuselage.

Fuselage elements	Area [in <sup>2</sup> ]/Thickness [in]	Quantity
Stringers	0.085	24
Frames	0.18	7
Skin	0.02	-

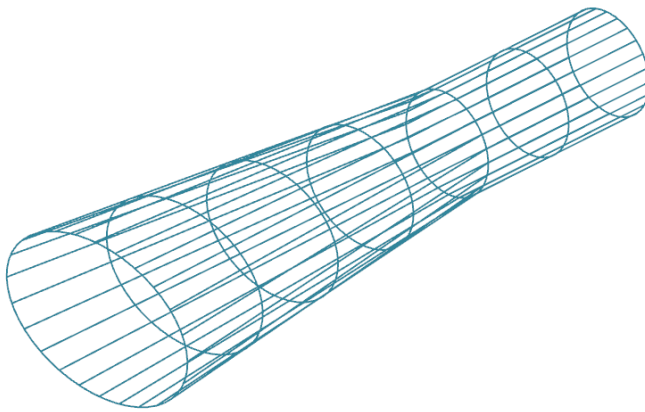


Figure 8.5: Structure of the rear of the fuselage.

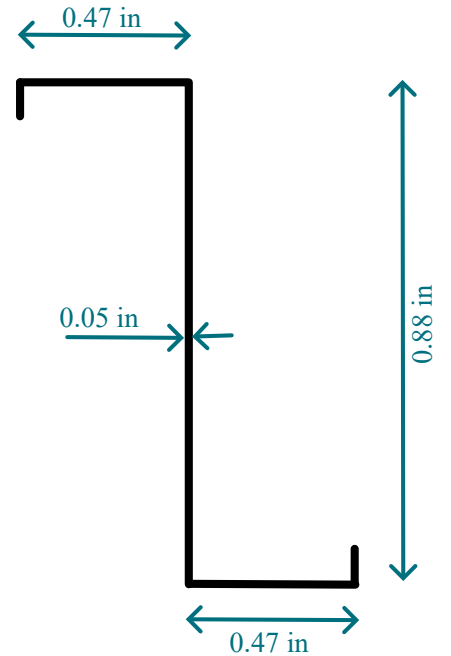


Figure 8.6: Geometry of the fuselage stringers.

In order to properly model the fuselage, the loads must be taken into account. First of all, the fuselage is subjected to its own weight, considering the load factor of the critical case. Then, the frames are submitted to the payload loads. Thus, the weight of the air-intakes and the engine listed in Table 5.8 are applied on the



corresponding fuselage section. The air-intakes inside the rear of the fuselage have the same skin thickness than the fuselage. Therefore, in order to properly estimate its mass, the skin thickness must be known. A first guess of 110 lbs is thus first assumed. After computing the fuselage skin thickness, its mass is estimated to 123 lbs. The generated thrust must be considered as well. Finally, the load contribution of the V-tail must be taken into account. Its weight, the generated lift and the fin force listed in Table 8.5 are applied at the aerodynamic center of the V-tail. Thus, rigid links connect the aerodynamic center of the tail with the corresponding frames of the fuselage. By doing so, the loads of the V-tail are transmitted to the fuselage and the moment induced by the V-tail is correctly considered. Additionally, regarding the magnitude of the considered loads, the drag contribution is neglected.

As mentioned previously, the cross-section just after the wing is assumed to be clamped. In addition, in order to properly model the structure, a glue constraint is applied between the skin and the frames as well as between the skin and the stringers.

A *2D mapped mesh* is created on the skin. After conducting a convergence analysis, the size of the quadrilateral mesh *Q8* is set to 0.4 in. The *1D mesh* on the stringers and the frames is set to the same size. It is defined accordingly to the beam areas listed in Table 8.8.

Since the aim of this numerical study is to ensure that the fuselage structure can withstand the loads for each point of the maneuver envelope, the worst case is considered, *i.e.* point B from Table 8.4. The resulting displacement, principal stresses and shear stresses are represented in Figure 8.7, Figure 8.8 and Figure 8.9.

First, it can be mentioned that, as expected since the fuselage is clamped at the section right after the wing, the maximum displacement takes place at the end of the fuselage. Moreover, it is interesting to note that the displacement is small with respect to The Drop dimensions. It indeed corresponds to about 0.4 % of the fuselage length.

Regarding the principal stresses, it can be seen in Figure 8.8 that it is concentrated at the clamped cross-section. The same observation can be done for the shear stresses represented in Figure 8.9. On the one hand, this result can be explained by the boundary condition. Enforcing a clamped section induces stresses. On the other hand, that section is, due to the configuration, submitted to the largest loads. Additionally, it can be noticed that higher stresses are observed on the frames than on the surrounding skin. In fact, as designed, they withstand most of the load.

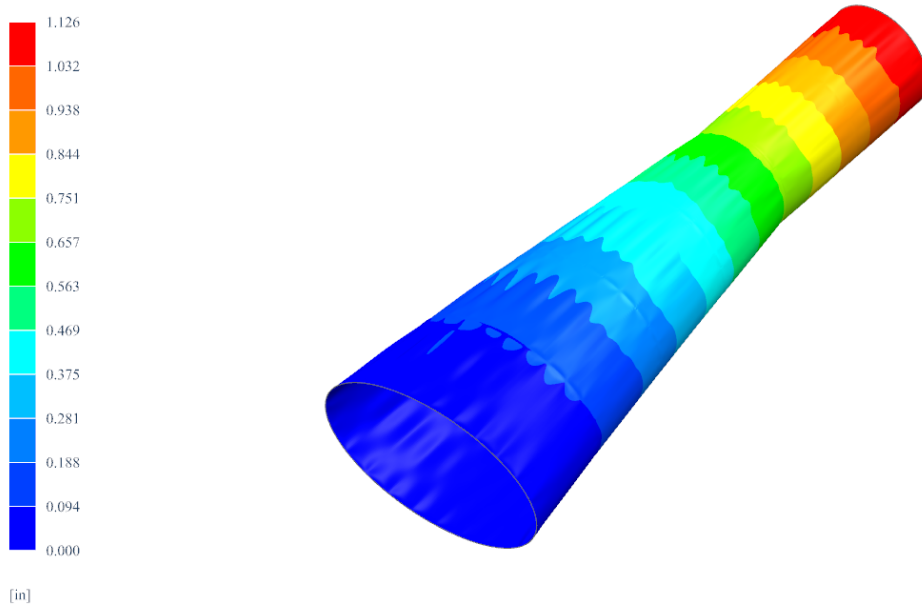


Figure 8.7: Displacement field of the rear of the fuselage of The Drop submitted to the loads of point B of the maneuver envelope 8.4.

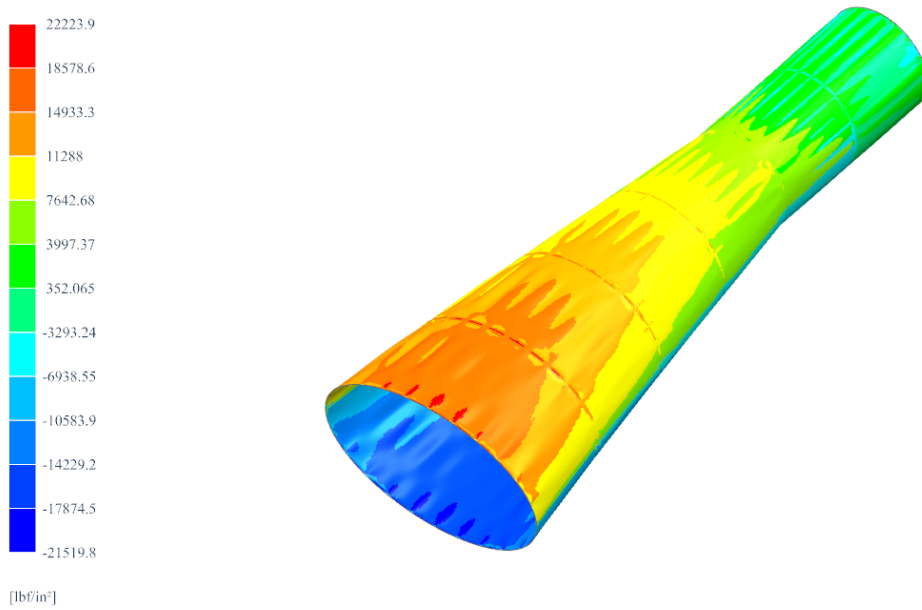


Figure 8.8: Principal stresses of the rear of the fuselage of The Drop submitted to the loads of point B of the maneuver envelope 8.4.

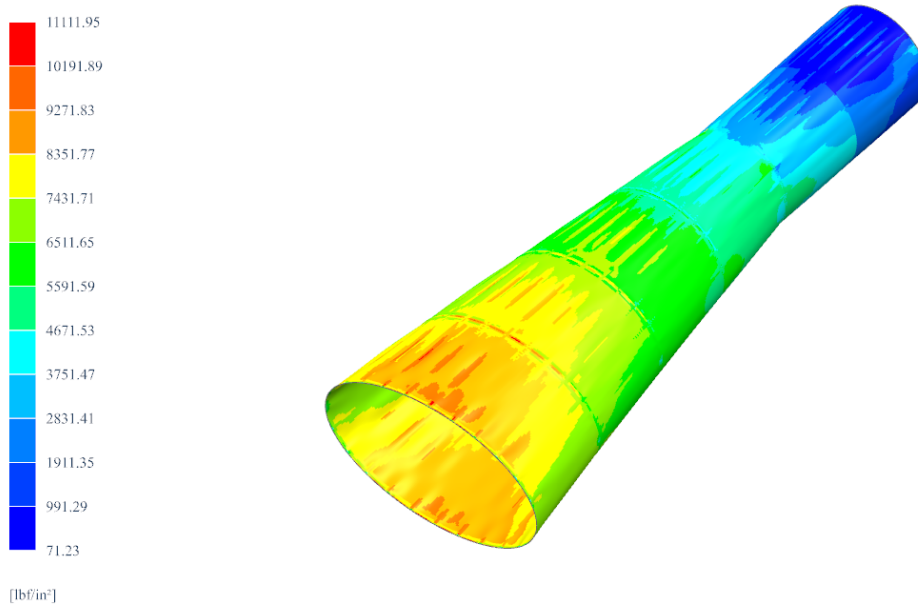


Figure 8.9: Shear stresses of the rear of the fuselage of The Drop submitted to the loads of point B of the maneuver envelope 8.4.

A final interesting point to consider is a comparison between the numerical results and the analytical results. Since the maximal principal and shear stresses are located at the cross-section right after the wing, no difference is made between the maximal stresses over the all fuselage and at the cross-section. The main results are summarized in Table 8.9. First of all, it can be noted that the analytical method overestimates the principal stresses. This method is indeed more conservative than the numerical one due to the numerous assumptions. It was assumed in the analytical study that the normal stresses are carried exclusively by the stringers while only the skin withstands the shear stresses. However, in reality, the skin, the frames and the stringers all carry the principal and shear stresses. Therefore, the analytical results overestimate the principal stresses. Moreover, the drag contribution is neglected in the numerical study. These results thus slightly underestimate the principal stresses. These two main assumptions explain the significant difference between the analytical and numerical results.

Regarding the shear stresses, the numerical results outgrow the analytical ones. This is once again a consequence of the assumptions made during the analytical study. Warping due to clamping was indeed neglected. However, the cross-section is clamped in the numerical model. The contribution of the warping to the shear stresses is thus taken into account in the numerical simulation contrary to the analytical study. Since

this contribution is small, the assumption that it is negligible is however correct. Thus, these results are close enough to validate the numerical model and ensure that the structure can resist to the loads.

In fact, the maximum stresses correspond to 27% and 57% of the yield strength respectively for the *NX-Siemens* model and analytical method while the shear stresses correspond to 23% and 22% of the shear strength of the material. These percentages are computed with respect to the maximum yield and shear strength of the material, thus not taking into account the value reduced by the safety factor  $s = 1.5$ , which explains why they are small. It must be noted that, even if the safety factor is considered, the structure resists to the loads.

Regarding the principal stresses, these ratios are in line with the structure design and with previous observations. Meanwhile, the low value of the analytical shear stresses is a consequence of two inputs. On the one hand, the skin is increased with respect to its minimal acceptable value. On the other hand, point B of the maneuver envelope corresponds to the worst case concerning the principal stresses, not the shear stresses. Regarding the low value of the shear stresses and since the skin thickness was doubled with respect to the restrictive case, no simulation is conducted considering that case.

Table 8.9: Comparison of the maximal loads computed over the cross-section right after the wing both analytically and using the *NX-Siemens* software.

Method	$\max \sigma_{xx} $ [lbf/in <sup>2</sup> ]	$\max \tau_{xx} $ [lbf/in <sup>2</sup> ]
<i>NX-Siemens</i>	22,224	11,112
Analytic	46,976	10,494

## 8.4.2 Wing

The structure of the wing is composed of 29 stringers placed along the airfoil as shown in Figure 8.10. As already mentioned, since it is the common configuration, the latter is separated into 3 cells. The first cell separation is placed at the quarter chord and the second at the begin of the control surfaces which were designed in Section 5.1.1. The stringers are distributed on the two first cells only since the third cell corresponds to the moving part of the wing, there is thus no structural reinforcement there. Furthermore, two spars ended by two flanges are placed at the cell boundaries. To simplify the structure, all the stringers and the four flanges are assumed to have the same cross section area  $B$ .

To compute the minimum stringer area  $B$  that can withstand the stresses, the same method as for the



Figure 8.10: Structure of the airfoil.

fuselage is applied. First, the direct stresses are obtained as:

$$\sigma_{yy,i} = \frac{(M_x \cdot I_{zz} + M_z \cdot I_{xz})z_i - (M_z \cdot I_{xx} + M_x \cdot I_{xz})x_i}{I_{xx} \cdot I_{zz} - I_{xz}^2},$$

with  $I$  representing the second moment of inertia and  $(x_i, z_i)$  the coordinates of the  $i^{th}$  stringer of the wing with respect to the centroid, represented with a black dot in Fig. 8.10. The direct stresses are computed for each point of the maneuver envelope. The minimum area is then obtained considering Eq. (8.5). Its minimum value is  $0.23 \text{ in}^2$ .

In order to determine the minimum skin thickness, the shear flux is first computed as:

$$q(s) = -\frac{I_{zz}T_z^{web} - I_{xz}T_x^{web}}{I_{xx}I_{zz} - I_{xz}^2} \left[ \sum_{i:s_i \leq s} z_i B \right] - \frac{I_{xx}T_x^{web} - I_{xz}T_z^{web}}{I_{xx}I_{zz} - I_{xz}^2} \left[ \sum_{i:s_i \leq s} x_i B \right] + \sum_j q^j(0),$$

where the web loading is developed as:

$$\begin{cases} T_x^{web} = T_x - \sum_i \frac{\mathbf{P}_y^i \delta x^i}{\delta y}; \\ T_z^{web} = T_z - \sum_i \frac{\mathbf{P}_y^i \delta z^i}{\delta y}. \end{cases}$$

The closed-cell correction  $q^j(0)$  is, in this case, obtained by imposing a constant twist rate on the three cells and by adding the moment equilibrium of the section to close the system of equations. Finally, the thickness is derived from Eq. (8.7). It is equal to  $0.078 \text{ in}$ . All the wing structural elements geometries are summarized in Table 8.10.

Table 8.10: Structural elements characteristics of the wing.

Wing elements	Area [in <sup>2</sup> ]/Thickness [in]	Quantity
Stringers	0.23	29
Ribs	0.078	9
Skin	0.078	-
Spars	0.078	2

Knowing the characteristics of the structural elements, the internal structure of the wing can be modeled. Since the problem is symmetric, the computations are done on half a wing, without any loss of accuracy. The entire internal structure is represented in Figure 8.11. The geometry of the stringers is detailed in Figure 8.12. In order to reinforce the structure, 9 ribs are equally spaced along the span. The first rib is located at the root and the last one at the tip.

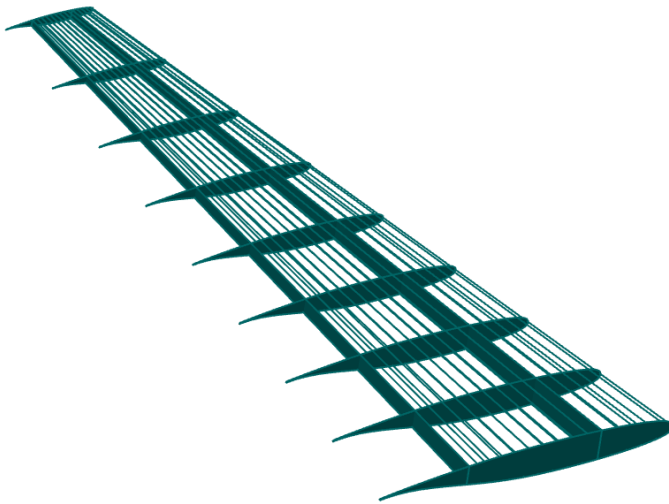


Figure 8.11: Structure of the half wing.

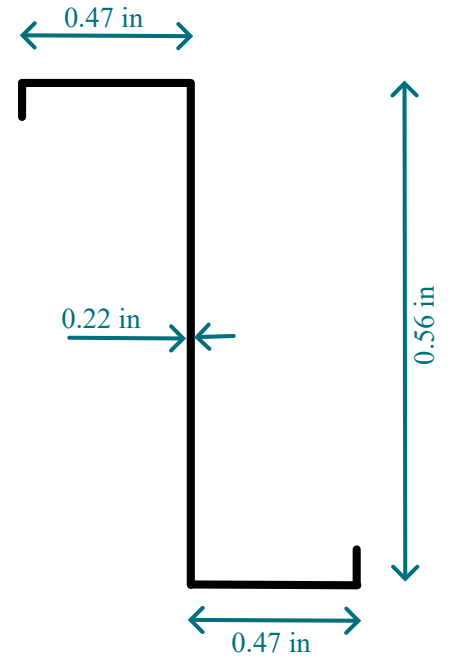


Figure 8.12: Geometry of the wing stringers.

In order to simulate the wing structure on the *NX-Siemens* software, the loads applied on the wing must be considered. The loads that must be taken into account are its own weight, comprising the internal structure and the skin, the part of the fuel included in the half wing, as well as the generated lift. The distribution of the latter along the span is obtained using DARTFLO. It is applied at the quarter chord spar. Though, it must be mentioned that the aerodynamic center of the wing moves from the quarter chord to the mid chord as the speed increases. The assumption that the resultant of the wing is applied at the quarter chord may thus induce miscalculations. Finally, assuming that the drag is small with respect to the other forces, its contribution is neglected in this model.

To ensure that the structure is strong enough to resist to the applied loads, the worst case is considered, which corresponds to point B in the Table 8.4. The load factor is thus taken into account when considering the weights. Additionally, a boundary condition is applied at the root of the wing, it is assumed to be clamped. Finally, the stringers, the frames edges and the spars edges are all glued to the skin. This constrain prevents the skin to deform independently.

A *2D mapped mesh* is created on the spars, the frames and the skin. The size of the mesh is set to 0.6 in in order to ensure convergence. On the stringers, a *1D mesh* is generated. Its size is the same as the *2D mapped mesh*.

The resulting displacement, principal stresses and shear stresses are represented respectively in Figure 8.13, Figure 8.14 and Figure 8.15. Similarly to the fuselage, the maximum displacement is observed at the tip of the wing since the root is clamped. This displacement corresponds to about 1.2% of the wing span. This ratio is reasonable considering that the wing is highly triggered since it generates most of the lift.

Regarding the principal stresses, the greatest values are located at the root of the wing as it can be seen in Figure 8.14. It is also the case for the maximum shear stresses represented in Figure 8.15. This phenomena is a direct consequence of the boundary condition. Clamping the section indeed induces important stresses. Additionally, it can be noticed that a stress concentration takes place at the quarter chord of the wing. This observation was expected since the lift is applied along that line. The reinforcement by the span is thus fully justified.

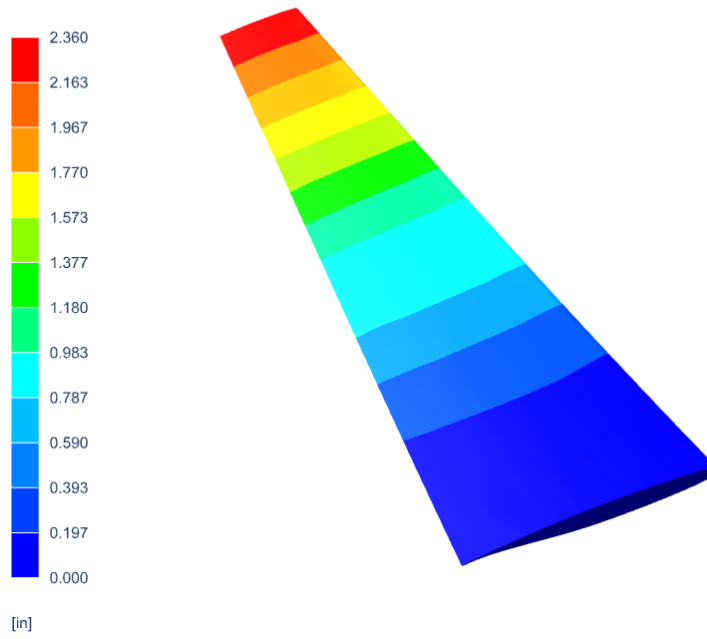


Figure 8.13: Displacement field of the half wing of The Drop submitted to the loads of point B of the maneuver envelope 8.4.

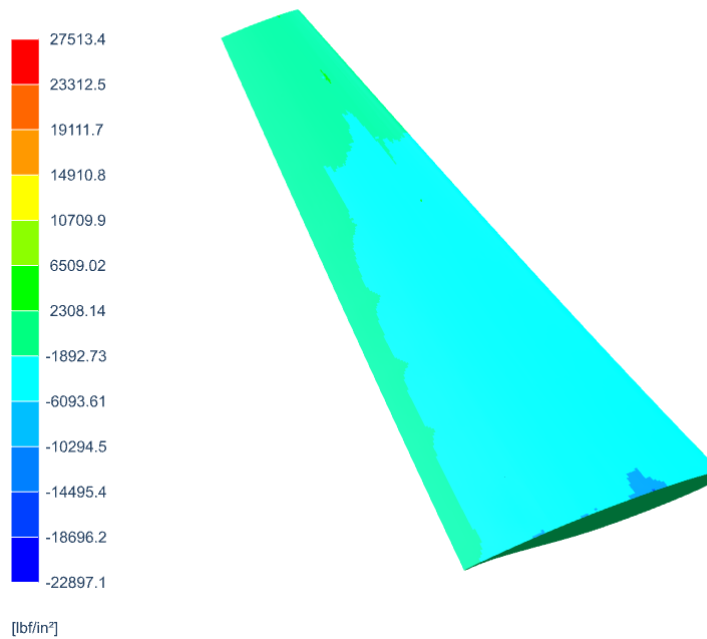


Figure 8.14: Principal stresses of the half wing of The Drop submitted to the loads of point B of the maneuver envelope 8.4.



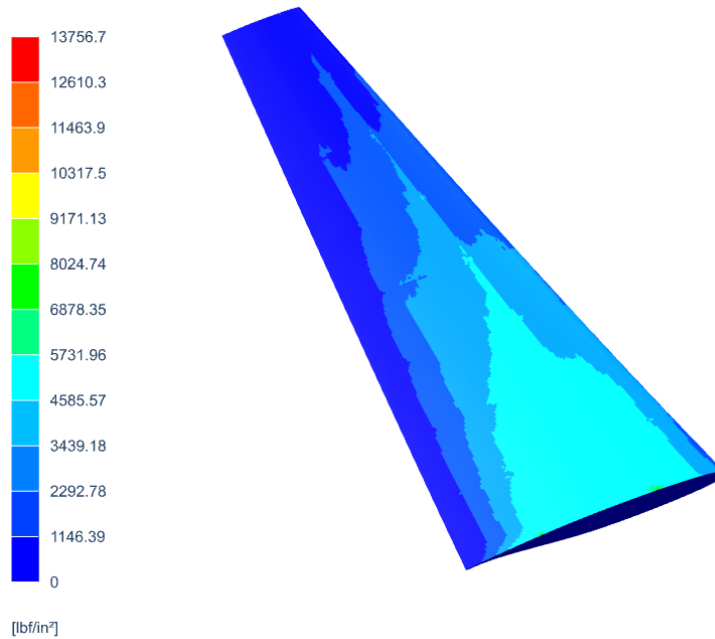


Figure 8.15: Maximum shear stresses of the half wing of The Drop submitted to the loads of point B of the maneuver envelope 8.4.

Table 8.11 gathers the stresses obtained for the half wing and compares the numerical results with the analytical ones. The analytical method overestimates both the principal stresses and the maximum shear stresses of the wing. Thus, it is more conservative than the numerical method. This difference can be explained by several reasons. First, the lift is applied at the quarter chord into the *NX-Siemens* software. Moments such as the pitching moment are thus underestimated. Then, neglecting the drag in the numerical method also tends to underestimate the stresses. Moreover, it is assumed in the analytical method that the normal stresses are only carried by the stringers and the shear stresses only by the skin. However, both stresses are in fact carried by the skin, the spars, the ribs and the stringers. The value estimated analytically is thus larger than the actual one. Regarding these explanations, the numerical results are validated.

Using the properties of the material listed in Table 8.2, it can be computed that the maximum principal and shear stresses from the *NX-Siemens* Software correspond to 33% and 29% of the yield and shear strength. For the analytical method, the principal and the shear stresses respectively account for 59% and 67% of the maximum value. In line with previous observations, the numerical results are further away from the maximum value than the analytical results. Additionally, similarly to the analysis of the fuselage, these values are compared with the maximum tensile stress and yield strength of the material before reduction by the safety

factor. Nonetheless, even if this factor is taken into account, the loads are lower than the maximum admissible value. The structure is thus able to withstand the worst case scenario given by point B of the maneuver envelope in Figure 8.4. Therefore, the wing structure can resist to the loads that are applied during the flight. Regarding the numerical results, the skin thickness and the stringers area might be reduced. A more precise numerical study should then be conducted in order to ensure that the lightened structure resist to the structural loads.

Table 8.11: Comparison of the maximal loads computed analytically and using the *NX-Siemens* software.

Method	$\max \sigma_{xx} $ [lbf/in <sup>2</sup> ]	$\max \tau_{xx} $ [lbf/in <sup>2</sup> ]
<i>NX-Siemens</i>	27,513	13,757
Analytic	48,637	32,054

## 9 Aircraft performances

The take-off, the climb, the glide, the turn and the landing are studied following Gudmundsson's methodology [10]. This analysis aims to ensure that The Drop meet the AIAA requirements at take-off and at landing [4]. Afterwards, the payload range diagram is represented.

### 9.1 Take-off

Regarding the AIAA requirements listed in Table 2.1, the aircraft must take off in less than 4,000 feet on dry, wet and icy asphalt. Also, it must pass an obstacle of 30 ft. The take-off phase is separated between the ground run ( $S_G$ ), the rotation ( $S_{ROT}$ ), the transition ( $S_{TR}$ ) and the climb ( $S_C$ ) distances as shown in Figure 9.1. Because The Drop has only one engine, there is no decision speed.

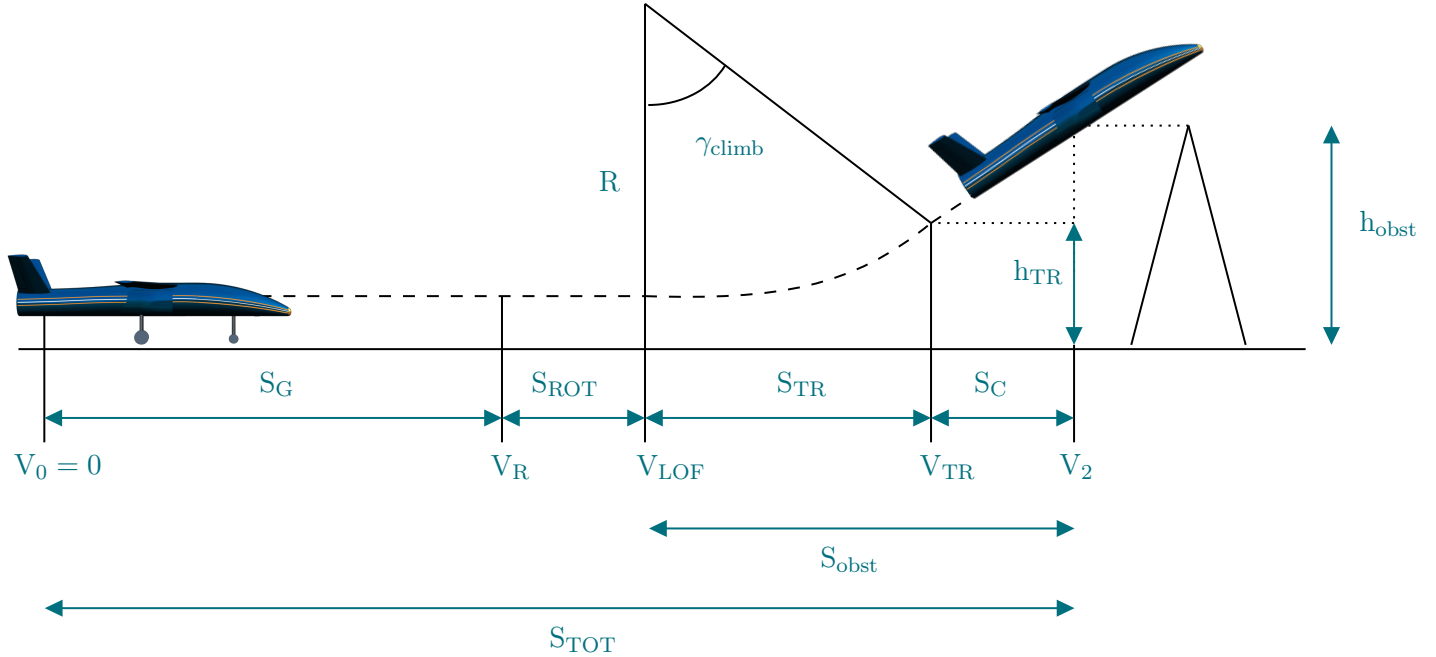


Figure 9.1: Take-off phase.

Velocities at each segment of the take-off are computed with the stall velocity at sea level conditions :

$$V_S = \sqrt{\frac{2 \cdot W_{TO}}{\rho_0 \cdot C_{L_{max,TO}} \cdot S_W}} = 116.2 \text{ kts.}$$

The velocity just before the rotation of the aircraft is  $V_R = V_{LOF} = 1.1 \cdot V_S$  while  $V_{TR} = 1.15 \cdot V_S$  is the transition velocity and  $V_C = 1.2 \cdot V_S$  is the climb velocity. To reach these velocities, the engine is only able to produce a percentage of the static thrust depending on the by-pass ratio BPR, here equal to 4.1:

$$\bar{T} = 0.75 \cdot T \frac{5 + \text{BPR}}{4 + \text{BPR}} = 2,248 \text{ lbf.}$$

The take-off lift coefficient  $C_{L_{TO}} = 1.62$  is computed at the lift-off velocity in Section 5.1.1 and the corresponding drag coefficients  $C_{D_{TO}} = 0.1966$  is computed using the drag study from Section 7.2.2.

During take-off, more precisely during ground run phase, lift and drag are evaluated at  $V = \frac{V_{LOF}}{\sqrt{2}}$ . By following Gudmundsson's methodology [10], distances are computed for the three types of ground with:

$$\begin{cases} \gamma_{climb} = \arcsin \frac{\bar{T} - D_{TO}}{W_{TO}} = 20^\circ; \\ R \approx 0.2156 \cdot V_S = 2528 \text{ ft,} \end{cases}$$

which are independent on the type of ground. The take-off distances are listed in Table 9.1.

Table 9.1: Take-off distances at sea level.

Type of ground	$S_G$ [ft]	$S_{ROT}$ [ft]	$S_{obst}$ [ft]	$S_{TOT}$ [ft]
Dry asphalt ( $\mu = 0.04$ )	2,443	212	382	3,037
Wet asphalt ( $\mu = 0.05$ )	2,484	212	382	3,078
Icy asphalt ( $\mu = 0.02$ )	2,366	212	382	2,960

Only the ground run distance depends on the type of ground. The same work is performed in order to find the maximum altitude of the airbase. In this case, the only interesting distance is the ground run distance. This one is equal to 4,000 feet for the worst case (wet asphalt) at an altitude of 7,830 feet. The Drop is able to take-off from high altitude ground. Therefore it can start its operations from numerous airbases in the world.

## 9.2 Climb

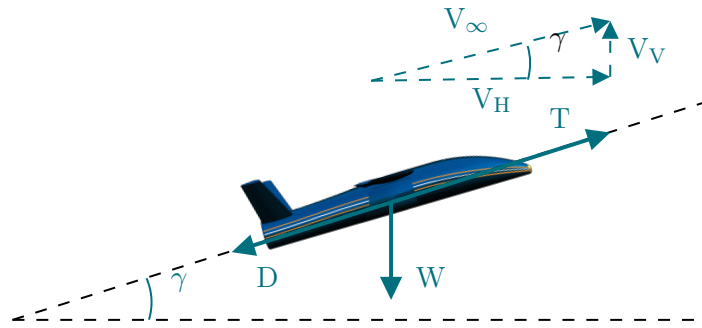


Figure 9.2: Climb phase.

After the take-off, the aircraft enters the phase of climb with an angle  $\gamma = 5^\circ$ , which is considered as a reasonable climb angle according to Gudmundsson [10]. In general, it is preferable that  $\gamma$  does not exceed a maximum climb angle  $\gamma_{max}$  of  $15^\circ$ . The rate of climb (RoC) is the vertical velocity of the aircraft and is expressed as:

$$V_V = \frac{P_{av} - P_{re}}{W} = \frac{(T - D) \cdot V_V}{W},$$

where  $P_{av}$  and  $P_{re}$  are respectively the available and required power. These variables depend on the velocity and on the altitude. The available thrust is computed with Bartel and Young [25] by following the methodology

described in Section 5.3. The drag is computed in the drag study section. Figure 9.3 represents the range of power that the engine needs to reach during the climb at sea level. It can be seen that the velocity which is associated with the highest rate of climb is 352.6 KTAS. Moreover, when the airspeed becomes higher than 661 KTAS, the available power is not sufficient anymore to achieve the climb.

Figure 9.4 shows the rate of climb depending on the true speed and the altitude. At sea level, the maximum RoC is 7,370 ft/min. The higher is the aircraft, the lower is the RoC. Thus, the ceiling (RoC = 100 ft/min) can be determined. It is equal to 43,000 ft, which is 43 % higher than the cruise altitude.

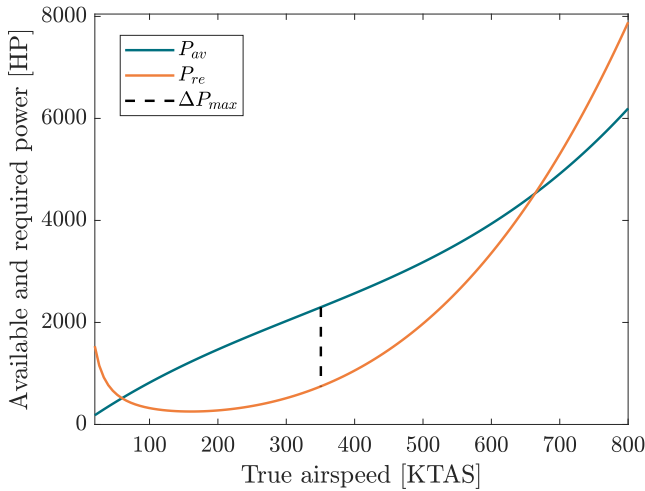


Figure 9.3: Available and required power with respect to the true airspeed at sea level.

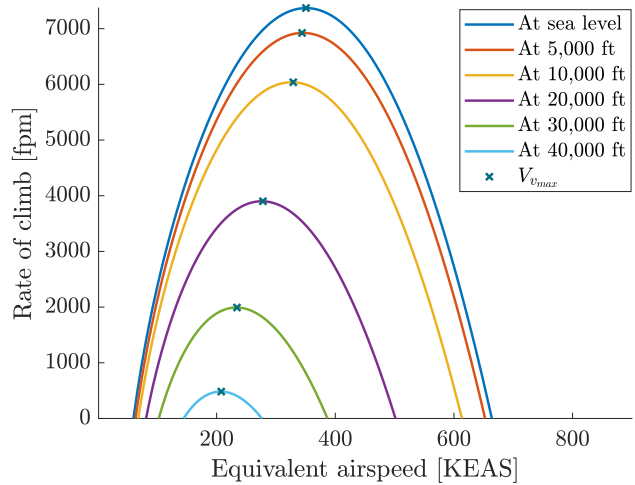


Figure 9.4: Rate of climb with respect to the true airspeed and altitude.

Figure 9.6 and Figure 9.5 show the evolution of the altitude as a function of the equivalent airspeed and respectively the rate of climb and the angle of climb. A difference between the service ceiling (RoC = 100 ft/min) and the absolute ceiling (RoC = 0 ft/min) can be made. They are respectively 43,000 ft and 43,700 ft. Figure 9.6 allows to find the maximum angle of climb  $\gamma_{\text{climb,max}} = 16.3^\circ$ . Another important quantity is the duration of the climbing phase (from 0 to 30,000 ft). This time is expressed as:

$$t = \int_{h_i}^{h_f} \frac{dh}{V_v} = 7\text{min}30\text{sec},$$

where  $V_v$  is the RoC. This time is minimized by keeping the best rate-of-climb airspeed.

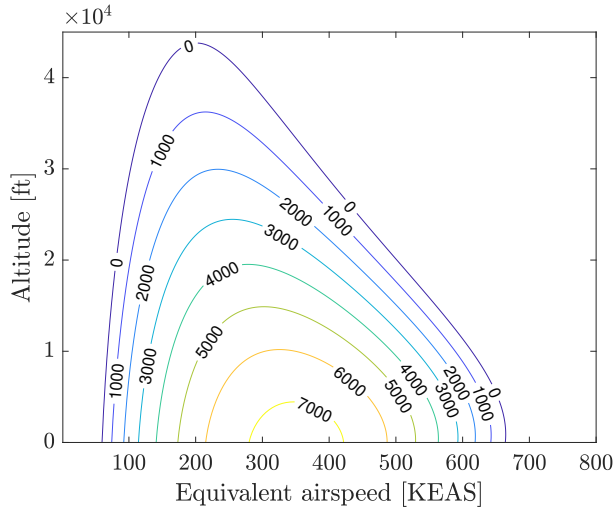


Figure 9.5: Altitude with respect to the true airspeed and rates of climb (ft/min).

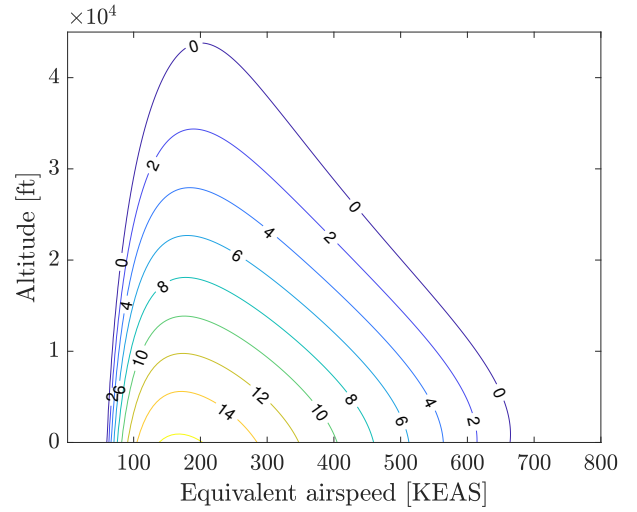


Figure 9.6: Altitude with respect to the true airspeed and climb angles (deg).

### 9.3 Turn

Figure 9.7 shows the force equilibrium during turn. This equilibrium allows keeping a constant altitude.

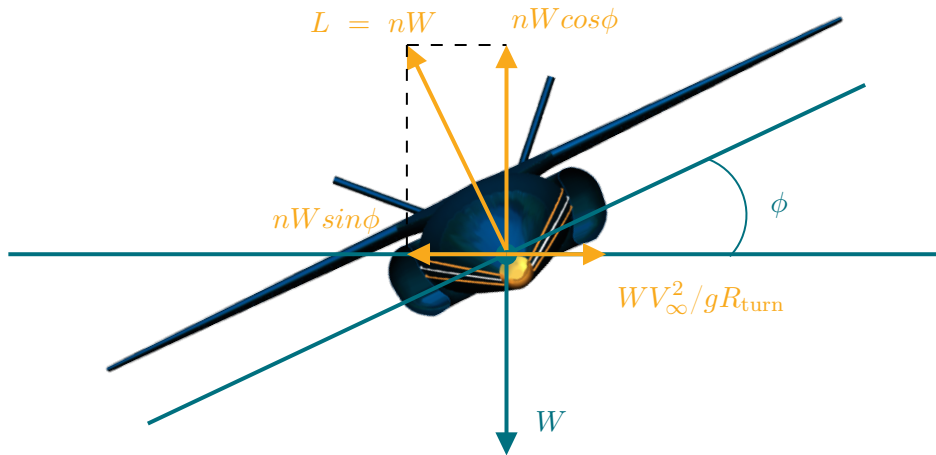


Figure 9.7: Forces acting on the aircraft in a level constant velocity turn.

The turn rate  $\dot{\Phi}$  expressed in rad/s can be computed using Eq. (9.1).

$$\dot{\Phi} = \frac{g\sqrt{n^2 - 1}}{V_\infty} = \frac{V_\infty}{R_{\text{turn}}}, \tag{9.1}$$

where  $n$  is the load factor and  $R_{\text{turn}}$  the radius of the turn maneuver. This allows to represent the turn performances map in Figure 9.8. The turn maneuver is impossible on the left of the stall limit curve and above the thrust limit curve. If the load factor  $n$  ranges between 3, the maximum load factor, and 4.5, the ultimate load factor, there are possible structure damages. For  $n > 4.5$ , there is a high probability of structural failure. Fortunately, at cruise condition, this case never happens. The maximum load factor  $n_{\text{max}}$  in cruise is the load factor that makes a tangent with the thrust limit curve. It is equal to 2.64. The maximum bank angle and its corresponding velocity are:

$$\psi_{\text{max}} = \arccos \frac{1}{n_{\text{max}}} = 67.7^\circ \quad \text{and} \quad V_{n_{\text{max}}} = \sqrt{\frac{T + \sqrt{T^2 - 4C_{D_{\text{min}}}(n_{\text{max}}W)^2}}{\rho S_w C_{D_{\text{min}}}}} = 448.1 \text{ KTAS.}$$

The minimum turn radius as well as the minimum velocity are computed as:

$$R_{\text{turn}_{\text{min}}} = \frac{V_{\text{turn}_{\text{min}}}^2}{g\sqrt{n_{\text{min}}^2 - 1}} = 4,500 \text{ ft} \quad \text{with} \quad \begin{cases} n_{\text{min}} = \sqrt{2 - 1/n_{\text{max}}^2} = 1.362; \\ V_{\text{turn}_{\text{min}}} = 2\sqrt{\frac{(W/s)k}{(T/W)\rho}} = 216.8 \text{ KTAS.} \end{cases}$$

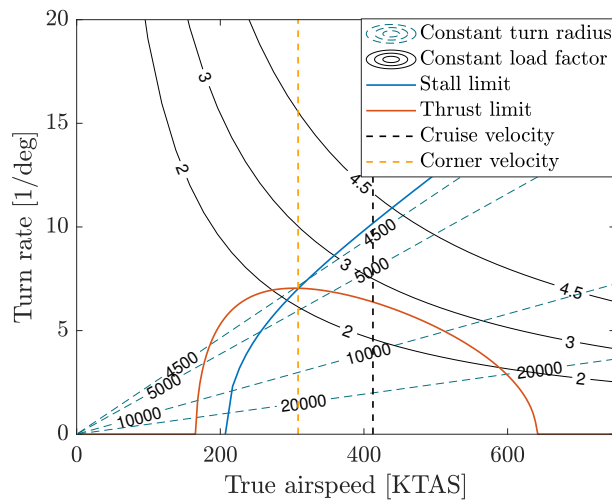


Figure 9.8: Turn performances map at cruise altitude.

## 9.4 Glide

Glide performances are critical in the case of an engine failure. Therefore, they are essential to be known in order to save the integrity of the aircraft. The best glide speed is defined as:

$$V_{BG} = \sqrt{\frac{2W}{\rho S}} \sqrt{\frac{1}{\pi e A R C_{D_0}}} = 197.3 \text{ kts},$$

where  $W$  is the weight of the aircraft and  $C_{D_0} = 0.019$  is computed in the drag study. The aim of the pilot is to maximize the glide ratio and to reach the maximal glide range. The maximum glide ratio is computed as:

$$\left(\frac{L}{D}\right)_{max} = \frac{1}{\sqrt{4C_{D_0} \frac{1}{e\pi AR}}} = 15.58.$$

Therefore, the distance which can be glided before hitting the ground, starting to glide at  $h = 30,000$  ft, is:

$$R_{glide} = h \cdot \left(\frac{L}{D}\right)_{max} = 76.94 \text{ nm}.$$

Finally, the rate of descend in the case of an engine fail can be computed using the glide distance, the cruise altitude and the cruise best glide speed:

$$\text{RoD} = V_{bg} \cdot \sin\left(\arctan\left(\frac{h}{R_{glide}}\right)\right) = 1,221 \text{ ft/min}.$$

## 9.5 Landing

Regarding the requirements, the aircraft must land in less than 4,000 ft on dry, wet and icy asphalt and generally pass an obstacle of 50 feet. As for the take-off, the landing is separated into four sections. The first one is the approach ( $S_A$ ) with an assumed approach angle  $\gamma_{app} = 3^\circ$  [10]. This phase is followed by the flare ( $S_F$ ) and free roll ( $S_{FR}$ ). The aircraft touches the ground between these two phases. The past segment is the braking ( $S_{BR}$ ) which is the longest part of the landing. The landing is represented in Figure 9.9.



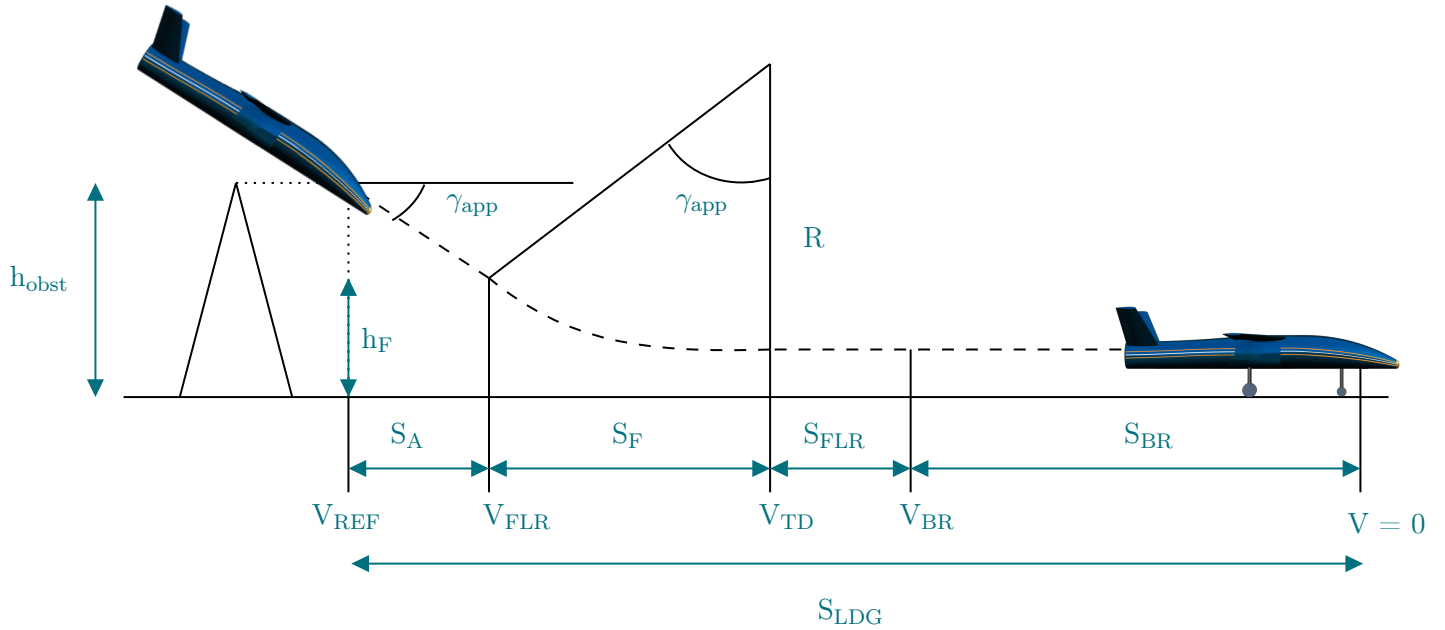


Figure 9.9: Landing phase.

Once again, each velocity depends on the stall velocity:

$$V_S = \sqrt{\frac{2 \cdot W_{\text{LDG}}}{\rho \cdot C_{L_{\text{max,LDG}}} \cdot S_W}} = 196.2 \text{ ft/s},$$

where  $W_{\text{LDG}}$  is the empty weight,  $V_{\text{REF}} = V_{\text{FLR}} = 1.3 \cdot V_S$  is the approach velocity or reference velocity while  $V_{\text{TD}} = V_{\text{BR}} = 1.1 \cdot V_S$  is the touch down velocity or the velocity just before braking. Once again the take-off lift coefficient  $C_{L_{\text{LDG}}} = 1.84$  is computed at the touch down velocity in Section 5.1.1 and the corresponding drag coefficients  $C_{D_{\text{TO}}} = 0.1966$  is computed using the drag study in Section 7.2.2. The approach angle  $\gamma_{\text{app}}$  is set to  $3^\circ$  since it is generally the target angle for approach.

The braking distance is given as:

$$S_{\text{BR}} = \frac{V_{\text{BR}}^2}{2a} \quad \text{with} \quad a = \frac{g}{W_{\text{LDG}}} (T - D_{\text{LDG}} - \mu(W_{\text{LDG}} - L_{\text{LDG}})).$$

The lift and drag are evaluated at  $\frac{V_{\text{BR}}}{\sqrt{2}}$  and a reverse thrust  $T = -0.3 \cdot T_0$  can be used for a low by pass ratio turbofan [9]. By following the Gudmundsson's methodology [10], the other distances are computed and given in Table 9.2.

Table 9.2: Landing distances at sea level.

Type of ground	$S_A$ [ft]	$S_F$ [ft]	$S_{FR}$ [ft]	$S_{BR}$ [ft]	$S_{LDG}$ [ft]
<b>Dry asphalt</b> ( $\mu = 0.4$ )	940	28	118	647	1,733
<b>Wet asphalt</b> ( $\mu = 0.225$ )	940	28	118	744	1830
<b>Icy asphalt</b> ( $\mu = 0.08$ )	940	28	118	850	1,936

Only the braking distance depends on the type of ground. The distance for the icy asphalt is logically the longest. Because the aircraft is very light at landing and thanks to the reverse thrust of its engine, landing is also possible at very high altitude ground. The Drop can thus land in numerous airbases in the world.

### 9.5.1 Crosswind conditions landing

The vertical tail and the rudder must provide stability and control in landing configuration. Critical cases of high speed crosswind conditions are thus studied here to ensure good landing conditions. Take-off conditions should also be considered. However, conditions at landing are more restrictive and 85% of accidents occurs while landing, as stated in Sadraey [18]. Only the case of landing is thus studied. In case of crosswind, the rudder must be able to counter the effects of the wind on the plane to assure landing in the axes of the track by using yawing moment to do a "crabbing approach"[18]. Here, a  $90^\circ$  angle of attack wind is considered to study the worst case. The angle of deflection of the rudder is calculated using Sadraey methodology [18]. Moreover, the V-tail configuration is simplified by considering that the rudder surfaces is the vertical projection of the ruddervator as explained in Section 5.1.3. The rudder control derivatives  $C_{y_{\delta_r}}$  and  $C_{n_{\delta_r}}$  must be evaluated, using Sadraey method [18]. These values are listed in Table A.1 in Appendix A. Figure 9.10 shows the evolution of the deflection angle required to counteract the action of the wind during landing. FAR Part 23 Section 233 requires that each GA aircraft must be able to carry out landing for  $90^\circ$  cross-winds of a wind velocity up to 25 knots [18]. This regulation is respected as the maximum wind speed at which The Drop can land is 36.35 knots, with a deflection angle of  $30^\circ$ . Additionally, the rudder surface is sufficient to ensure performances at landing and thus at take-off as well. Note that the value of 36.35 knots is the limit value beyond which the control is lost. A safety margin must therefore be respected and is set to 25% according to Gudmundsson [10], so that the maximal acceptable deflection angle is  $22.5^\circ$  and the wind speed maximal value of 25 knots is still manageable.

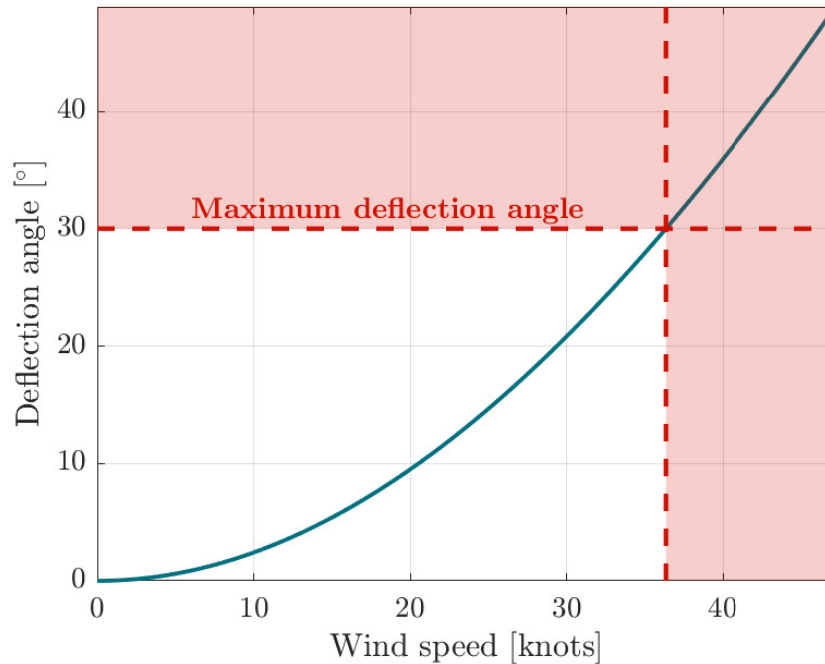


Figure 9.10: Deflection angle of the ruddervator with regards to the cross-wind speed.

## 9.6 Payload-range diagram

The payload-range diagram corresponding to cruise speed at Mach 0.7 is represented in Figure 9.11. This speed is chosen since it maximizes the range contrary to higher speeds as Mach 0.8 or Mach 0.85. Lower speeds are not considered here to reach the threshold. As the payload mass is very small with respect to the mass of the entire aircraft and the fuel, the range does not vary significantly if the payload is reduced or removed. The required fuel mass to fulfill the main mission is 4,2503 lbs. The fuel reserve is computed to provide enough fuel to fly one-half hour at maximum speed *i.e.* at dash speed (see Eq. (8.1)), as stated in FAR regulations [19]. The range reached at maximum take-off weight is 5,219 nm while the maximal range is 5,476 nm. Finally, the range reached for higher payloads, computed with the triple of the payload, gives a range of 4,765 nm. Obviously, an increase of the payload would indeed decrease the range of The Drop.

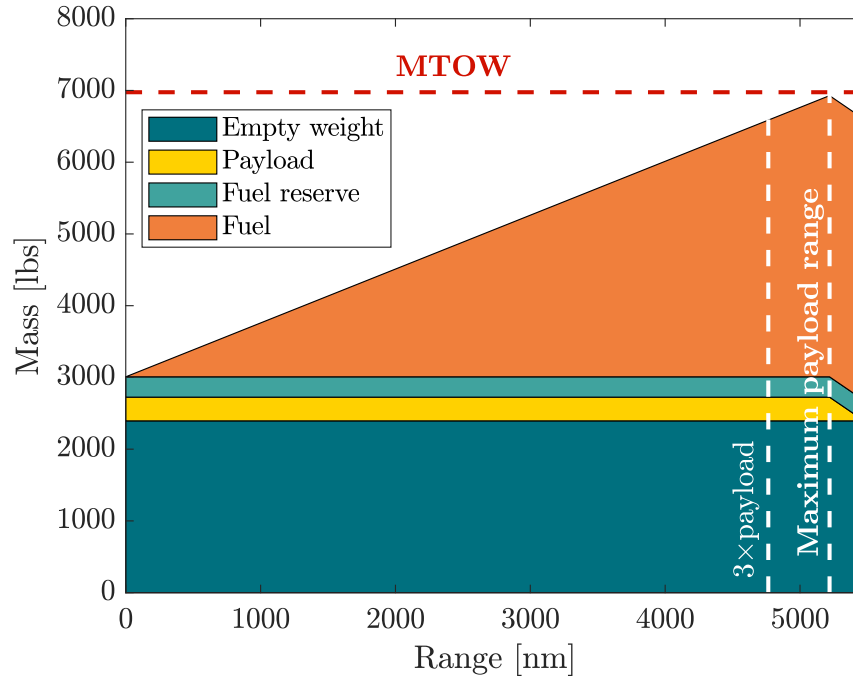


Figure 9.11: Payload-range diagram.

## 10 Cost Analysis

During the preliminary design of a product, it is important to assess the costs associated to the designed product such as the costs of the product's development, production and operation. This study is as critical as the preliminary design of aircraft's parts. In fact, if the costs of the aircraft is too high, the airplane will certainly never leaves the drawing board. The aim of every potential buyer is either to make profit from its aircraft as fast as possible or either to limit the costs of its operations, if it has no means of reimbursing the purchase as it is the case for water bombers used by the authorities during fires.

During the preliminary design phase of the design of a new aircraft, only statistical cost-estimating methods can be applied to the costs do analysis. Such a method is called a Cost-Estimating Relationship (CER). One of the most renamed for conceptual aircraft design is the RAND Corporation's DAPCA IV model, on which the following analysis is based. This model estimates the workload for the development and the production of the airplane based on simple parameters such as its weight, maximum cruising speed and the number of aircraft produced. The particular method to apply this model is described by S. Gudmundson [10].

First, a projection of the economy in 2028, when The Drop is expected to be released, is presented. This section ensures that the considered price are valid. In order to compute the production costs, the number of man-hours required for engineering, tooling and manufacturing must then be estimated. The costs are then

evaluated considering the fixed and the variable costs. A break-even analysis is then carried out. Finally, the operational costs are described.

## 10.1 Economy projection in 2028

It is important to notice that S. Gudmunson takes into account the costs of living in the year 2012. As The Drop must be available by 2028, the consumer price index must be considered between 2012 and 2028 in order to update the price stated by S. Gudmunson. The Federal Reserve Bank of Minneapolis [44] provides the evolution of the CPI between the year 2012-2023. In addition, according to the Federal Reserve Bank Philadelphia [45], the forecasters predict that headline CPI inflation will be at an annual-average rate of 2.37 % over the next years. Therefore, an annual CPI growth of 2.37 % per year over the period 2023-2028 is considered. The evolution of the CPI from 2012 to 2028 is represented in Figure 10.1.

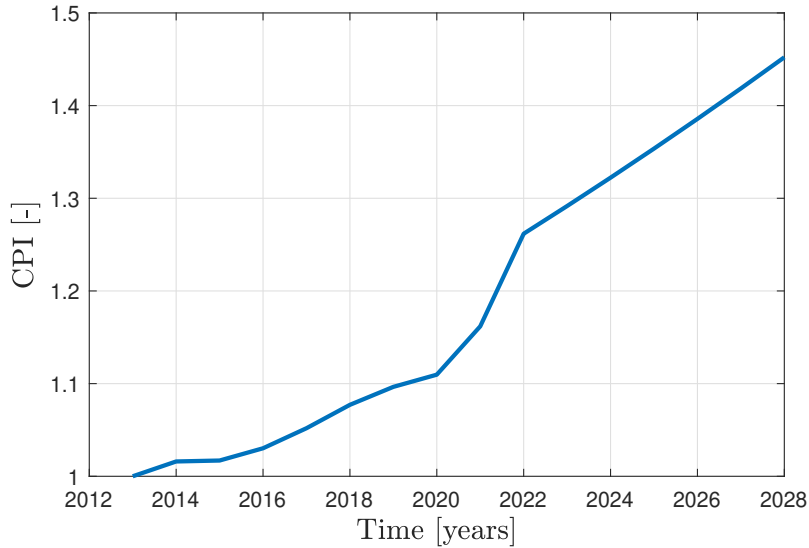


Figure 10.1: CPI evolution and prediction over the years with the year 2012 being the reference year.

## 10.2 Number of hours

The number of man-hours is computed following the method prescribed by S. Gudmunson [10]. The number of hours required for engineering, tooling and manufacturing are given by:

$$\left\{ \begin{array}{l} H_{eng} = 0.0396 \cdot W_{empty}^{0.791} \cdot V_{max}^{1.526} \cdot N^{0.183} \cdot F_{cert} \cdot F_{cf} \cdot F_{comp} \cdot F_{press}; \\ CH_{tool} = 1.0032 \cdot W_{empty}^{0.764} \cdot V_{max}^{0.899} \cdot Q_m^{0.189} \cdot Q_m^{0.066} \cdot F_{taper} \cdot F_{cf} \cdot F_{comp} \cdot F_{press}; \\ H_{mfg} = 9.6613 \cdot W_{empty}^{0.74} \cdot V_{max}^{0.543} \cdot N^{0.524} \cdot F_{cert} \cdot F_{cf} \cdot F_{comp}, \end{array} \right.$$

where  $W_{empty}$  is the empty weight of the aircraft [lbs],  $V_{max}$  is the maximum reachable airspeed in cruise [kts],  $F_{taper} = 1$  as the wing is tapered,  $F_{cf} = 1$  as simple flaps are considered,  $F_{press} = 1$  as the cabin is unpressurized,  $F_{cert} = 1$  as the aircraft is meant to be 14 CFR Part 23 [46] certified and  $F_{comp} = 1$  as no CFRP material is constituting the aircraft. In addition, the number of engineers required to develop the aircraft over 5 years and the time required to manufacture one aircraft is computed as:

$$\begin{cases} N_{eng} & = \frac{H_{eng}}{5 \cdot 40 \cdot 8}; \\ t_{manufacturing} & = \frac{H_{mfg}}{N}, \end{cases}$$

where it is assumed that an engineer works 8 hours a day, 5 days a week and 48 weeks during a year. The number of man-hours and the manufacturing characteristics are highlighted in Table 10.1.

Table 10.1: Number of hours and manpower required to produce 500 aircraft over a period of 5 years.

	Value
Engineering man hours	757,976
Tooling hours	355,488
Manufacturing hours	2,331,523
Number of engineers	79
Manufacturing time of one aircraft [hours]	4,663

## 10.3 Cost Evaluation

The cost of an aircraft can be split into two distinct costs: the fixed costs and the variable costs. They are detailed separately hereafter.

### 10.3.1 Fixed costs

Fixed costs are expenses that remain constant regardless of the level of production or sales.

The total costs to engineer the aircraft are:

$$C_{eng} = 2.0969 \cdot H_{eng} \cdot R_{eng} \cdot CPI,$$

where  $R_{eng} = \$92$  per hour and CPI is estimated in Section 10.1.

The total costs of development support are:

$$C_{dev} = 0.06458 \cdot W_{airframe}^{0.873} \cdot V_{max}^{1.89} \cdot N_p^{0.346} \cdot CPI \cdot F_{cert} \cdot F_{cf} \cdot F_{comp} \cdot F_{press},$$

where  $N_p = 1$  is the number of prototypes developed.

The total costs of flight test operations are:

$$C_{cf} = 0.009646 \cdot W_{airframe}^{1.16} \cdot V_{max}^{1.3718} \cdot N_p^{1.281} \cdot CPI \cdot F_{cert}.$$

The tooling costs are given by:

$$C_{tool} = 2.0969 \cdot H_{tool} \cdot R_{tool} \cdot CPI,$$

where  $R_{tool} = \$61$  per hour is the rate of tooling labor.

Finally, the total costs to certify the aircraft are computed as:

$$C_{certification} = C_{eng} + C_{dev} + C_{cf} + C_{tool}.$$

The different values constituting the fixed costs are listed in Table 10.2.

Table 10.2: Fixed costs distributions for 500 units produced over a period of 5 years.

Fixed costs	Value
Engineering costs	\$146,224,874
Development support costs	\$7,178,317
Flight test operation costs	\$404,458
Tooling costs	\$45,470,889
Total = Certification costs	\$199,278,538

### 10.3.2 Variable costs

The variable costs include all the costs that depend on the number of produced aircraft. Thus, the costs of manufacturing, the costs of quality control, the total costs of materials, the total costs of the avionics and the total costs of delivered package must be computed.

First the avionics are estimated to be \$15,000 per aircraft.

The total costs of manufacturing are:

$$C_{mfg} = 2.0969 \cdot H_{mfg} \cdot R_{mfg} \cdot CPI,$$

where  $R_{mfg} = \$53$  per hour, is the rate of manufacturing labor.

The total costs of quality control are:

$$C_{QC} = 0.13 \cdot C_{mfg} \cdot F_{cert} \cdot F_{comp}.$$

The total materials costs are:

$$C_{mat} = 24.896 \cdot W_{airframe}^{0.689} \cdot V_{max}^{0.624} \cdot N^{0.792} \cdot CPI \cdot F_{cert} \cdot F_{cf} \cdot F_{press}.$$

The costs of the engine are:

$$C_{pp} = 1035.9 \cdot N_{pp} \cdot T^{0.8366} \cdot CPI,$$

where  $N_{pp} = 1$  is the number of engines and  $T$  is the nominal thrust at cruise. The contribution of the costs is summarized in Table 10.3 where a QDF of 0.9% is applied on the price of avionics and engine.

Table 10.3: Variable costs for 500 aircraft produced over 5 years.

Variable costs	Value
Manufacturing labor costs	\$ 259,115,615
Quality control costs	\$33,685,030
Material/equipment costs	\$35,273,494
Engine	\$83,928,870
Avionics	\$6,750,000
<b>Total = Variable costs</b>	<b>\$418,753,009</b>



## 10.4 Break-even analysis

The number of aircraft produced is assumed to be 500 over a period of five years. In fact, a high production rate is chosen. Because of the high turnover of aircraft, they should indeed be replaced every 50 flights. Therefore, 100 aircraft must be produced each year. The selling price as a function of units produced is represented in Figure 10.2.

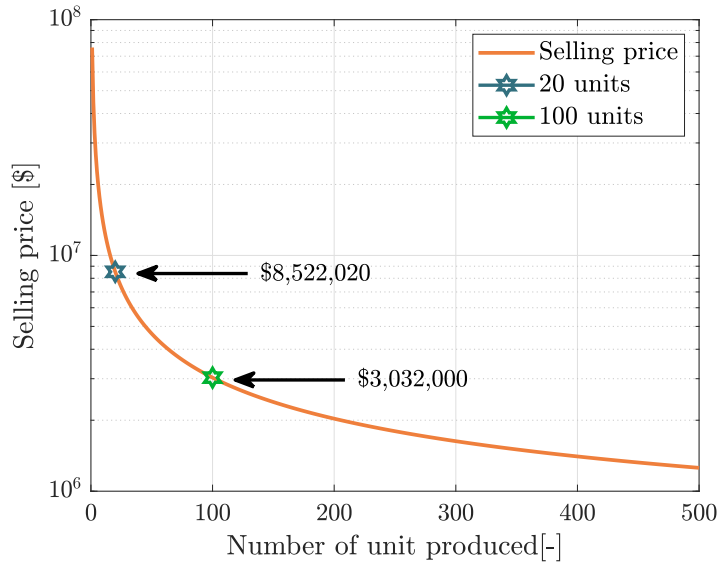


Figure 10.2: Selling price [\$] as a function of units produced N.

Knowing the minimal selling price, the number of aircraft that must be sold in order to make profit can be calculated. The aim of every company is indeed to sell its product and to make benefits from it. The number of units break-even is given by:

$$N_{BE} = \frac{\text{total fixed costs}}{\text{unit sale price} - \text{unit variable costs}}$$

The total fixed costs does not depend on the number of units produced. However, the unit variable costs strongly depend on the number of units produced and therefore will define the number of units to break even. Different unit sale prices are considered: 110%, 120% and 130% of the minimal selling price, \$ 1,256,213. The different break-even points and their selling prices are represented in Figure 10.3. In order to maximize the profitability, a 30% profit is selected. **The final selling price of The Drop is thus \$1,633,078.** Break-even is met after selling 257 aircraft.

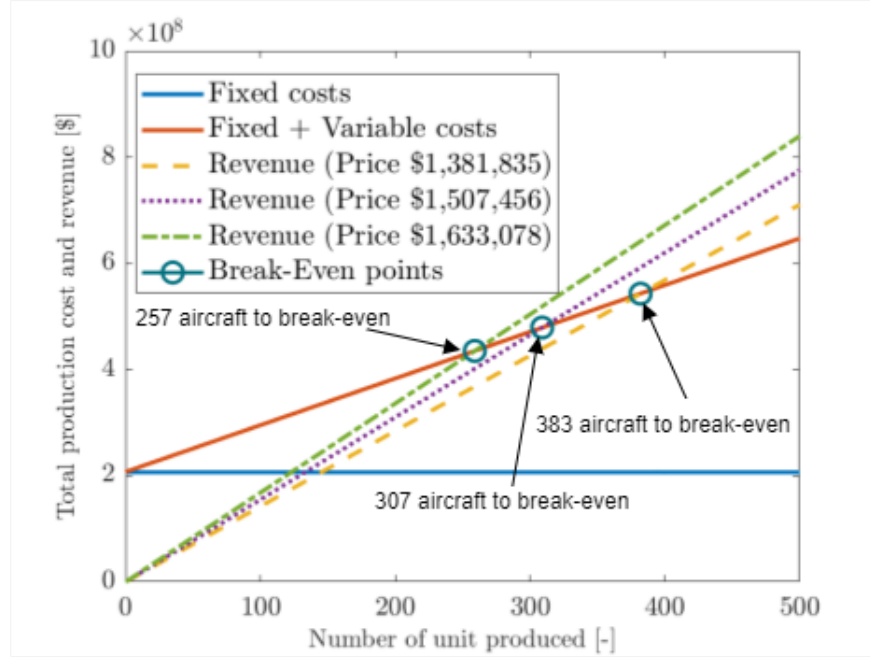


Figure 10.3: Break-even analysis based on a minimum sale price of \$ 1,256,213.

## 10.5 Operational costs

Estimating the operational costs of the aircraft is a key aspect of development. Potential customers indeed need to know how much they have to pay on average to use the aircraft and maintain it when it is on the ground.

The maintenance costs per year are estimated as:

$$C_{ap} = F_{mf} \cdot R_{ap} \cdot Q_{flgt},$$

where, according to Gudmonson [10],  $F_{mf} = 0.26$  is the ratio of maintenance man-hours to flight hours when the maintenance is assumed to be performed by the owner of the aircraft. The hourly rate for a certified airframe and powerplant mechanic is  $R_{ap} = \$60$ . The number of hours flown per year is  $Q_{flgt}$ .

In addition, the costs of storage are estimated as:

$$C_{storage} = 12 \cdot R_{storage} \cdot CPI,$$

where  $R_{storage} = \$250$  in 2012.

The annual fuel costs are estimated by:

$$C_{fuel} = BHP_{cruise} \cdot SFC_{cruise} \cdot Q_{flgt} \cdot R_{fuel},$$

where BHP is the typical horsepower during cruise,  $SFC_{cruise} = 0.00247$  lbf/hr/BHP is the specific fuel consumption of the engine at cruise and  $R_{fuel} = \$2.68$  per gallon is the price of one gallon of kerosine on the date of 19<sup>th</sup> April 2023 according to Reference [47].

The insurance costs are given by:

$$C_{ins} = 500 + 0.017 \cdot C_{ac},$$

where  $C_{ac}$  is the insured value of the aircraft. As the The Drop is a newly designed aircraft,  $C_{ac}$  amounts to the purchase price of the aircraft.

The annual inspection costs are given by:

$$C_{insp} = \$500 \cdot CPI.$$

The engine overhaul found per year is:

$$C_{over} = 5 \cdot N_{pp} \cdot Q_{flgt} \cdot CPI.$$

In light of the above, the total yearly costs of the aircraft are:

$$C_{year} = C_{ap} + C_{storage} + C_{fuel} + C_{insp} + C_{insurance}.$$

The costs of operation for one aircraft are resumed in Table 10.4. Different numbers of flight hours per year are considered in order to provide sufficient data to possible buyer. Table 10.4 highlights the fact that the costs to operate the aircraft over one year is mainly driven by the fuel costs. The price of 1 package is specified as well. This price is based on the price of the satellite phone [32], two bottles of water, a survival kit and one blanket assuming a quantity discount factor of 90%.

Table 10.4: Costs of operation of one aircraft per year.

Flying hours per year	200 hours	400 hours	600 hours
Maintenance costs	\$4,530	\$9,061	\$13,592
Storage costs	\$4,356	\$4,356	\$4,356
Annual fuel costs	\$128,320	\$256,665	\$384,970
Annual insurance costs	\$19,343	\$19,343	\$19,343
Annual inspection costs	\$726	\$726	\$726
Engine overhaul funds	\$1,500	\$2,904	\$4,356
1 Package	\$400	\$400	\$400
Total yearly operational costs	\$159,175	\$293,304	\$427,350

## 11 Trade-off study

A trade-off study allows designers to evaluate the relative merits and drawbacks of different design options and to make informed decisions about the final design of the aircraft. A trade-off study typically involves examining a range of design options and evaluating them based on a set of pre-defined criteria, such as performances, costs, weight and other factors.

The aim of a trade-off study is to find the optimal design for the aircraft, taking into account the requirements and constraints of the project. This may involve making trade-offs between different design options in order to find the best balance between competing objectives. For example, the designers may need to trade-off the weight of the aircraft against its performances in order to find a design that is both lightweight and aerodynamically efficient.

Overall, a trade-off study is a crucial part of the design process for an aircraft, as it allows designers to make informed decisions about the final design of the aircraft and to ensure that the aircraft meets all performances and operational requirements. A first trade-off study is made on the aspect ratio by observing the effects of an increase and a decrease of this parameter on several results of The Drop while keeping the same wing area. The results of this study are highlighted in Table 11.1. Generally speaking, an increase in the aspect ratio increases the performances of the aircraft but these differences are relatively small. However, it is interesting to note that the take-off and landing distances increase slightly. It is also important to mention

Table 11.1: Trade-off study of the aspect ratio and specific fuel consumption.

Evaluation criteria	Aspect ratio			Proportion of lift generated by fuselage [%]		
	-1	0	+1	0%	5%	10%
Variation	-1	0	+1	0%	5%	10%
Value	6	7	8	0%	5%	10%
Takeoff distance [ft]	-1.23%	3037	+0.69%	3037	+0.35%	+1.17%
Landing distance [ft]	-1.69%	1,733	+1.37%	1,733	+2.22%	+4.71%
MTOW [lbs]	+2.61%	6,934.4	-2.20%	6,934.4	-4.65%	-8.91%
Fuel Weight [lbs]	+3.37%	4,233.3	-2.86%	4,233.3	-6.12%	-11.74%
Drag [lbf]	+3.38%	496	-2.86%	496	-6.12%	-11.74%
Lift to drag ratio	-0.74%	14.99	+0.69%	14.99	+1.57%	+3.21%

that structural considerations cannot be ignored and that the aspect ratio cannot be increased indefinitely or else unmanageable structural problems will occur.

Secondly, as the fuselage of The Drop might produce some lift as it is not symmetric, a trade-off study of this effect is made. The results are gathered in Table 11.1. The present study does not take into account this effect as it is very hard to model in a conceptual design, but the trade-off consider that the fuselage generates successively 5 and 10% of the total lift of the aircraft. The lift generated by the wing is thus reduced. In order to simplify calculations of this effect, the lift generated by the fuselage is considered to be applied on the center of gravity of the aircraft to avoid any momentum generation. The parameter that varies here is the proportion of the aircraft weight carried by the wing and tail, going from almost 100% to 95% and then to 90% to artificially model a lift generated by the fuselage. The performances of The Drop increase in a general way, especially the fuel weight which decreases of about 10% for a fuselage creating 10% of the total lift. The required lifting surfaces of the tail and the wings are also smaller. This consequently increases the stall speed at take-off and then the take-off distance, but it also decreases the drag generated by these surfaces.

## 12 Conclusion

Through this work, the preliminary design of The Drop was presented. The Drop is a disaster response search and identification aircraft which aims to meet the American Institute of Aeronautics and Astronautics proposal. Thus The Drop's main mission is to identify victims in the aftermath of natural disasters and to provide them with rescue resources. Since hours or minutes can save numerous lives, delivering the packages should be achieved as fast as possible. Moreover, in order to help the most victims possible, the loiter should be maximized.

Regarding its mission, The Drop's target market is any government agencies or other organizations involved in disaster relief efforts. These organizations would be interested in its numerous attributes.

First, The Drop is an autonomous air vehicle. This characteristic ensures minimal operational logistics. No ground crew is indeed required during the fulfillment of the mission. This can in turn increase the response time in the aftermath of a natural disaster since only the technicians ensuring take-off must be mobilized.

Then, The Drop displays a long range. The ingress, the egress and the loiter ranges are respectively equal to 850 nm, 2,000 nm (5h) and 2,060 nm, which correspond to the objectives of the Key Performance Parameters given by the AIAA. In order to achieve this long range, the cruise speed corresponds to the threshold Mach 0.7. However, this velocity is high enough to ensure a quick response.

Moreover, in order to help a maximum of victims, the payload of The Drop corresponds to the objective of 330 lbs. The survival packages are composed of two water bottles, a satellite phone, a survival blanket and a survival kit. This packages are dropped from a bay door. This release system enables to deliver the packages at high altitude, which contributes to increasing the range since no descent is required.

Additionally, by studying the performances, it was shown that The Drop can take-off in less than 3,078 ft and land in less than 1,936 ft. The thresholds from the AIAA requirements are thus exceeded. The maximum altitude at which The Drop can takeoff is 7,830 ft. The Drop can therefore be deployed from and return to numerous airbases in the world.

Finally, assuming a production of 500 aircraft over 5 years, the minimal selling price is \$1,256,213 and the final selling price assuming a 30% profit is \$1,633,078. Only 257 aircraft must then be sold in order to start making profit. Additionally, the low acquisition costs ensure that The Drop is affordable to the potential buyers.

To conclude, The Drop displays the main features that government agencies for disaster response search and identification could be interested in. It can thus be successful on the market.

## A Derivatives

Table A.1: Aerodynamic derivatives based on DATCOM methodology [34].

Longitudinal derivatives		Lateral derivatives	
Derivatives	DATCOM value	Derivatives	DATCOM value
$C_{L\alpha}$	6.3653	$C_{n\beta}$	0.2993
$C_{D\alpha}$	0.2877	$C_{l\beta}$	-0.1313
$C_{m\alpha}$	-0.9194	$C_{y\beta}$	-0.6833
$C_{L_u}$	0.3490	$C_{n_p}$	-0.0065
$C_{D_u}$	0.1381	$C_{l_p}$	-0.5150
$C_{m_u}$	0	$C_{y_p}$	0.0345
$C_{L_q}$	8.7804	$C_{n_r}$	-0.4563
$C_{D_q}$	0	$C_{l_r}$	0.0013
$C_{m_q}$	-16.92	$C_{y_r}$	0.1391
$C_{L\dot{\alpha}}$	-10.177	$C_{n_{\delta_r}}$	-0.1587
$C_{D\dot{\alpha}}$	0	$C_{y_{\delta_r}}$	0.2250
$C_{m\dot{\alpha}}$	-7.6361	$C_{n_{\dot{\beta}}}$	0.0002

## References

- [1] ‘Study finds Atlantic hurricanes becoming more frequent, destructive’. In: *Washington Post* (). URL: <https://www.washingtonpost.com/weather/2021/12/02/atlantic-hurricanes-increasing-frequency-climate/> (visited on 27/04/2023).
- [2] United States Geological Survey. *Why are we having so many earthquakes? Has naturally occurring earthquake activity been increasing? Does this mean a big one is going to hit? OR We haven’t had any earthquakes in a long time; does this mean that the pressure is building up for a big one?* www.usgs.gov. URL: <https://www.usgs.gov/faqs/why-are-we-having-so-many-earthquakes-has-naturally-occurring-earthquake-activity-been> (visited on 15/10/2022).
- [3] *Earthquakes*. URL: [http://www.earthquakes.bgs.ac.uk/news/EQ%5C\\_increase.html](http://www.earthquakes.bgs.ac.uk/news/EQ%5C_increase.html) (visited on 15/10/2021).
- [4] AIAA Aircraft Design Technical Committee. *Disaster Response Search and Identification Attributable Air Vehicle (Dr. SAAV)*. 2022.
- [5] *Northrop Grumman X-47B*. Wikipedia, Jan. 2022. URL: [https://en.wikipedia.org/wiki/Northrop\\_Grumman\\_X-47B#/media/File:X-47B\\_operating\\_in\\_the\\_Atlantic\\_Test\\_Range\\_\(modified\).jpg](https://en.wikipedia.org/wiki/Northrop_Grumman_X-47B#/media/File:X-47B_operating_in_the_Atlantic_Test_Range_(modified).jpg) (visited on 23/10/2022).
- [6] *Baykar Bayraktar Kızılelma*. Wikipedia, Oct. 2019. URL: [https://en.wikipedia.org/wiki/Baykar\\_Bayraktar\\_K%5C%C4%5C%B1z%5C%C4%5C%B1lelma](https://en.wikipedia.org/wiki/Baykar_Bayraktar_K%5C%C4%5C%B1z%5C%C4%5C%B1lelma) (visited on 23/10/2022).
- [7] *Scaled Composites 401*. Wikipedia, Mar. 2021. URL: [https://en.wikipedia.org/wiki/Scaled\\_Composites\\_401](https://en.wikipedia.org/wiki/Scaled_Composites_401) (visited on 23/10/2022).
- [8] *EADS Barracuda*. Wikipedia, Jan. 2023. URL: [https://en.wikipedia.org/wiki/EADS\\_Barracuda](https://en.wikipedia.org/wiki/EADS_Barracuda) (visited on 23/10/2022).
- [9] Daniel P Raymer. *Aircraft design : a conceptual approach*. 6th ed. American Institute Of Aeronautics and Astronautics, Inc, Sept. 2018. URL: <https://arc.aiaa.org/doi/book/10.2514/4.104909> (visited on 27/04/2023).
- [10] Snorri Gudmundsson. ‘General Aviation Aircraft Design (Second Edition)’. In: ed. by Snorri Gudmundsson. Second Edition. Butterworth-Heinemann, 2022. ISBN: 978-0-12-818465-3. DOI: <https://doi.org/10.10>



- 16/B978-0-12-818465-3.09986-9. URL: <https://www.sciencedirect.com/science/article/pii/B9780128184653099869>.
- [11] *The Supercritical Airfoil*. NASA. URL: <https://www.nasa.gov/centers/dryden/about/Organizations/Technology/Facts/TF-2004-13-DFRC.html> (visited on 18/03/2023).
- [12] Charles D. Harris. *NASA supercritical airfoils: A matrix of family-related airfoils*. NTRS - NASA Technical Reports Server, Mar. 1990. URL: <https://ntrs.nasa.gov/citations/19900007394> (visited on 24/04/2023).
- [13] *XFOIL, Subsonic Airfoil Development System*. URL: <https://web.mit.edu/drela/Public/web/xfoil/>.
- [14] Noels L. *Aircraft Design: Conceptual Design*. ULiege, 2022.
- [15] John C. *Simple Aerodynamics Of The V-Tail*. Eckalbar, 1986.
- [16] Egbert Torenbeek. *Synthesis of subsonic airplane design*. Delft University Press, Dec. 1982. URL: <https://repository.tudelft.nl/islandora/object/uuid%5C%3A229f2817-9be9-49b6-959a-d653b5bac054> (visited on 23/04/2023).
- [17] Campbell J.P. and Purser P.E. ‘Experimental Verification of a Simplified Vee-tail Theory and Analysis of Available Data on Complete Models With Vee Tails’. In: *NACA TN 823* (Jan. 1944). URL: <https://ntrs.nasa.gov/api/citations/19930091901/downloads/19930091901.pdf> (visited on 15/10/2022).
- [18] Mohammad H Sadraey. *Aircraft design : a systems engineering approach*. John Wiley & Sons, Oct. 2012. URL: <https://www.wiley.com/en-fr/Aircraft+Design:+A+Systems+Engineering+Approach-p-9781119953401> (visited on 23/04/2023).
- [19] *Code of Federal Regulations*. Apr. 2023. URL: <https://www.ecfr.gov/current/title-14/chapter-I/subchapter-C/part-23#23.2430>.
- [20] Airfoils Tools. *NACA 0010 (naca0010-il)*. Airfoiltools.com, 2019. URL: <http://airfoiltools.com/airfoil/details?airfoil=naca0010-il> (visited on 10/05/2023).
- [21] Geetesh Waghela, Manish Kumar and Nakash Nazeer. ‘OPTIMIZATION OF FUSELAGE SHAPE FOR BETTER PRESSURIZATION AND DRAG REDUCTION’. In: *International Journal of research in engineering and technology* 05 (Aug. 2016), p. 37.
- [22] David Rosado. *Products - Williams International*. www.williams-int.com, Jan. 2021. URL: <https://www.williams-int.com/products/> (visited on 20/11/2022).

- [23] Nihad E Daidzic. ‘Estimation of performance airspeeds for high-bypass turbofans equipped transport-category airplanes’. In: *Journal of Aviation Technology and Engineering* 5.2 (2016). DOI: [10.7771/2159-6670.1122](https://doi.org/10.7771/2159-6670.1122).
- [24] *JT15D*. URL: <https://www.prattwhitney.com/fr/products/general-aviation-engines> (visited on 19/04/2023).
- [25] M. Bartel and T. M. Young. ‘Simplified Thrust and Fuel Consumption Models for Modern Two-Shaft Turbofan Engines’. In: *Journal of Aircraft* 45 (July 2008), pp. 1450–1456. DOI: [10.2514/1.35589](https://doi.org/10.2514/1.35589). URL: <https://arc.aiaa.org/doi/10.2514/1.35589> (visited on 15/06/2019).
- [26] Advisory Group for Aerospace Research & Development. *Air hitakes for High Speed Vehicles*. 1992.
- [27] *Air-inlet general information*. URL: <https://www.aircav.com> (visited on 22/04/2023).
- [28] *Autonomous Flight Operations*. NASA. URL: <https://csaob.larc.nasa.gov/projects/autonomous-flight-operations/> (visited on 15/11/2022).
- [29] *Star Safire 380-HD Single LRU HD EO/IR Imaging System | Teledyne FLIR*. [www.flir.eu](http://www.flir.eu). URL: <https://www.flir.eu/products/star-safire-380-hd/> (visited on 20/04/2023).
- [30] *Lockheed Says It Can Fit 2 More Missiles In F-35 Bay*. URL: [http://www.earthquakes.bgs.ac.uk/news/EQ%5C\\_increase.html](http://www.earthquakes.bgs.ac.uk/news/EQ%5C_increase.html) (visited on 13/02/2023).
- [31] *C-130*. URL: <https://airbornescience.nasa.gov/sites/default/files/515-64.jpg> (visited on 13/02/2023).
- [32] *inReach® Mini 2 Marine Bundle*. Garmin. URL: <https://www.garmin.com/fr-BE/p/pn/010-02602-30> (visited on 27/04/2023).
- [33] Dimitriadis G. *Aircraft Design: Stability and Control*. ULiege, 2022.
- [34] Hoek D.E., Anderson R.O. and Goss C.R. *USAF Stability And Control DATCOM*. AFWAL, 1978.
- [35] Dimitriadis G. *Flight Dynamics and Control, AERO0003*. ULiege, 2023.
- [36] Michael V Cook. *Flight Dynamics Principles*. 3rd ed. Butterworth-Heinemann, Oct. 2012. URL: <https://www.elsevier.com/books/flight-dynamics-principles/cook/978-0-08-098242-7> (visited on 22/03/2023).
- [37] Adrien Crovato et al. ‘A discrete adjoint full potential formulation for fast aerostructural optimization in preliminary aircraft design’. In: *Aerospace Science and Technology* 138 (2023), p. 108332. DOI: <https://doi.org/10.1016/j.ast.2023.108332>.

- [38] *CES software*. URL: <https://www.ansys.com/products/materials/granta-edupack>.
- [39] *Sonaca*. URL: <https://www.sonaca.com/> (visited on 12/02/2023).
- [40] Snorri Gudmundsson. ‘General Aviation Aircraft Design, Applied Methods and Procedures’. In: Butterworth-Heinemann, 2022. Chap. Chapter 8 - The Anatomy of the Airfoil. ISBN: 978-0-12-818465-3. DOI: <https://doi.org/10.1016/C2018-0-03861-X>. URL: <https://www.sciencedirect.com/book/9780128184653/general-aviation-aircraft-design#book-description>.
- [41] *NX-Siemens software*. URL: <https://plm.sw.siemens.com/en-US/nx/>.
- [42] K.N. Arunkumar, N. Lohith and B.B. Ganesha. ‘Effect of Ribs and Stringer Spacings on the Weight of Aircraft Structure for Aluminum Material’. In: *Journal of Applied Sciences* 12 (Oct. 2012), pp. 1006–1012. DOI: [10.3923/jas.2012.1006.1012](https://doi.org/10.3923/jas.2012.1006.1012). URL: <https://scialert.net/fulltext/?doi=jas.2012.1006.1012> (visited on 12/03/2023).
- [43] ‘Aircraft and Aerospace Applications: Part One’. In: (). URL: <http://www.keytometals.com/Article95.htm> (visited on 25/04/2023).
- [44] *CPI evolution*. URL: <https://www.minneapolisfed.org/about-us/monetary-policy/inflation-calculator/consumer-price-index-1913-> (visited on 19/04/2023).
- [45] *CPI predictions*. URL: <https://www.philadelphiafed.org/surveys-and-data/real-time-data-research/spf-q1-2023> (visited on 19/04/2023).
- [46] *Code of Federal Regulations*. Vol. 14. 2023.
- [47] *US Gulf Coast Kerosene-Type Jet Fuel Spot Price*. URL: [https://ycharts.com/indicators/gulf\\_coast\\_jet\\_fuel\\_spot\\_price#:~:text=US](https://ycharts.com/indicators/gulf_coast_jet_fuel_spot_price#:~:text=US) (visited on 19/04/2023).
- [48] *Telephonics RDR-1700A*. URL: <https://www.telephonics.com/product/rdr-1700a>.
- [49] *UltraForce 275-HD | Teledyne FLIR*. [www.flir.fr](http://www.flir.fr). URL: <https://www.flir.fr/products/ultraforce-275-hd/> (visited on 27/04/2023).
- [50] *Propriétés des stratifiés HexTow en HexPly 8552*. URL: <https://www.hexcel.com/Products/Resources/1664/hextow-laminate-properties-in-hexply-8552> (visited on 16/02/2023).
- [51] M F Ashby and David R H Jones. *Engineering materials 2 : an introduction to microstructures and processing*. 4th ed. Butterworth-Heinemann, 2013. URL: <https://www.elsevier.com/books/engineering-materials-2/jones/978-0-08-096668-7> (visited on 27/04/2023).

- [52] Jeevanantham V., Vadivelu P. and Manigandan P. ‘Materials based structural analysis of a typical landing gear’. In: *International Journal of Innovative Science, Engineering and Technology* (2017).
- [53] ‘Introduction to Aerospace Materials’. In: *Introduction to Aerospace Materials*. Ed. by Adrian P. Mouritz. Woodhead Publishing, 2012, pp. i–iii. ISBN: 978-1-85573-946-8. DOI: <https://doi.org/10.1533/9780857095152.frontmatter>. URL: <https://www.sciencedirect.com/science/article/pii/B9781855739468500261>.
- [54] *Hurricanes’ intensity*. URL: <https://www.c2es.org/content/hurricanes-and-climate-change/>.
- [55] Champagne V.K., Ozdemir O.C. and Nardi A. *Practical cold spray*. 2021.
- [56] Langenberg P. *Relation between design safety and Y/T ratio in application of welded high strength structural steel*. 2008.
- [57] Andrienne T. and Terrapon V. *Aerodynamics: Lecture 1 - Introduction*. 2022.
- [58] S. Sivakumar and M. Syedhaleem. ‘Non-linear vibration analysis of oleo pneumatic landing gear at touchdown impact’. In: *Mathematical Models in Engineering* 4 (June 2018), pp. 89–97. DOI: [10.21595/mme.2018.19895](https://doi.org/10.21595/mme.2018.19895). URL: [https://www.researchgate.net/publication/326075740\\_Non-linear\\_vibration\\_analysis\\_of\\_oleo\\_pneumatic\\_landing\\_gear\\_at\\_touchdown\\_impact](https://www.researchgate.net/publication/326075740_Non-linear_vibration_analysis_of_oleo_pneumatic_landing_gear_at_touchdown_impact).